Study of $\Sigma(1385)$ and $\Lambda(1405)$ photoproduction at SPring-8/LEPS

Deuk Soon Ahn

Department of Physics
Osaka University

Study of $\Sigma(1385)$ and $\Lambda(1405)$ photoproduction at SPring-8/LEPS

(SPring-8/LEPSにおける $\Sigma(1385)$ と $\Lambda(1405)$ の光生成反応実験の研究)

Abstract

We have measured differential cross sections and photon beam asymmetries for the $\vec{\gamma}p \rightarrow K^{+}\ \Sigma(1385)/\Lambda(1405)$ reaction at SPring-8/LEPS facility. The experiment was carried out with a Liquid Hydrogen target at the photon energy ranges from 1.5 to 2.4 GeV and the angular range $0.6 < cos\Theta_{cm}^{K^{+}} < 1.0$. Data with the high statistics were obtained with LEPS forward spectrometers. We studied the contributions of the pseudoscalar meson(K^{-}) and the vector meson(K^{*}) exchange in the $t-$channel for $\Sigma(1385)/\Lambda(1405)$ photpoprodcution by measuring both differential cross sections and photon beam asymmetries. The photon beam asymmetry is a good mean to investigate the $t-$channel mechanism because it is possible to decompose the contribution of the exchanged particles. Our LEPS experimental results of the photon beam asymmetries for $\Sigma(1385)/\Lambda(1405)$ are the first measurements in the world. We found that the differential cross sections for $\Sigma(1385)/\Lambda(1405)$ have a forward peak at the high photon energy regions while they are almost flat at the low photon energy. Also it was found that the photon beam asymmetries increase from 0 to the positive value as the photon energy increases. From the experimental results, we expect that the contribution of the K^{*} meson exchange(natural parity exchange) for the $\Sigma(1385)$ is large at the high photon energy regions. However the contribution of the K^{-} meson exchange(unnatural parity exchange) for the $\Lambda(1405)$ or resonances contributions are considerable at the low photon energy regions.

Contents

List of Figures

List of Tables

Chapter 1

Introduction

All particles which undergo strong interactions, baryons and mesons, are collectively called 'hadrons'. The strong interactions are governed by the Quantum ChromoDynamics(QCD). In the Quark model [1], the baryons consist of three quarks(qqq) and mesons are composed of a quark and anti-quark($q\bar{q}$). There are many ground state baryons (N, Δ, Λ, Σ, Ξ, Ω,...) and their excited states (N^*, Δ^*, Λ^*,Σ^*, Ξ^*, Ω^*, ...) have been experimentally observed. Among them, the ground state of Λ baryon families, the Λ baryon was first discovered in 1950 by cosmic rays and detected in photographic emulsions. Though the particle was expected to live for $\sim 10^{-23}$ s, it actually survived for $\sim 10^{-10}$ s. It led the discovery of the strange quark.

The $\Sigma(1385)$ and $\Lambda(1405)$ hyperons have not yet been studied well while there are many experimental results for the Λ and Σ photoproduction [2–8]. The $\Lambda(1405)$ baryon resonance plays an outstanding role in various aspects in hadron and nuclear physics. It has been considered that the $\Lambda(1405)$ resonance is generated by the attractive interaction and is the $\bar{K}N$ quasi-bound state below its threshold decaying into the $\pi\Sigma$ channel. Thus, the structure of $\Lambda(1405)$ is closely related to the $\bar{K}N$ interaction. Since two particles of $\Sigma(1385)$ and $\Lambda(1405)$ are overlapped in the K^+ missing mass spectra with large decay widths, it was difficult to distinguish $\Sigma(1385)$ and $\Lambda(1405)$. However, from the experiments, the angular dependence of differential cross sections and photon beam asymmetries are possible to extract the production mechanisms of the $\Sigma(1385)/\Lambda(1405)$.

1.1 Properties of $\Sigma(1385)$ and $\Lambda(1405)$

The $\Sigma(1385)$ resonance is a positive parity(+) baryon resonance with spin J=$\frac{3}{2}$, isospin I=1 and strangeness S = -1.

The $\Lambda(1405)$ resonance is a negative parity($-$) baryon resonance with spin J=$\frac{1}{2}$, isospin I=0 and strangeness S = -1.

The mass is 1383.7 ± 1.0 MeV, 1406 ± 4 MeV and full width(Γ) is 36 ± 5 MeV, 50 ± 2 MeV for $\Sigma(1385)$ and $\Lambda(1405)$, respectively [9]. The $\Sigma(1385)$ decays mainly into the $\pi^0\Lambda$ channel (88±2%) and into the $\pi\Sigma$ channel (12±2%). The $\Lambda(1405)$ decays totally into $\pi\Sigma$ channel. These two particles are overlapped in a missing mass spectrum for the $p(\gamma,K^+)$ reaction because the mass difference between $\Sigma(1385)$ and $\Lambda(1405)$ is about 20 MeV, which is

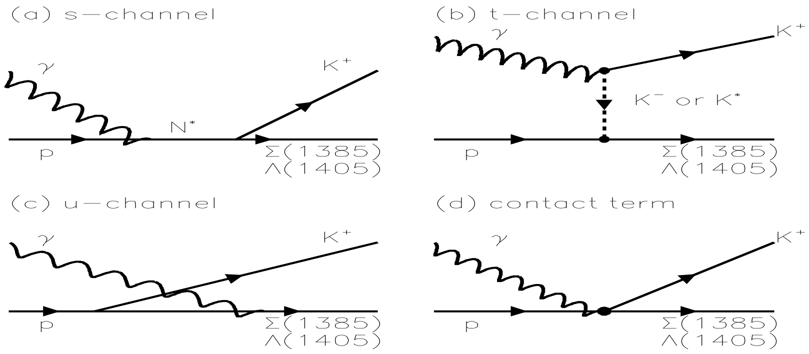

Figure 1.1: Feynman diagrams for the Σ(1385) and Λ(1405) photoproduction from a proton target.

smaller than their decay widths.

Both the Σ(1385) and Λ(1405) resonances are located near/just below $\bar{K}N$ threshold. These resonances seem to have different nature. The Σ(1385) hyperon is well established as a q^3 state [10]. On the other hand, the nature of Λ(1405) is still on an open question and there have been long standing discussions on the interpretation of the Λ(1405). The structure of Λ(1405) hyperon is indicated as a SU(3) singlet *uds* state in the quark model [10], and also it has been widely discussed as a candidate of a meson-baryon state [11, 12] or a $q^4\bar{q}$ baryon state [13]. Extensive studies of the Λ(1405) based on chiral Lagrangian suggested that the resonance is generated by meson-baryon interactions [14–19].

1.2 Photoproduction of hyperon resonances

The total/differential cross sections for Σ(1385) and Λ(1405) photoproduction, the production ratio of Λ(1405) to Σ(1385) and the lineshape of Λ(1405) have been studied experimentally and theoretically. The theoretical calculations of the photon beam asymmetry were also studied for the Σ(1385) and Λ(1405) photoproduction [20–34].

The Σ(1385) and Λ(1405) photoproduction from a proton target is well described in the Feynman diagrams as shown in Fig.1.1. In the *s*-channel, proton and resonances(N*, Δ*) are exchanged. The exchanged mesons in the *t*-channel are K, K* and K$_1$. The hypreons(Λ, Σ^0, Σ^+) and the hyperon resonances are exchanged in the *u*-channel. The contact term is required by gauge invariance.

The differential cross section of two-body kinematics $\vec{\gamma}(p_1)+p(p_2) \rightarrow K^+(k_1) + \Sigma(1385)/\Lambda(1405)(k_2)$

is given by ;

$$\frac{d\sigma}{d\Omega} = \frac{1}{64\pi^2} \cdot \frac{|\ \mathbf{k_1}\ |}{|\ \mathbf{p_1}\ |} \cdot \frac{1}{s} \mid \mathcal{M} \mid^2, \tag{1.1}$$

where the 4-momenta of the photon, the proton, the K$^+$ and the $\Sigma(1385)/\Lambda(1405)$ hyperons are denoted by p_1, p_2, k_1 and k_2, respectively. The $\mathbf{p_1}$ and $\mathbf{k_1}$ correspond to the three-momentum of the photon and the K$^+$, respectively in the center-of-mass(CM) frame. The $d\Omega$ is an infinitesimal solid angle, s ($=E_{cm}{}^2$) is the square of the center-of-mass energy and $\mathcal{M}$ is a physical amplitude [1]. The differential cross section is proportional to the square of $\mathcal{M}$ which is related to X(=s, t or u) and m_{ex}(mass of exchanged particle);

$$\mid \mathcal{M} \mid^2 \ \propto \ \frac{1}{(X - m_{ex}^2)^2}, \tag{1.2}$$

The s-channel shows isotropic behavior, and the t-channel has forward peak while u-channel has backward peak.

1.2.1 Experimental results of $\Sigma(1385)$ and $\Lambda(1405)$

The LEPS group carried out the hyperons photoproduction experiment through $\vec{\gamma} + p \rightarrow K^+ + \Sigma(1385)$ and $\vec{\gamma} + p \rightarrow K^+ + \Lambda(1405)$ reactions [20]. The production ratio of $\Lambda(1405)$ to $\Sigma(1385)$ has been measured in two photon energy regions. The experimental data are shown in Fig. 1.2 as closed circles. The data were fitted with spectra obtained by Monte Carlo(MC) simulation of $K^+\Lambda(1405)$, $K^+\Sigma(1385)$, $K^+\Lambda(1520)$, non-resonant $K^+\pi\Sigma$ and $K^{*0}\Sigma^+$. The solid lines show the spectra of $\Lambda(1405)$ with the lineshape calculated by Nacher *et al.* [19], and the open circles, dashed lines, and dot-dashed lines show the spectra of $K^+\Sigma(1385)$, non-resonant $K^+\pi\Sigma$, and $K^{*0}\Sigma^+$ production, respectively. The measured production ratio of $\Lambda(1405)$ to $\Sigma(1385)$ decreased in the higher photon energy region as listed in Table 1.1 [20]. It may suggest different production mechanisms for $\Sigma(1385)$ and $\Lambda(1405)$ hyperons.

	production ratio of $\Lambda(1405)/\Sigma(1385)$
1.5<E_γ<2.0	0.54 ± 0.17
2.0<E_γ<2.4	0.084 ± 0.076

Table 1.1: Production ratio of $\Lambda(1405)/\Sigma(1385)$ in two photon energy regions

The differential cross sections for $\vec{\gamma}+p \rightarrow K^+ + \Sigma(1385)$ and $\vec{\gamma}+p \rightarrow K^+ + \Lambda(1405)$ reactions have been measured in two photon energy regions with the K$^+$ scattering angle region, $0.8< cos\Theta_{cm}^{K+} <1.0$, in the center-of-mass(CM) system as listed in Table 1.2. The differential cross section of $\Lambda(1405)$ photoproduction was firstly measured. The differential cross section of $\Sigma(1385)$ photoproduction was obtained with $\sim$0.8μb in the two photon energy regions, and these results are almost similar with the model calculation of Oh *et al.*(0.4$\sim$1.1 μb) using the effective Lagrangian [31]. The differential cross section of $\Lambda(1405)$ photoproduction was obtained with $\sim$0.4μb at the lower photon energy region ($1.5< E_\gamma <2.0$ GeV) and this result is

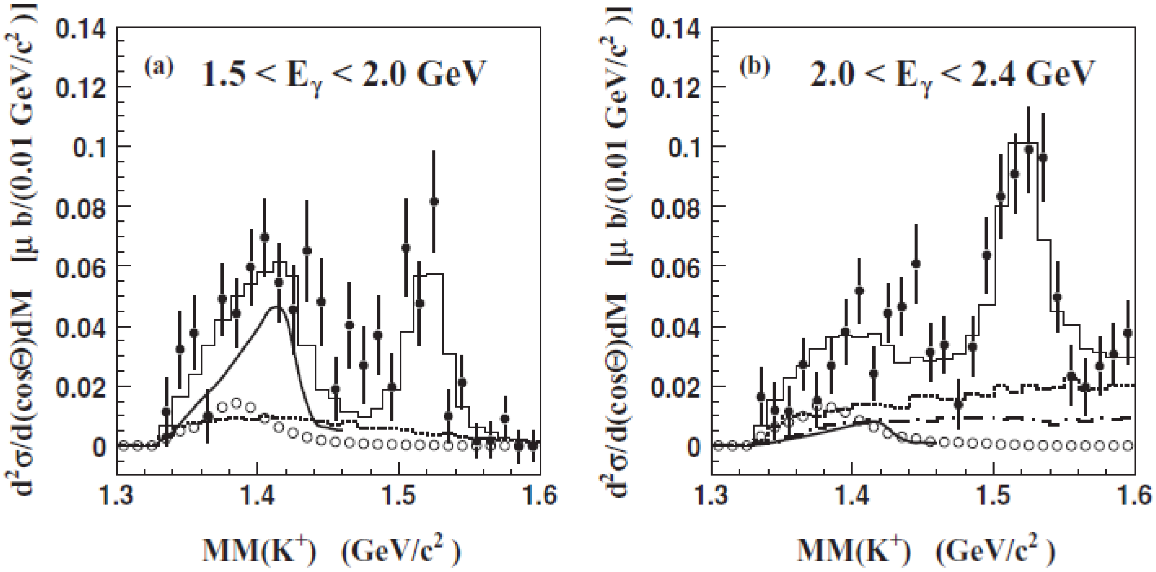

Figure 1.2: Missing mass of the $\vec{\gamma}p \rightarrow K^{+}$+X in the two photon energy ranges of (a) 1.5<E$_{\gamma}$<2.0 GeV and (b) 2.0<E$_{\gamma}$<2.4 GeV : The experimental data are shown as closed circles. The data were fitted with spectra determined by Monte Carlo(MC) simulation of $K^{+}\Lambda(1405)$, $K^{+}\Sigma(1385)$, $K^{+}\Lambda(1520)$, non-resonant $K^{+}\pi\Sigma$ and $K^{*0}\Sigma^{+}$. The solid lines show the spectra of $\Lambda(1405)$ calculated by Nacher *et al.* [19], and the open circles, dashed lines, and dot-dashed lines show the spectra of $K^{+}\Sigma(1385)$, non-resonant $K^{+}\pi\Sigma$, and $K^{*0}\Sigma^{+}$ production, respectively.

$\sim$4 times larger than the model calculation of Nam *et al.*($\sim$0.1 μb) [32], whereas the differential cross section of $\Lambda(1405)$ rapidly decrease at the higher photon energy region(2.0< E_γ <2.4 GeV).

The lineshape of $\Lambda(1405)$ were obtained for the decay mode of $\Sigma^+\pi^-$ and $\Sigma^-\pi^+$ in the $\sim 4\pi$ Time Projection Chamber(TPC) and detecting K^+ using a LEPS forward spectrometer [20]. Before the LEPS/TPC experiment, the mass spectra of the $\Lambda(1405)$ for the $\Sigma^+\pi^-$ and $\Sigma^-\pi^+$ were also measured only with the LEPS forward spectrometer, and both K^+ and $\pi^\pm$ were detected in the LEPS spectrometer and the Σ^+ or Σ^- was identified with the missing mass of the $\vec{\gamma} + p \rightarrow K^+\pi^\pm X$ reaction [21].

	dσ/d(cosΘ) of $\Lambda(1405)$	dσ/d(cosΘ) of $\Sigma(1385)$
1.5<E_γ<2.0	0.43 ± 0.088(stat.) $^{+0.034}_{-0.14}$ μb(syst.)	0.80 ± 0.092(stat.)$^{+0.062}_{-0.27}$ μb(syst.)
2.0<E_γ<2.4	0.072 ± 0.061(stat.) $^{+0.011}_{-0.0056}$ μb(syst.)	0.87 ± 0.064(stat.)$^{+0.13}_{-0.067}$ μb(syst.)

Table 1.2: Differential cross sections for $\vec{\gamma} + p \rightarrow K^+ + \Sigma(1385)$ and $\vec{\gamma} + p \rightarrow K^+ + \Lambda(1405)$ in two photon energy regions.

There are other experimental data of the differential cross sections for the $\Sigma(1385)$ and $\Lambda(1405)$ photodproduction obtained by CLAS collaboration.

Recently, CLAS collaboration measured lineshape, total/differential cross sections and spin and parity of $\Sigma(1385)$, $\Lambda(1405)$ and $\Lambda(1520)$ hyperons, respectively [22]. The differential cross sections($\frac{d\sigma}{dcos\Theta_{cm}^{K^+}}$) measured for the $\Sigma(1385)$, $\Lambda(1405)$ and $\Lambda(1520)$ hyperons are shown in Fig. 1.3. The differential cross sections for three hyperons increase in the more forward angles in all the photon energy regions, and it is noticeable in the higher photon energy bins. These results are compared only to the LEPS measurement of the $\Lambda(1405)$(blue points) [20] at the Wbin 1-4 regions. They are almost similar to those by LEPS data in the lower photon energy regions(Wbin 1-2), but they are significantly different at the higher photon energy regions(Wbin 3-4). We could find that they are distinctly larger than the LEPS results at the higher photon energy regions. On the other hand, we could find that the CLAS measurement results for $\Sigma(1385)$ are similar to the LEPS measurement results.

The differential cross sections $\frac{d\sigma}{dt}$ for the $\Sigma(1385)$, $\Lambda(1405)$ and $\Lambda(1520)$ hyperons were obtained and the results were fitted with the form of $\frac{d\sigma}{dt} = \sigma_0 e^{-b|t-t_{min}|}$, and slope parameter b was obtained. It was found that $\Lambda(1405)$ has a slightly steeper slope than others while $\Sigma(1385)$ and $\Lambda(1520)$ have similar slope parameters.

Total cross sections of $\Sigma(1385)$ photoproduction have been measured by the CLAS collaboration with a photon energy range of 1.5−3.8 GeV [25]. The total cross sections of $\gamma + p \rightarrow K^+ + \Sigma(1385)$(blue circles) were compared to the earlier measurement of $K^+\Sigma(1385)$ photoproduction(red squares) [26–28] which are shown in Fig. 1.4. The peak was observed in the CLAS data around the region of $E_\gamma = 1.8 \sim 2.0$ GeV.

The $\Lambda(1405)$ does not rapidly decrease in JLAB/CLAS experiments as the photon energy increase while the $\Lambda(1405)$ rapidly decreases at the higher energy region in the LEPS experiment.

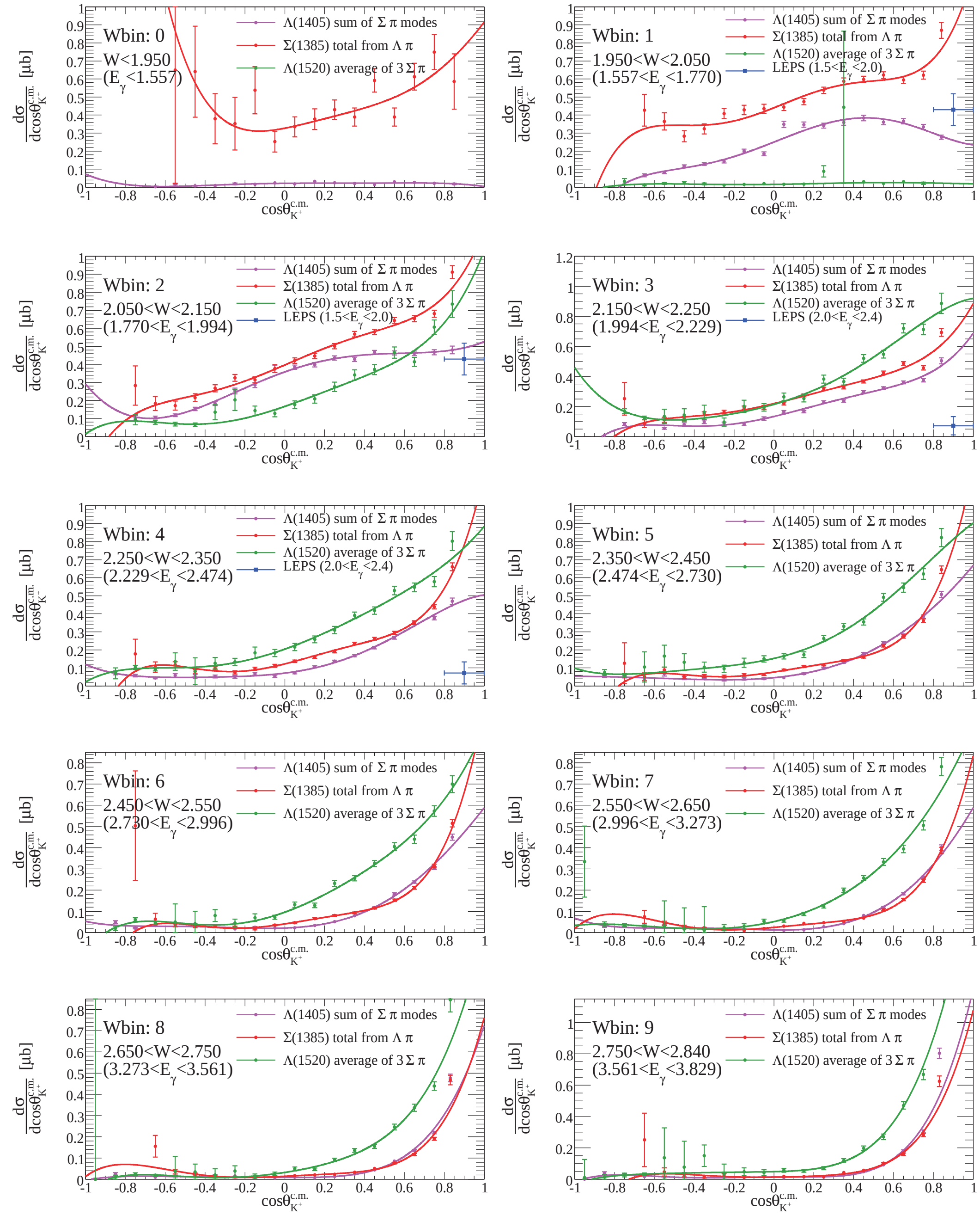

Figure 1.3: Differential cross sections $\frac{d\sigma}{dcos\theta_{cm}^{K+}}$ for the Σ(1385)(red), Λ(1405)(pink) and Λ(1520)(green) hyperons at different photon energy regions (These results are compared to the LEPS measurement [20] for the Λ(1405)(blue points) at the Wbin 1-4 regions

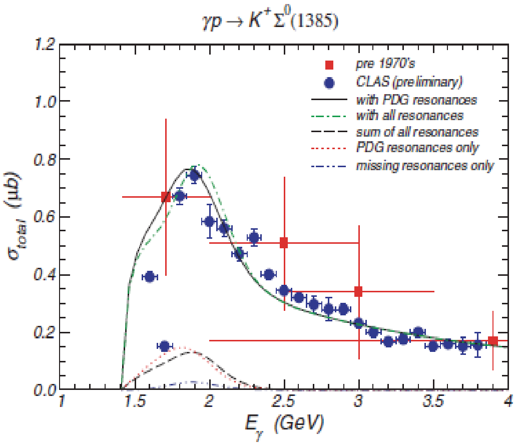

Figure 1.4: Total cross section of $\Sigma(1385)$ measured by CLAS collaboration(blue circles) and compared to the earlier(1970's) measurement(red squares)

In addition, there are old electroproduction data obtained by DESY collaboration [24]. DESY collaboration measured the differential cross sections as functions of W, q^2, t at the $1.9 < W < 2.8$ GeV by electroproduction of $ep \to eK^+Y$, $Y = \Lambda, \Sigma, \Sigma(1385), \Lambda(1405), \Lambda(1520)$ [24].

1.2.2 Theoretical studies of $\Sigma(1385)$ and $\Lambda(1405)$

There have been theoretical studies for the $\Sigma(1385)$ and $\Lambda(1405)$ photoproduction. Oh *et al.* [31] investigated the roles of N and Δ resonances in the s-channel from $\Sigma(1385)$ photoproduction, and they compared the model calculation to the CLAS data [25]. Nam *et al.* [32] investigated the $\Lambda(1405)$ photoproduction. In addition, Lutz and Soyeur [34] studied about the t-channel processes in the $\Sigma(1385)/\Lambda(1405)$ photoproduction, Williams [33] and Nacher [19] also calculated the $\Lambda(1405)$ photoproduction.

The total/differential cross sections and photon beam asymmetries for the $\vec{\gamma} + p \to K^+ + \Sigma(1385)$ reaction were calculated using the framework of gauge-invariant effective Lagrangians by Oh *et al.* [31], which are shown in Fig.1.4 and Fig.1.5. Contributions of N and Δ resonances in the Particle Data Group(PDG) and the quark model predictions are also included in Fig.1.5. The resonances are referred to as PDG resonances and include $N\frac{1}{2}^-(1945)$, $N\frac{3}{2}^-(1960)$, $N\frac{5}{2}^-(2095)$, $\Delta\frac{3}{2}^-(2080)$, and $\Delta\frac{5}{2}^+(1990)$, which are identified as $N(2090)S_{11}^*$, $N(2080)D_{13}^{**}$, $N(2200)D_{15}^{**}$, $\Delta(1940)D_{33}^*$, and $\Delta(2000)F_{35}^{**}$, respectively.

The Lagrangians were constructed with the coupling constants determined from the decay amplitudes predicted by a quark model. The coupling constant of $g_{KN\Sigma^*} = -3.22$ was used for the t-channel K^-(pseudoscalar meson) exchange, and $g_{K^*N\Sigma^*} = -5.48$ was applied to the t-channel K^*(vector meson) exchange. The monopole type form factor was used for the t-channel K^- exchange as Eq. 1.3,

$$F_M(q_{ex}^2, M_{ex}) = \frac{\Lambda_M^2 - M_{ex}^2}{\Lambda_M^2 - q_{ex}^2} \tag{1.3}$$

and the Gaussian type form factor was used for the t-channel K^* exchange, s and u channel

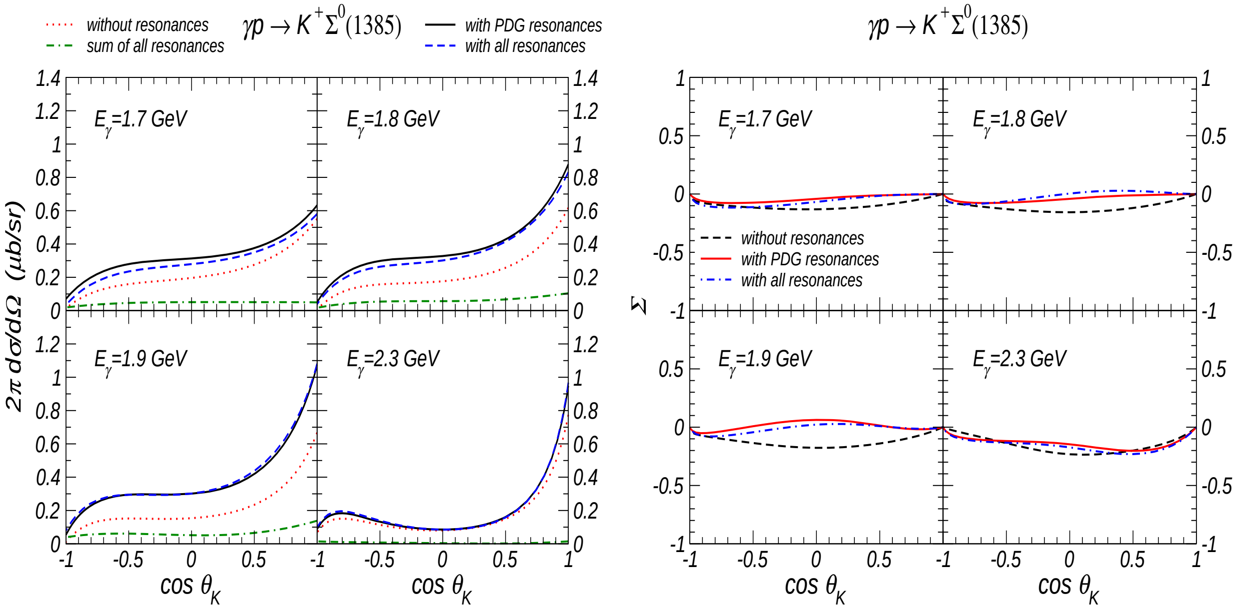

Figure 1.5: Differential cross section(Left) and photon beam asymmetry(right) of $\Sigma(1385)$

diagrams as Eq. 1.4.

$$F_G(q_{ex}^2, M_{ex}) = \left(\frac{n\Lambda_B^4}{n\Lambda_B^4 + (q_{ex}^2 - M_{ex}^2)^2}\right)^2, \tag{1.4}$$

where q_{ex} is the four momentum of an exchanged particle with mass M_{ex}. The cutoff parameter Λ_M=0.83 GeV was used to reproduce the total cross section data and the Λ_B=1.2 GeV was used with n=1 for the calculation.

Comparing the results of the total cross sections for the $\gamma + p \to K^+ + \Sigma(1385)$ reaction to the CLAS data, Oh *et al.* found the most important contributions are from $\Delta(2000)F_{35}$, $\Delta(1940)D_{33}$, and $N(2080)D_{13}$ as well as the missing resonances $N\frac{3}{2}^-(2095)$ predicted in the quark model. The differential cross sections and the photon beam asymmetries were predicted at E_γ=1.7, 1.8, 1.9 and 2.3 GeV with/without resonance contributions. The missing resonances include $N\frac{3}{2}^-(2095)$, $N\frac{5}{2}^+(1980)$ and $\Delta\frac{3}{2}^-(2145)$. The definition of the photon beam asymmetry as shown in Eq. 1.5 is opposite to the Nam's and LEPS's definition Eq. 1.7:

$$\Sigma = \frac{d\sigma_\parallel/d\Omega - d\sigma_\perp/d\Omega}{d\sigma_\parallel/d\Omega + d\sigma_\perp/d\Omega}, \tag{1.5}$$

where $d\sigma_\parallel/d\Omega$ and $d\sigma_\perp/d\Omega$ are the differential cross sections with linearly polarized photons in the parallel and perpendicular to the reaction plane. The dotted lines in Fig.1.5 shows the results of these theoretical calculations obtained without resonance contributions in the region of E$_\gamma$=1.8−1.9 GeV. The solid and dashed lines indicate the results with PDG resonances and with all resonances, respectively. It was found that these model calculations yield the same results at the higher photon energy region with/without resonances. The differential cross sections have forward peak in all photon energy regions. The similarities can be observed between the solid line(with PDG resonances) and dot-dashed line(with all resonances), and it is difficult to identify the effect of missing resonances. The results show that the role of the resonances can be verified by measuring the photon beam asymmetry. However, it is difficult to identify the role of missing resonances.

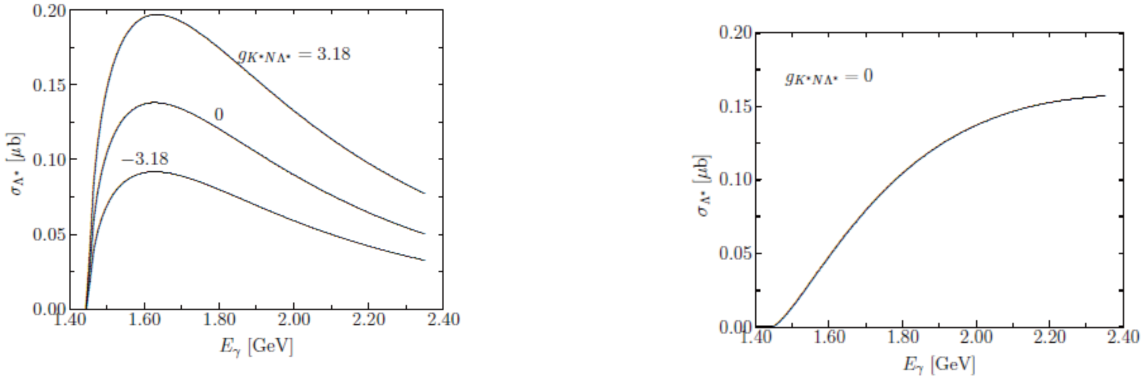

(a) (b)

Figure 1.6: Total cross section of Λ(1405) by changing coupling constants(a) and by changing form factor(b)

The total/differential cross sections and the photon beam asymmetries for Λ(1405) were calculated using effective Lagrangian by Nam *et al.* [32] as shown in Figs.1.6 and 1.7. As shown in Fig.1.6, the total cross sections depend on the $K^*N\Lambda^*$ coupling strength and the form factor structures, and the total cross sections are about 0.1∼0.2 μb near the threshold and decreased slowly beyond E_γ ∼1.6 GeV.

The differential cross sections and the photon beam asymmetries according to $\frac{d\sigma}{dcos\Theta^{K+}_{cm}}$ were calculated with $g_{KN\Lambda^*}$=+3.18 coupling constant by taking three different $g_{K^*N\Lambda^*}$ coupling constants ($g_{K^*N\Lambda^*}$=0,−3.18,+3.18) in the photon energy of 1.45−2.35 GeV as shown in Fig.1.7. The angular dependence shows a mild enhancement in the forward direction due to the K^- exchange in the $t-$channel. The monopole type form factor was adopted for the t-channel K^- and K^* exchanges as Eq. 1.6,

$$F_{\Phi BB} = \frac{\Lambda_h^2 - M_\Phi^2}{\Lambda_h^2 + |k_\Phi|^2}, \tag{1.6}$$

where the subscripts Φ and B stand for the mesonic and the baryonic particles involved with M and k are the mass of the exchanged particle and three momentum for the particles. The cutoff mass Λ_h=650 MeV is used for hadronic form factor.

The photon beam asymmetry can be expressed as Eq. 1.7, which is based on the important physical observations in photoproduction.

$$\Sigma = \frac{d\sigma_\perp/d\Omega - d\sigma_\parallel/d\Omega}{d\sigma_\perp/d\Omega + d\sigma_\parallel/d\Omega}, \tag{1.7}$$

Moreover, the photon beam asymmetry becomes negativel in the forward region(0.5< $cos\theta_{cm}$) with/without K^* exchange contributions. Even though the K^* exchange contributions are included, the value of the photon beam asymmetry does not change. It indicates the K^* exchange has small contributions in the Λ(1405) photoproduction.

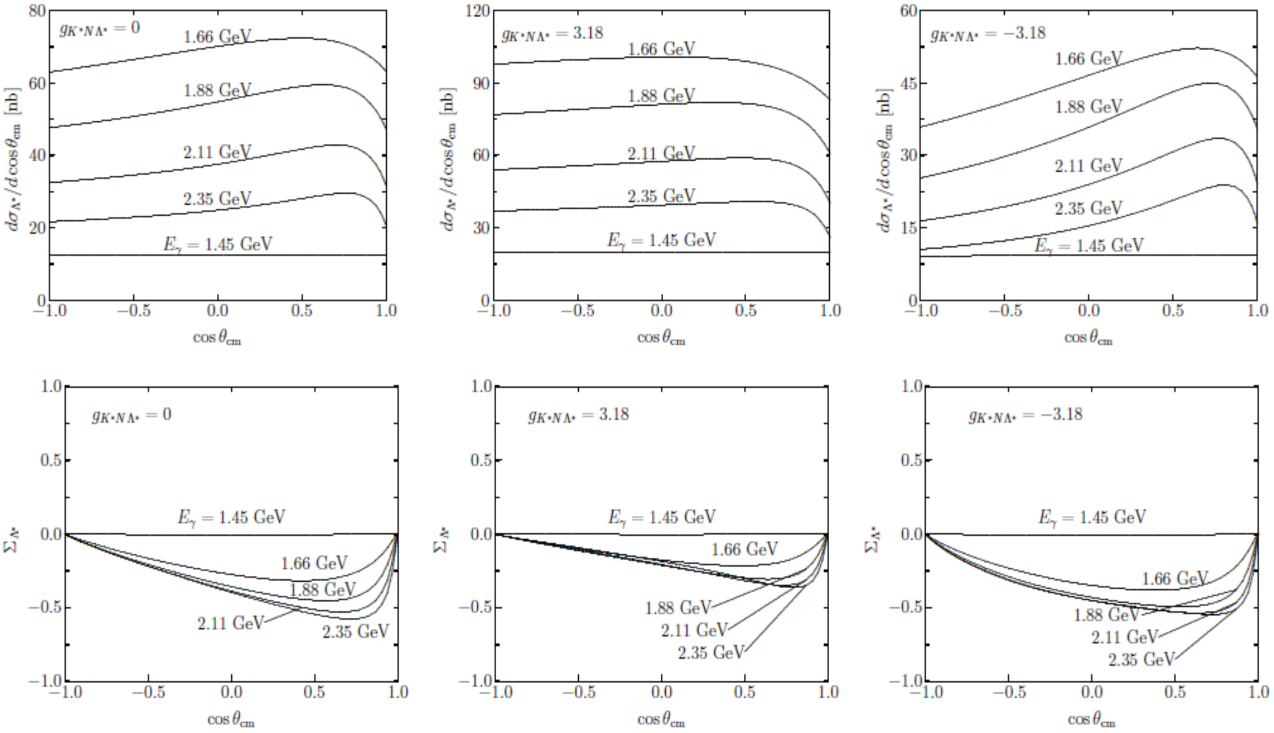

Figure 1.7: Differential cross sections(upper figures) and photon beam asymmetries(bottom figures) for $\Lambda(1405)$ by changing coupling constant at the photon energy ranges of $1.45-2.35$ GeV.

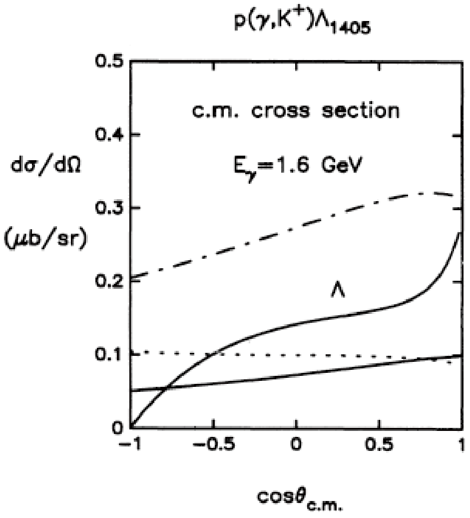

Figure 1.8: The differential cross section of the $\Lambda(1405)$ calculated by Williams *et al.* with $g_{KN\Lambda^*}$=1.5(solid line), 3.0(dot-dashed line), $g_{KN\Lambda^*}$=1.5 and N^* coupling∼0(dotted line)

Williams *et al.* [33] calculated the differential cross section of $\Lambda(1405)$ at E_γ=1.6 GeV with $g_{KN\Lambda(1405)}$=1.5(solid line), 3.0(dot-dashed line), and $g_{KN\Lambda(1405)}$=1.5 and N^* coupling∼0(dotted line) as shown in Fig.1.8. The value of differential cross sections with $g_{KN\Lambda(1405)}$=3.0 is ∼3 times larger than $g_{KN\Lambda(1405)}$=1.5. This model calculation indicates the sensitivity of the differential cross sections to the $KN\Lambda(1405)$ coupling strength and contributions of nucleon resonances from $N^*(1650)$ and $N^*(1710)$.

Lutz and Soyeur [34] calculated the differential cross sections ($d\sigma/dt$) in the region of the $\Sigma(1385)$ and $\Lambda(1405)$ resonances and showed a sharp drop of the differential cross sections($d\sigma/dt$) as increasing $\mid t \mid$. This drop has both double pole and single pole components. The double pole component behaves like $\frac{1}{(t-M_K^2)^2}$ and the single pole component behaves like $\frac{1}{(t-M_K^2)}$. In Fig. 1.9, the solid and dashed lines show the t-dependence of the cross section expected from double and single K$^-$ pole terms, respectively with arbitary normalizations. The data(closed cricles) are from Ref. [24]. The q^2 is the photon virtuality and q_γ^0 is the virtual photon energy. The points at t =−0.18 GeV^2 and t =−0.23 GeV^2 were directly measured by Azemoon. The points corresponding to t =−0.27 GeV^2 and t =−0.37 GeV^2 were measured at q_γ^0∼3.5 GeV and extrapolated to q_γ^0=2.5 GeV by rescaling the differential cross section according to the energy dependence predicted by Lutz and Soyeur's model [34]. They expected that the t-channel exchange with the rapid drop as increasing $\mid t \mid$ is from the dominant double kaon pole term.

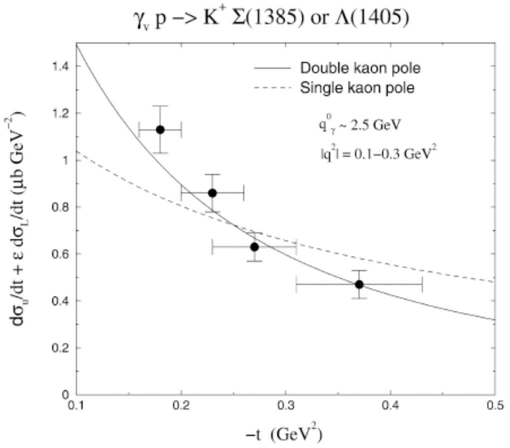

Figure 1.9: t-dependence of the differential cross section with double and single kaon pole contribution at E_γ=2.1 GeV. The data(closed cricles) are from Ref. [24].

1.3 Physics motivation

The main physics motivations in this thesis are to understand the production mechanism of Σ(1385) and Λ(1405) photoproduction by measuring differential cross sections and photon beam asymmetries. The photon beam asymmetry measurement is a good means to investigate the t-channel mechanism because it is possible to decompose the contributions of the exchanged particles. The Σ(1385) hyperon is well established as a q^3 state [10]. On the other hand, there are theoretical models that the Λ(1405) is meson-baryon state strongly coupled with $\bar{K}N$.

In this experiment, we accurately measured the angular dependence of the differential cross sections and the photon energy dependence of the photon beam asymmetries. The photon beam asymmetries provide crucial information on the contribution of the t-channel meson exchange.

There are theoretical model calculations about the contribution of the K^- meson exchange in the t-channel for Λ(1405) and the K^* meson exchange in the t-channel for Σ(1385). Measuring the differential cross sections and the photon beam asymmetries, we can investigate the contribution of the exchanged particles in the t-channel.

In addtion, there are experimental results which show the strong photon energy dependence of the differential cross sections for Λ(1405) in two photon energy regions even in the absence of enough statistics from the LEPS/TPC experiment. We can investigate the angular dependence of Σ(1385)/Λ(1405) at the forward angle region with high statistics.

From the angular distributions, we can expect the possible production mechanism of the $t-$ channel meson exchange for Σ(1385) and Λ(1405). However, it is difficult to conclude the production mechanism for Σ(1385) and Λ(1405) with only the results of the differential cross sections because the angular dependences strongly depends on the coupling, the propagator and the form factor. Therefore, the measurement of the photon beam asymmetries is necessary to understand the production mechanism for Σ(1385) and Λ(1405).

From this experiment, we can know the energy dependence of the photon beam asymmetries at the forward angle region. We expect it will also give interesting results, and we can extract the contribution of the $t-$channel meson exchange(K^- or K^*) for the $\Sigma(1385)$ and $\Lambda(1405)$. Our LEPS experimental results of the photon beam asymmetries for $\Sigma(1385)/\Lambda(1405)$ are the first measurement in the world and important to understand the production mechanism of $\Sigma(1385)$ and $\Lambda(1405)$.

Since two particles of $\Sigma(1385)$ and $\Lambda(1405)$ are overlapped in the K^+ missing mass spectra with large decay widths, it is difficult to distinguish $\Sigma(1385)$ and $\Lambda(1405)$. However, high statistical data at the LEPS forward angle provide precise information of the t-channel meson exchange. The LEPS spectrometer have a very good forward angle coverage which proper to search the $t-$ channel process, while other experiments have poor forward angle coverage. There are other experimental data by JLAB/CLAS collaboration and the theoretical calculations. The discrepancies between the experimental data and the theoretical calculation have been studied with experimental data.

1.4 Photon beam asymmetry

The photon beam asymmetry measurement is a good way to distinguish the $t-$channel meson exchange in the production mechanism. The horizontally and vertically polarized photon beams were used to measure the photon beam asymmetry. The photon beam asymmetry was measured in the dimension of K^+ azimuthal angle and it was obtained by the relation with the production yields shown in Eq. 1.8.

$$\frac{nN_V - N_H}{nN_V + N_H} = P\Sigma cos(2\phi_{K+}), \tag{1.8}$$

where N_H is the K^+ photoproduction yield with the horizontally polarized photons and N_V is the K^+ photoproduction yield with the vertically polarized photons. A $n(=\frac{n_h}{n_v})$ is the normalization factor which was obtained by using the number of the horizontally polarized photons(n_h) and the vertically polarized photons(n_v).

The photon beam asymmetry is related with the spin and parity of the exchanged particles. If the photon beam asymmetry gives a positive value(+1), then the natural parity(K^*) exchange is dominant and indicating the K^+ photoproduction yield with the vertically polarized photons is large. If the photon beam asymmetry gives a negative value(−1), then the unnatural parity(K^-) exchange is dominant and indicating the K^+ photoproduction yield with the horizontally polarized photons is large [35].

The experimental setup of SPring-8/LEPS will be described in Chapter 2, and the data analysis and the event selections will be discussed in Chapter 3. The results of the differential cross sections and the photon beam asymmetries will be presented in Chapter 4. In Chapter 5, we will have conclusions and discussions about the results, and finally we will present the summary of this thesis in Chapter 6.

Chapter 2

Experiment

The $\Sigma(1385)/\Lambda(1405)$ photoproduction exepriment has been carried out at Laser-Electron-Photon beam line at the Super-Photon ring-8 GeV(SPring-8/LEPS) facility, in Japan. Differential cross sections and photon beam asymmetries for the $\mathrm{p}(\gamma,\mathrm{K}^+)\Sigma(1385)/\Lambda(1405)$ reaction have been measured in the photon energy regions from 1.5 to 2.4 GeV by using a linearly polarized photon beam which was produced by the backward Compton scattering. In this chapter, the LEPS facility which consists of a laser system and a photon tagging system and a LEPS spectrometer which consists of a liquid hydrogen target system and a charged partice spectrometers, are described in detail.

2.1 SPring-8 facility

SPring-8(Super-Photon ring-8 GeV) [36], the world's largest 8-GeV third-generation synchrotron radiation facility, provides the powerful synchrotron radiation among the currently available facilities. Synchrotron radiation is an electro-magnetic wave emitted from an electron

Figure 2.1: A bird's eye view of SPring8

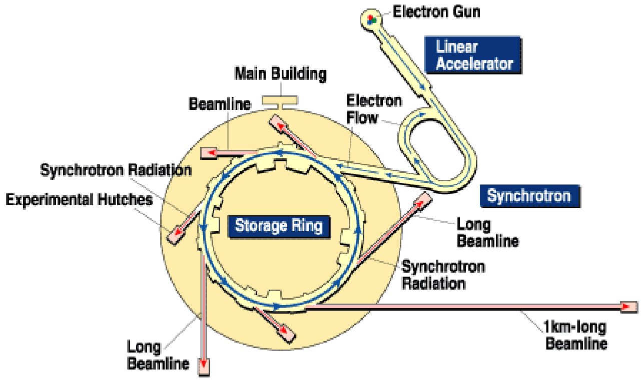

Figure 2.2: Schematic view of the accelerator complex of SPring-8.

traveling at near the speed of light, toward its running-direction when its path is bent by a magnetic field. Fig. 2.1 shows a bird's eye view of SPring8.

The SPring-8 accelerator complex is comprised of an injector linac(linear accelerator), a booster synchrotron, and a low-emittance and high-brightness storage ring. There are 57 beamlines available for scientific research activities and the laser-electron-photon facility was built at the BL33LEP beamline.

Fig. 2.2 shows the schematic view of the accelerator complex of SPring-8. The linac accelerator is used as an injector into the booster synchrotron. The electron beam is generated by a electron gun and the extracted beam is accelerated to an energy of 1-GeV in the injector linac with a length of 140 m. The electron beam from the linear accelerator is accelerated up to 8-GeV by the booster synchrotron with a 396 m circumference. The 8-GeV electron beam is injected from the booster synchrotron into the storage ring with a 1436 m circumference. The 8-GeV electrons circulate in the storage ring. The time interval of the successive bunches for electrons is 1.966 nsec. Electrons are filled in some bunches with various filling patterns. The maximum current of the 8-GeV electron beam is 100 mA.

2.2 LEPS facility

The Laser-Electron-Photon facility at SPring-8 (LEPS), a multi-GeV photon beam is produced by backward Compton scattering (BCS) of laser photons from the circulating 8-GeV electrons [37–41]. The LEPS beam line is used for the experiments of nuclear and hadron physcis [7, 8, 21, 42–54].

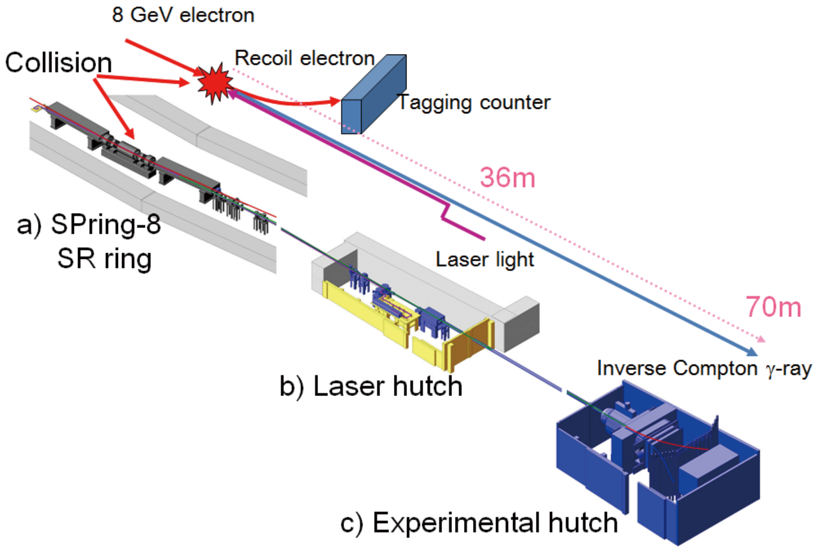

Figure 2.3: Schematic view of the LEPS facility at SPring-8. The facility consists of three parts;(a) laser-electron collision part in the storage (SR) ring, (b) laser hutch for a laser injection, and (c) experimental hutch where a spectrometer is placed.

2.2.1 Backward Compton scattering

The kinematics of the backward-Compton-scattering process in the laboratory system are described in this section.

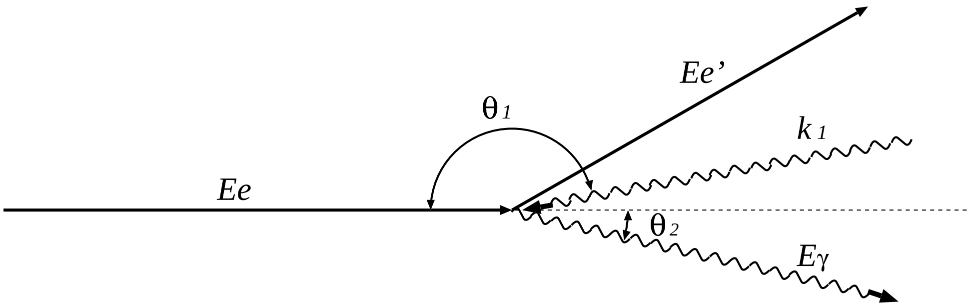

Figure 2.4: Kinematical variables of the backward-Compton-scattering process in the laboratory frame.

Fig. 2.4 shows kinematical variables of the backward Compton scattering process in the laboratory frame. E_e is an incident electron energy, k_1 is a laser photon energy, $E_{e'}$ is a recoiled electron energy, and E_γ is a BCS photon energy. If a laser photon energy(k_1) interacts with a high energy electron(E_e) and a relative angle $\theta_1 \simeq 180°$, it is scattered with a scattering angle of θ_2, where $\theta_1(\theta_2)$ is a polar angle between an incident electron direction and a laser photon(outgoing scattering photon) direction. If $E_e \gg k_1$, the scattered photon is directed strongly in the backward direction due to the Lorentz boost.

Based on the energy-momentum conservation, the energy of a BCS photon E_γ is depicted as

$$E_\gamma = k_1 \frac{1 - \beta cos\theta_1}{1 - \beta cos\theta_2 + \frac{k_1(1-cos\theta)}{E_e}}, \tag{2.1}$$

where β is an incident electron velocity in a unit of the speed of light and $\theta = \theta_2 - \theta_1$. Assuming $\gamma = E_e/m_e \gg 1$, $\beta \simeq 1$, $\theta_1 \simeq 180°$ and $\theta_2 \ll 1$, Eq. (2.1) can be rewritten as

$$E_\gamma = \frac{4E_e^2 k_1}{m_e^2 + 4E_e k_1 + \theta_2^2 \gamma^2 m_e^2}, \tag{2.2}$$

where m_e is the electron mass of 0.511 MeV and $\gamma \sim 16,000$ at $E_e = 8$GeV. The maximum energy of a BCS photon (Compton edge) is obtained at $\theta_2 = 0°$:

$$E_\gamma^{max} = \frac{4E_e^2 k_1}{m_e^2 + 4E_e k_1}. \tag{2.3}$$

The maximum energy E_γ^{max} is shown in Fig. 2.5 as a function of an incident electron energy E_e. A linear-polarized photon beam was produced by an Ar laser with a 351 nm wavelength in the experiment. The energy spectrum and the beam profile of the BCS photon beam were measured by a PWO ($PbWO_4$) crystal calorimeter which was placed in 42.8 m far from the center of the straight section in the laser hutch [55]. Fig. 2.6 shows the energy spectrum of the BCS photon beam, which demonstrates that high energy photons with E_γ^{max}=2.4 GeV are produced by the BCS process. The energy spectrum of the Bremsstrahlung beam created in the residual gas in the storage ring is also plotted in Fig. 2.6. The maximum energy of the Bremsstrahlung beam is 8 GeV corresponding to the electron beam energy.

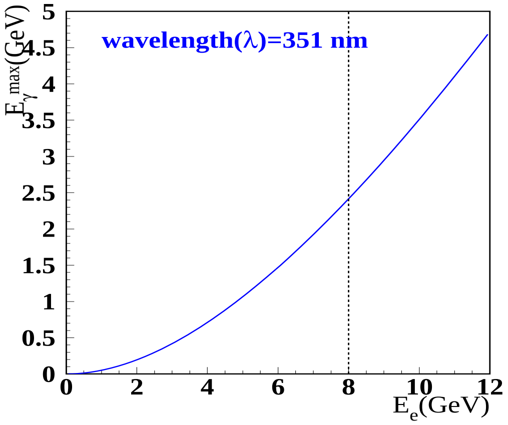

Figure 2.5: Maximum energies of BCS photons as a function of the incident electron energy for laser photons with 351 nm wavelengths

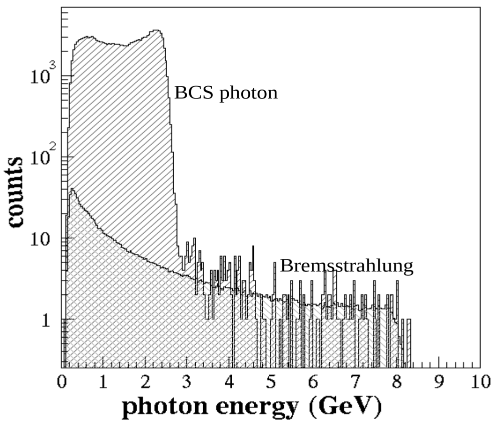

Figure 2.6: Energy spectrum of the BCS photon measured by a PWO crystal calorimeter [55]. The wavelength of laser photons is 351 nm.

The differential cross section of the BCS process is written as a function of the BCS photon energy [56]:

$$\frac{d\sigma}{dE_\gamma} = \frac{2\pi r_e^2 a}{E_\gamma^{max}}(\chi + 1 + cos^2\alpha) \tag{2.4a}$$

$$a = \frac{m_e^2}{m_e^2 + 4E_e k_1} \tag{2.4b}$$

$$\chi = \frac{\rho^2(1-a)^2}{1-\rho(1-a)} \tag{2.4c}$$

$$cos\alpha = \frac{1-\rho(1+a)}{1-\rho(1-a)} \tag{2.4d}$$

$$\rho = \frac{E_\gamma}{E_\gamma^{max}} \tag{2.4e}$$

where $r_e = 2.818$ fm is the classical electron radius. Fig. 2.7 shows the differential cross sections for the BCS process between 8 GeV incident electrons and laser photons with 351 nm wavelength.

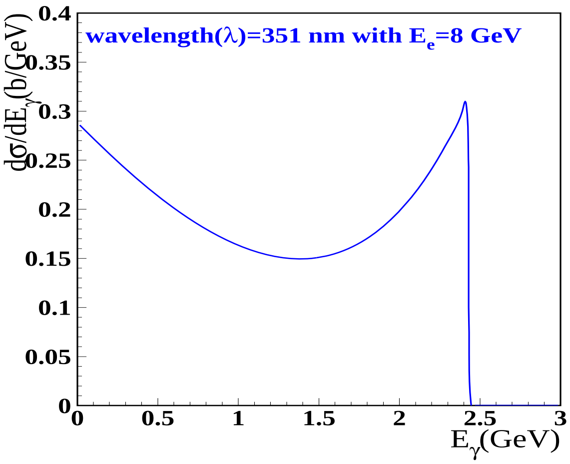

Figure 2.7: Differential cross sections of the BCS process with the 8 GeV incident electron beam for laser photons of 351 nm wavelengths.

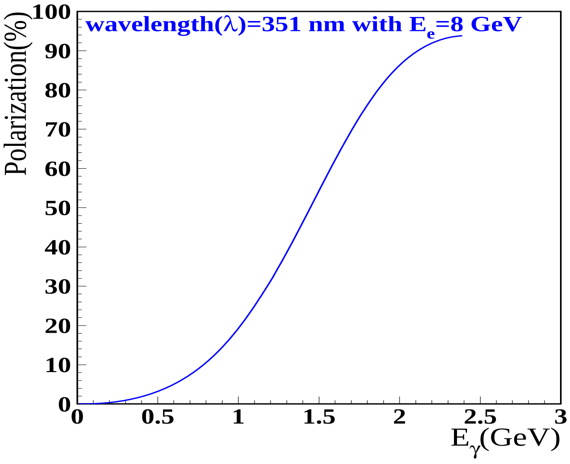

Figure 2.8: Linear polarization of the BCS photon as a function of E$_\gamma$ when the laser photon is 100% polarized for the 351 nm wavelength with the 8 GeV incident electron beam.

The linearly polarized BCS photons can be produced by using linear polarized laser photons. The degree of polarization (P_γ) of a BCS photon is proportional to that of a laser photon (P_{laser}) [56] and given by

$$P_\gamma \;=\; P_{laser}\frac{(1-cos\alpha)^2}{2(\chi+1+cos^2\alpha)}. \tag{2.5}$$

Fig. 2.8 shows the linear polarizations of a BCS photon as a function of E_γ and the laser photon is 100% polarized for the 351 nm wavelength with the 8 GeV incident electron beam. In the case of the linear polarization, the maximum polarization is obtained as $P_\gamma = P_{laser}\frac{2a}{1+a^2}$ from Eq. (2.5). The linear polarization is about 94% at the maximum energy when the incident electron with E_e = 8 GeV and a 351-nm laser with 100% polarization are used.

2.2.2 Laser system

Fig. 2.9 shows a schematic view of the laser operation system. The operating system consists of an Ar laser, a half-wave-length plate ($\lambda/2$ plate), a beam expander, four mirrors and a polarization monitor. The direction, shape, and polarization of laser photons are controlled by this system to achieve a high intensity and a high polarization of the BCS photon beam. The Ar laser passes through the $\lambda/2$ plate to change its polarization direction. The shape of the laser beam is tuned by the beam expander. The direction and position of the laser beam are tuned by the third and forth mirrors. The laser beam is transferred to the beam line by the first and second mirrors. The polarization direction(angle) and degree are obtained by a polarization measuring system consisting of a Glan-laser prism and photodiode at the end of

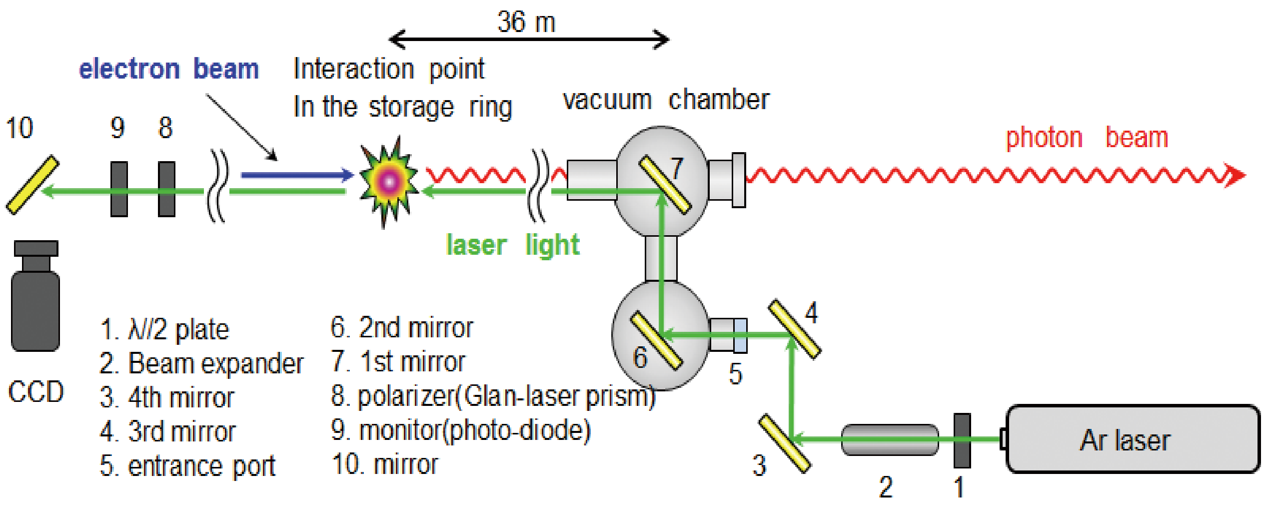

Figure 2.9: Schematic view of the laser operation system.

straight section in the storage ring. The Glan-laser prism is rotated, and the intensity of the laser light is measured behind the prism with a photodiode as a function of a rotation angle of the polarizer.

Figs. 2.10(a) and (b) show the intensity distribution measured by the photodiode for vertically and horizontally polarized laser photons. The data is fitted by a function of sinϕ. The polarization angle and degree are determined by this fitting. The laser beam is optimized to have the maximum polarization.

Specifications of the elements used in the laser system are listed in Table 2.1.

Table 2.1: Specifications of elements used in the LEPS laser system.

	Manufacture name (company)	Material	Size (mm)
Ar laser	Coherent Innova Sabre (Coherent)	-	-
$\lambda/2$ plate	for 351 nm (SURUGA)	Quartz	$17\times17\times2$t
Beam expander	(SURUGA)		
4th mirror	optical mirror (OPTO·LINE)	Quartz	$\phi 80 \times 12$t
3rd mirror	optical mirror (OPTO·LINE)	Quartz	$\phi 80 \times 12$t
2nd mirror	optical mirror (FUJITOKU)	Si (Aluminum)	$\phi 100 \times 19$t
1st mirror	optical mirror (FUJITOKU)	Si (Aluminum)	$\phi 100 \times 6$t
Glan-laser prism	PGL8310 (OptMax)	α-BBO	$\phi 10 \times 26$t
Photo diode	S1406-05(HAMAMATSU)	-	-

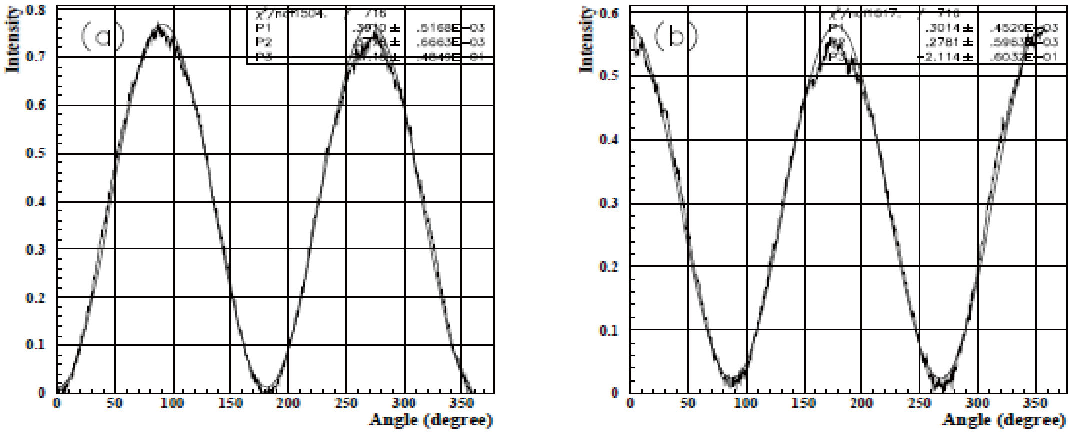

Figure 2.10: Intensity distribution of the laser beam measured by the photodiode for (a) vertically polarized laser photons and for (b) horizontally polarized laser photons. The distribution is fitted by a function of sinϕ. The line is the fitting function.

2.2.3 Tagging system

The energy E_γ of the BCS photon beam is determined by the recoiled electron energy $E_{e'}$ as

$$E_\gamma = E_e - E_{e'}, \tag{2.6}$$

where E_e is an energy of the electron beam in the storage ring and the energy was determined as 7.975 ± 0.003 GeV. The recoiled electrons($E_{e'}$) are detected with the tagging counter which is installed at the downstream of the bending magnet in the storage ring. They pass through the bending magnet, and their trajectory is bent to be deviated from the normal 8-GeV electrons orbit.

Fig. 2.11 shows the schematic view of the tagging system(tagger). The tagging system is placed at the outside of a beam vacuum chamber for the 8 GeV electron beam. The tagging system covers a region 4.5−6.5 GeV in the energy of the recoil electrons. This energy region corresponds to the energy of the BCS photons, 1.5−3.5 GeV. The lower limit of 1.5 GeV is due to the fact that the tagging system can't be positioned closer to the nominal orbit of the 8 GeV electrons. The tagging system consists of plastic scintillator (PL) hodoscopes and silicon strip detectors (SSD's) as shown in Fig. 2.11. There are two layers of the combination of the PL hodoscope and the SSD. Each PL hodoscope layer consists of 10 plastic scintillation counters. The size of the plastic scintillator is 10.0 mm high, 7.4 mm wide, and 3.0 mm thick. The plastic scintillators are stacked with an overlap of 1.0 mm as illustrated in Fig. 2.11. The PMT (HAMAMATSU R1635P) with a 3/8 inch diameter is coupled to the plastic scintillator through a light guide. The size of the SSD is 10.0 mm high, 51.2 mm wide, and 0.5 mm thick.

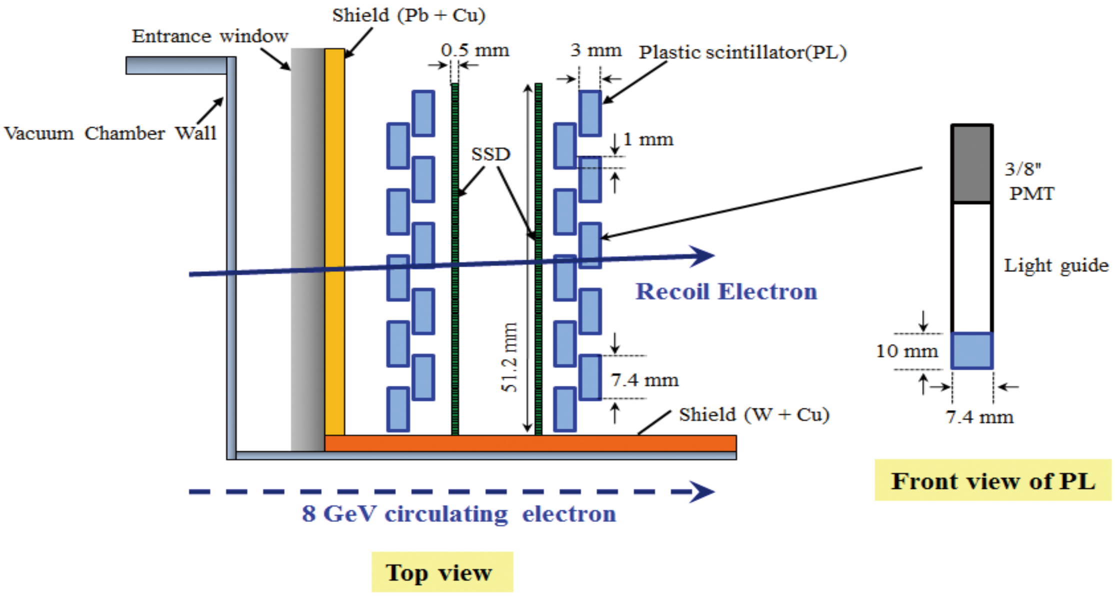

Figure 2.11: Schematic view of tagging system.

The strip pitch is 0.1 mm. There are 512 strips in total.

2.3 LEPS spectrometer

The LEPS spectrometer is located in the experimental hutch to identify charged particles produced at the target. Fig. 2.12 shows the LEPS spectrometer. The incidence direction of the photon beam is displayed in Fig 2.12. The LEPS spectrometer consists of a upstream-veto counter, a trigger counter, a silica-aerogel Čerenkov counter, a vertex detector (silicon strip detectors), a dipole magnet, three drift chambers (DC1, DC2 and DC3), and a TOF wall. The charged particles produced at the target are measured by the trigger counter. The silica-aerogel Čerenkov counter is used to eliminate the e^+e^- background events. The vertex detector and three drift chambers are used as tracking devices with the dipole magnet to measure momenta

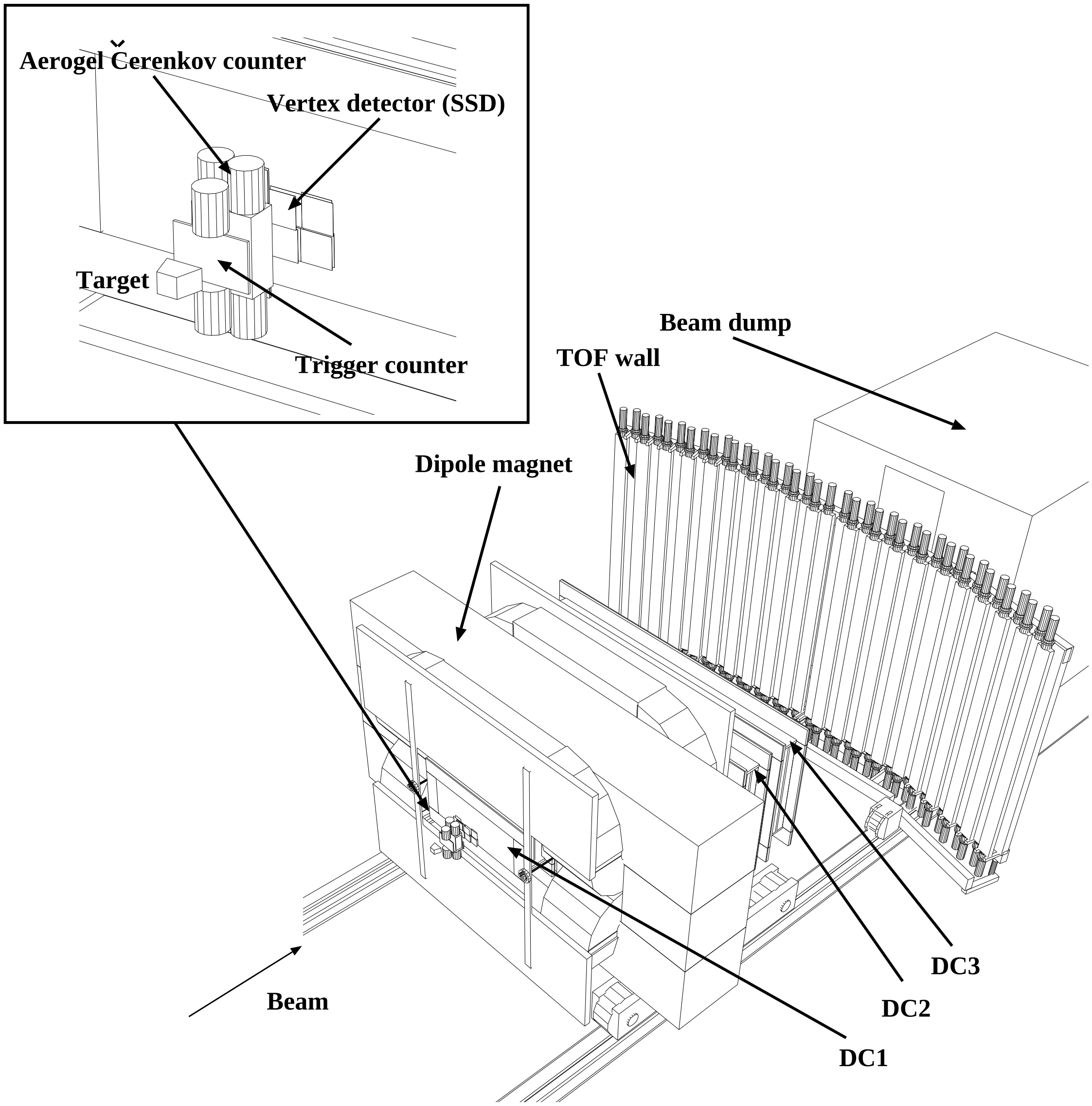

Figure 2.12: Overview of the LEPS spectrometer.

of the charged particles. A time-of-flight is measured by using the TOF wall. A beam dump is placed behind the spectrometer for the purpose of a radiation shielding.

2.3.1 Upstream-veto counter

An Upstream-veto counter is used to reject the e^+e^- pair production in air, the residual gas or Al windows of the beam pipe. These charged particles should be eliminated before the target.

2.3.2 LH_2 target

A 150 mm long liquid hydrogen(LH_2) target was used for this experiment.

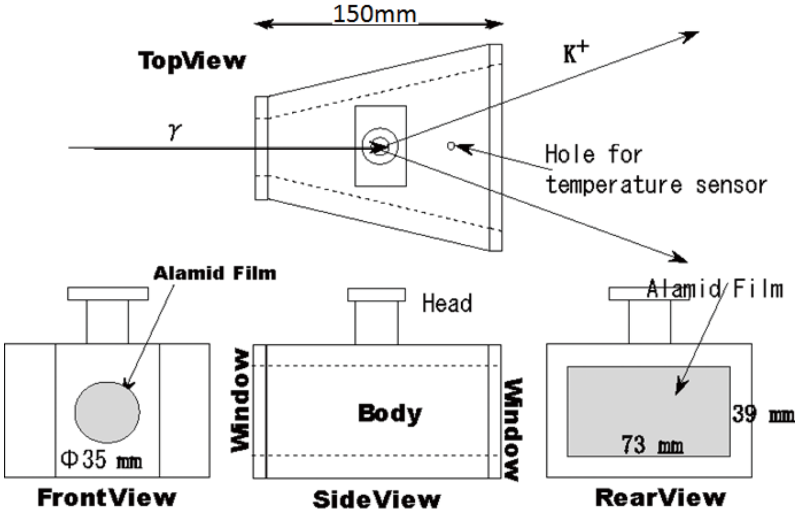

Figure 2.13: Schematic view of a target cell. A sample trajectory for the p(γ,K^+)X reaction is illustrated.

Fig 2.13 shows a schematic view of a target cell. The target cell was made of copper with a thickness of 8 mm. The entrance and exit windows of the tagrget cell were made of Aramid films with a thickness of 125 μm. The LH_2 target was located at 995 mm upstream of the center of the dipole magnet. The temperature and pressure of the target were kept at 20.5 K and 1.05 atm, repectively.

2.3.3 Trigger counter

The charged particles from the target are measured using a trigger counter. The trigger counter is used to determine a start timing of the trigger in the data taking. The size of a plastic scintillator(BC-408) is 94 mm height, 150 mm width, and 5 mm thickness.

2.3.4 Silica-aerogel Čerenkov counter (AC)

Main background events for the TRG in a measurement of hadronic reactions are the e^+e^- pairs produced at the LH_2 target.

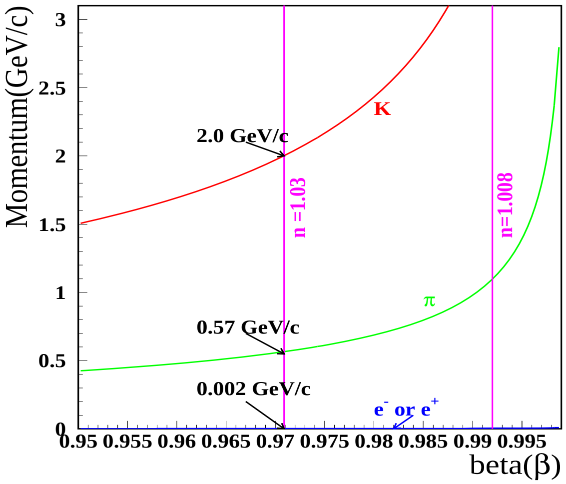

Figure 2.14: Relation between momentum and β for e^+e^-, π and K. A particle with $\beta > 1/n$ emits Čerenkov lights. The line is corresponding to an index of 1.03.

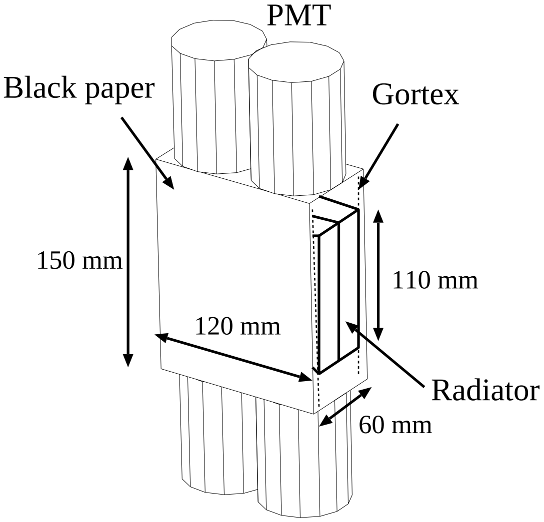

Figure 2.15: Schematic view of the silica aerogel Čerenkov counter (AC).

Fig. 2.14 shows the relation between the momentum and the velocity (β) of e^+e^-, pion and kaon. When a particle with a velocity $\beta > 1/n$ passes through a transparent material with a refractive index n, Čerenkov light is emitted. The Čerenkov thresholds for e^+e^-, pion and kaon are 0.002 GeV/c, 0.57 GeV/c and 2.0 GeV/c, respectively. Čerenkov light is collected at the photocathode of a PMT. The signal is used as a veto signal in the trigger logic. Pion events with a high momentum are rejected by the AC veto signals. However, pions and kaons with momenta around the Čerenkov threshold are not rejected due to the small number of Čerenkov light.

The AC is installed just behind the trigger counter to detect both an electron and a positron simultaneously. Fig. 2.15 shows a schematic view of a silica aerogel Čerenkov counter(AC). The size of the counter box is 150 mm height, 120 mm width, and 60 mm thickness. The box is made of a black paper. The size of the silica aerogel radiator is 110 mm height × 110 mm width, and 25 mm thickness. Two sheets of the radiators are inserted into the AC box as shown in Fig. 2.15. The collected light is read by four 2-inch fine-mesh PMTs (Hamamatsu H6614-01) which are coupled to the upper and the lower sides of the box.

2.3.5 e^+e^- Blocker

The e^+e^- blocker is used in the dipole magnet. The schematic view of the e^+e^- blocker is shown in Fig. 2.16.

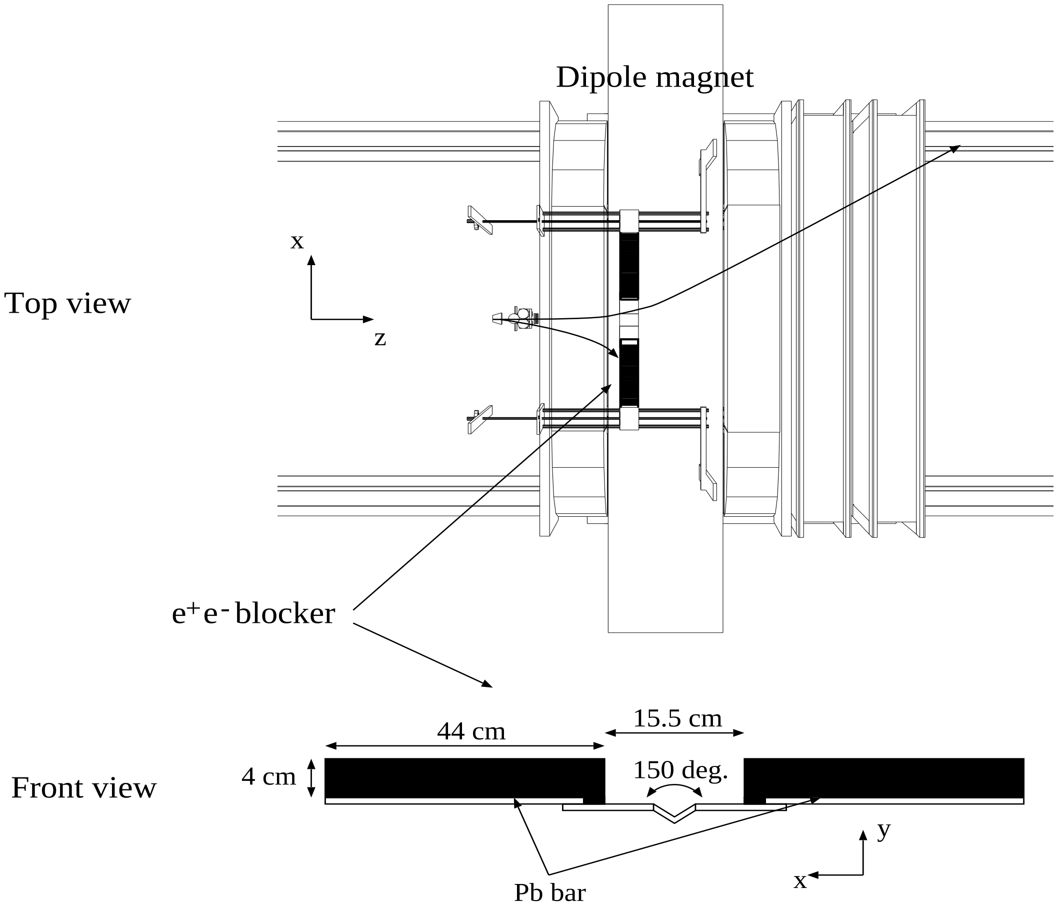

Figure 2.16: Drawing of the e^+e^- blocker.

The e^+e^- blocker with two lead bars is placed 20 cm downstream of the center of the dipole magnet. The size of each Pb bar is 4 cm height, 44 cm width, and 10 cm thickness. The gap distance between two Pb bars is 15.5 cm. The e^+e^- particles above 1 GeV/c momentum can go through the gap.

2.3.6 Dipole magnet

A dipole magnet is used as a momentum analyzer magnet to bend charged particles. The magnet is placed at the center of the spectrometer. The magnet has an aperture with 55 cm height and 135 cm width. The length of the pole along the beam is 60 cm.

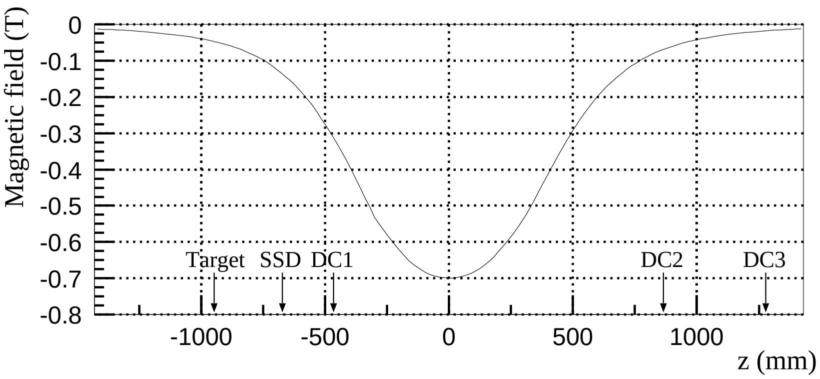

Figure 2.17: Distribution of the magnetic field B_y as a function of the z-position at x=0 and y=0. The position of z=0 corresponds to the center of the dipole magnet.

Fig. 2.17 shows the distribution of the magnetic field B_y along the y-direction as a function of the z-axis at x=0 and y=0. We used the TOSCA simulation program to obtain the distribution. The magnetic field was measured with a hole probe and the measured distribution was compared with the result obtained by the TOSCA simulation. They show a good agreement and then we used the distribution of the magnetic field obtained by TOSCA in tracking. The direction of the magnetic field is from up to down. The strength of the magnetic field is 0.7 T at the center when the current is set at 800 A.

2.3.7 Vertex detector (SVTX)

A vertex detector (SVTX) is used to determine a trajectory of a charged particle with drift chambers and determine a vertex point with a high precision by the track position close to the target. The SVTX is placed just after the AC. Fig. 2.18 shows the front view of the SVTX. The SVTX consists of two layers of silicon strip detectors (SSD's). One of the layers is used to measure a x-position and the other is used to measure a y-position. The strip pitch is 0.12 mm and the thickness is 0.3 mm. The SVTX has a rhombic-shaped hole for the beam path which is 10 mm × 10 mm in size.

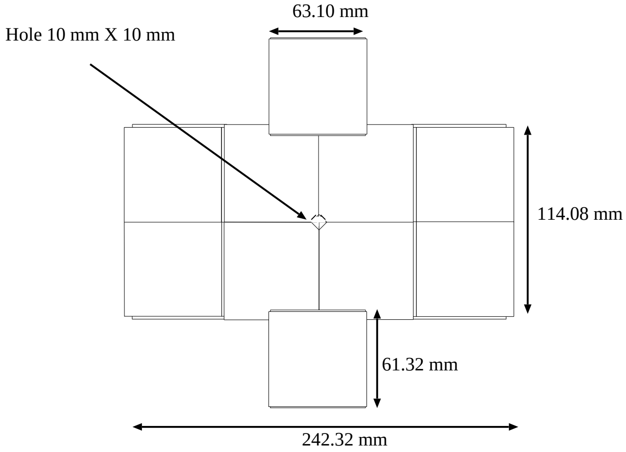

Figure 2.18: Front view of the SVTX.

2.3.8 Drift chambers

A tracking of a charged particle is performed by using hit information from the SVTX and three MWDCs (multi wire drift chambers(DC1, DC2, and DC3)). DC1 is located upstream of the dipole magnet. It has the active area of 600 mm × 300 mm.

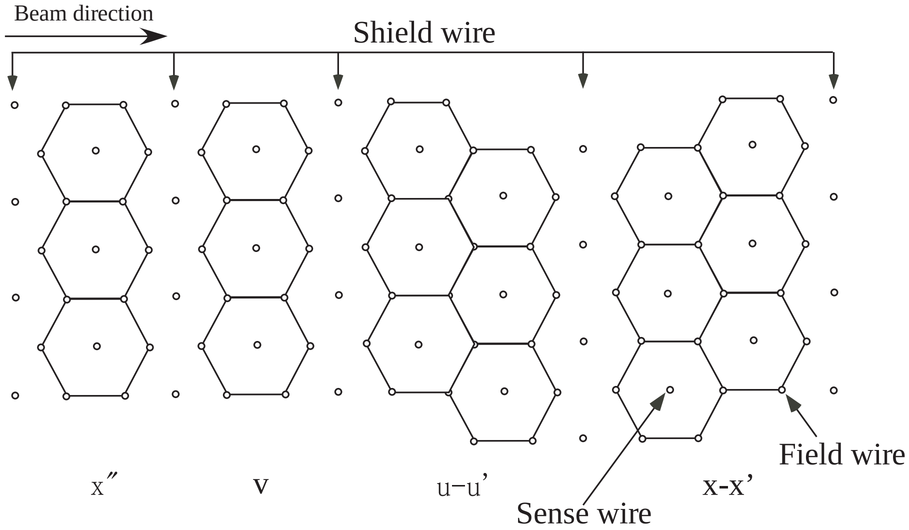

Figure 2.19: Drawing of field, shield and sense wires in the multi wire drift chamber, DC's.

Fig. 2.19 shows a drawing of field, shield and sense wires in DC1. DC1 has 6 planes, x, x', u, u', v and x". The x" wires are added because a charged particle begins to be spread out by the magnetic field in DC1. The sense wires of x-x' and u-u' are positioned with a 6 mm spacing and the wires of x" and v are positioned with a 12 mm spacing. The field wires are arranged in a hexagonal shape. The shield wires are positioned along the windows to shape the electric field. The inclination angle of the u and v wires is 45° with respect to the horizontal plane. DC2 and DC3 are installed downstream of the dipole magnet and have the active area of 2000 mm × 800 mm. Both DC2 and DC3 have 5 planes, x, x', u, u' and v. The design of DC2 and DC3 is the same as DC1 as shown in Fig. 2.19, but there is no x" wires in DC2 and DC3. The sense wires of x-x' and u-u' are positioned with a 10 mm spacing, and the wires of v are positioned with a 20 mm spacing. The u and v directions are inclined by 30° with respect to the 10 mm spacing, and the wires of v are positioned with a 20 mm spacing. The u and v directions are inclined by 30° with respect to the vertical plane. The material of the sense wires is gold-plated tungsten (Au-W) and the wire diameter is 25 and 30 μm for DC1 and DC2, DC3, respectively. The field and shield wires are made of Au-BeCu with a diameter of 100 μm. The windows are made of mylar with a thickness of 125 μm. The design parameters of the DC's are shown in Table 2.2.

Table 2.2: Design parameters of the MWDC's. The location of the center of

	Coordinate	Orientation	Number of	Wire spacing	Active area
DC1	x-x'	0°	48	6	600 × 300
	u-u'	45°	48	6	
	v	135°	48	12	
	x"	0°	48	12	
DC2	x-x'	0°	104	10	2000 × 800
	u-u'	120°	78	10	
	v	60°	79	20	
DC3	x-x'	0°	104	10	2000 × 800
	u-u'	120°	78	10	
	v	60°	79	20	

The gas mixture used to operate the DC's is 70 % argon and 30 % isobutane. The position resolution of the DC's is approximately 200 μm.

2.3.9 TOF wall

Time-of-flights of charged particles are measured by a TOF wall. The TOF wall is placed downstream of the DC3 with a full angular coverage of the LEPS spectrometer.

Fig. 2.20 shows a schematic view of the TOF wall and a drawing of a TOF counter. The TOF wall consists of 40 plastic scintillator bars (BC-408). The size of a plastic scintillator bar (TOF counter) is 200 cm length, 12 cm width, and 4 cm thickness. Two 2-inch PMTs(Hamamatsu H7195) are attached to both sides through a light guide with a thickness of 3 cm. Each bar is overlapped with adjacent bars by 1 cm. Sideway bars are aligned in the planes tilted by ± 15 degrees as shown in the top view of Fig. 2.20. Ten bars are arranged in the right side and other ten bars are placed in the left side. A 4-cm gap between two TOF counters at the center allows the photon beam to pass through. The TOF wall is movable on the rails between 1.5 m and 4.5 m away from the center of the dipole magnet. In the present

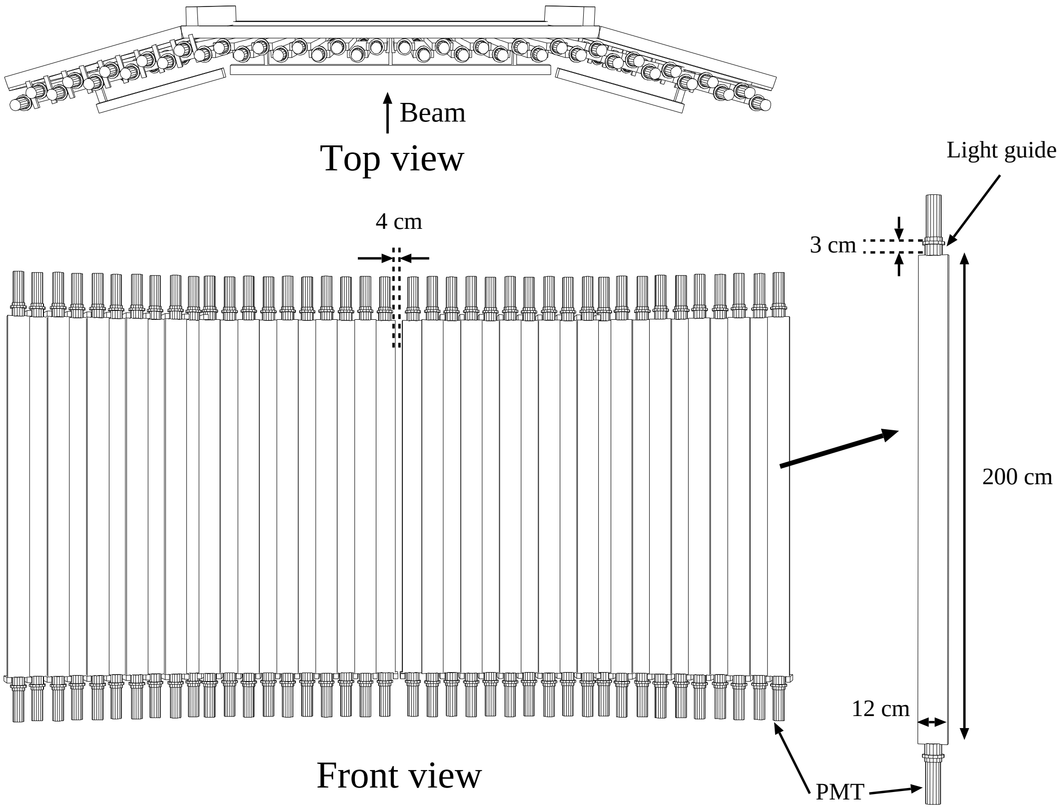

Figure 2.20: Drawing of the TOF wall.

experiment, the z-position of the TOF wall was set at 3151.5 mm away from the center of the dipole magnet.

2.3.10 RF signal

The 508 MHz radio frequency(RF) system is used in the 8-GeV storage ring to recover the energy loss of circulating electrons due to synchrotron radiation. A time interval of the successive bunches of the RF to accelerate the electrons is 1.966 nsec. The RF signal is used to determine a start timing for the time-of-flight measurement.

2.3.11 Trigger

The triggers for data acquisition are defined as

$$\begin{aligned} HadronTrigger &= TAG \cdot \overline{UPveto} \cdot TRG \cdot \overline{AC} \cdot TOF, && (2.7) \\ e^+e^-Trigger &= TAG \cdot \overline{UPveto} \cdot TRG \cdot TOF, && (2.8) \end{aligned}$$

Fig. 2.21 shows a diagram of the trigger logic.

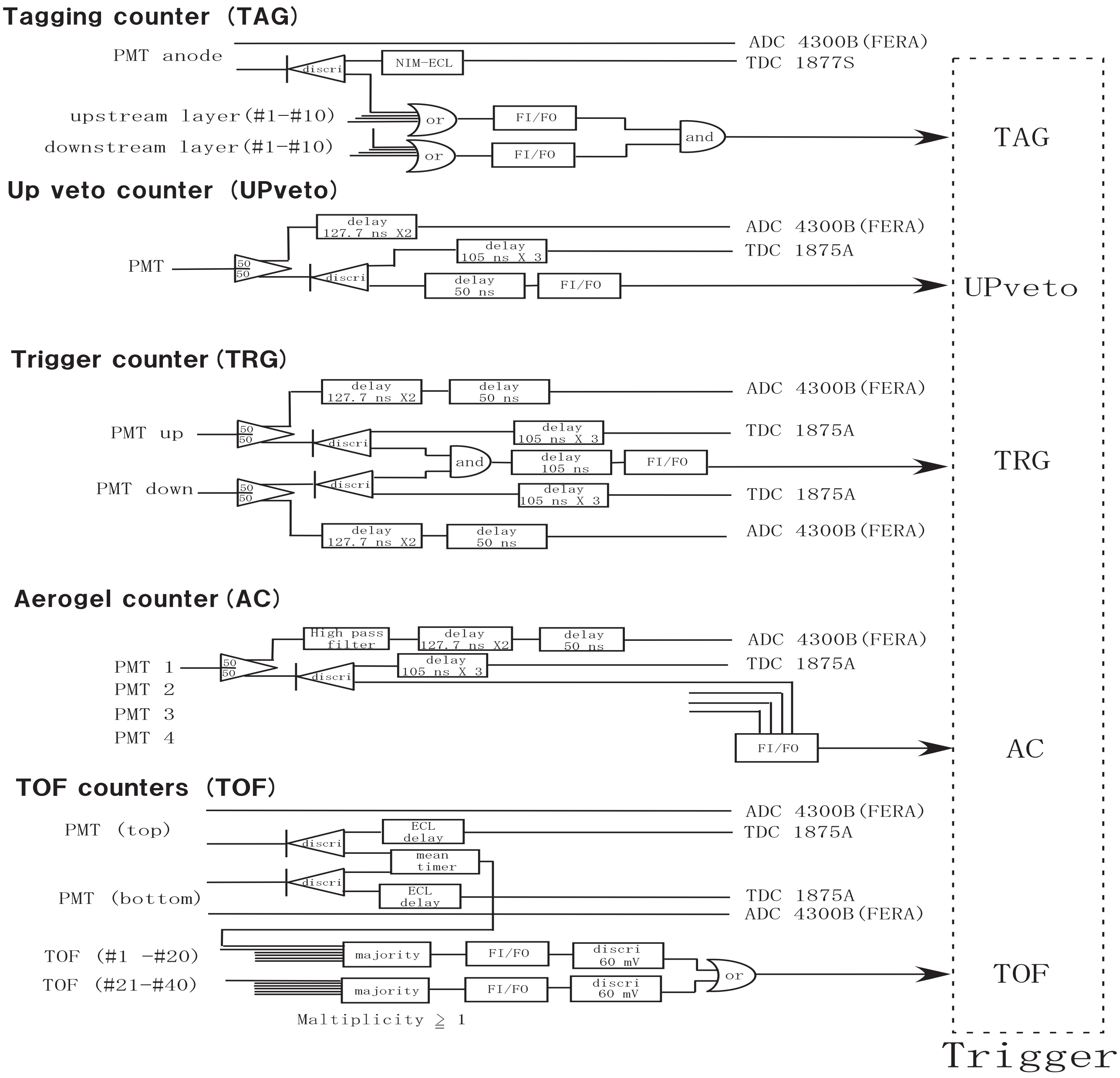

Figure 2.21: Diagram of the readout circuits for triggers.

Chapter 3

Data analysis for the $\vec{\gamma} + p \rightarrow K^{+} + \Sigma(1385)/\Lambda(1405)$

3.1 Data summary

The experiment was carried out from May 2002 to April 2003 with the 16 cm target length of long liquid hyrogen target(LLH2). The data were taken with these run numbers :

Cycle I ; r23690(2002.5.23)−r24058(2002.7.9)
Cycle II ; r25453(2003.2.27)−r25968(2003.4.13)

The ratio for the number of photons was measured as 45.6% at horizontally polarized photon beam and 54.4% at vertically polarized photon beam. All good runs were used for the $\Sigma(1385)$ and $\Lambda(1405)$ analysis.

The filling patterns and the run number are summarized as follows :

1. 23690-23807 : 29*(11-bunch train)
2. 23808-23834 : 160 bunch train*(12-1)
3. 23835-23922 : 203 bunches-4bunchesx7
4. 23923-23981 : 160 bunch train*(12-1)
5. 23982-24059 : 2/21 fill + 18 single bunches
6. 25451-25750 : 160 bunch train *(12-1)
7. 25811-25910 : 203 bunches-4bunchesx7
8. 25911-25968 : 160 bunch train *(12-1)

3.2 Event selection for K^{+} particles

The K^{+} events were selected with the standard cuts which are described below in this section. The number of the survived K^{+} events with the standard cut conditions is summarized in Table 3.1 and their K^{+} missing mass spectra are shown in Fig. 3.1.

Cuts	Horizontal	Vertical	Horizontal +Vertical	Comments
Analyzed	47870251	48133392	96003643	
Skimed K^+	2241512	2243252	4484764	
(ntag=1.or.2)&itagc.f>0	1704978	1720581	3425559	
PID (K^+)	532780	642849	1175629	3σ cut
DecayInFlight	489680	596283	1085963	
e^+e^-	408999	519234	928233	-30>ybar.or.ybar>16
z-vertex	290279	372793	663072	-1200<vtz<-900
usual tagger	284878	365610	650488	npl(1)=0.or.npl(2)=0
tight tagger	259054	333324	592378	npl(1)=0.and.npl(2)=0
MMcut				
$\Sigma(1385)\Lambda(1405)$	236753	306063	542816	$0.6<\cos\theta_{cm}^{K^+}<1.0$
	47115	56246	103361	$1.30<MM(K^+)<1.45$

Table 3.1: The number of the survived events with the standard cuts for the $\vec{\gamma}$p→ K^+ $\Sigma(1385)/\Lambda(1405)$ events in LLH2 data sets with horizontally and vertically polarized photons.

The cut conditions of K^+ particle identification(PID)(black), decay in flight(DIF)(green), e^+e^- cut(blue), z-vertex(red) were imposed on for the survived K^+ events as shown in Fig. 3.1.

Tagger cut

The cut conditions of (ntag=1 or 2) and itagc.f>0 were imposed on for the LLH2 data sets. The number of tracks in a tagging counter(ntag) was survived with ≤ 2. The consistency between a hit position in SSD and a hit position in plastic scintillators of the tagger was checked, and this condition is necessary to select good tracks of the recoil electrons for the backward Compton scattering in the storage ring.

Particle identification cut

The mass of a charged particle(m) was calculated with the momentum(p), the path length(L) and the time-of-flight(TOF) as

$$m^2 = p^2\Big\{\Big(\frac{c \cdot TOF}{L}\Big)^2 - 1\Big\} = p^2 \cdot \Big(\frac{1}{\beta^2} - 1\Big), \tag{3.1}$$

$$\beta = \frac{v}{c} = \frac{p}{E} = \frac{p}{\sqrt{m^2+p^2}} = \frac{L}{TOF \cdot c}, \tag{3.2}$$

where c is the speed of light.

Fig 3.2 shows the charged particle identification(PID) in the two dimensional scatter plot of mass squared(mass^2) versus momentum with the pions, kaons and protons. The mass^2 resolution becomes worse as the momentum increases. The momentum dependence of the mass

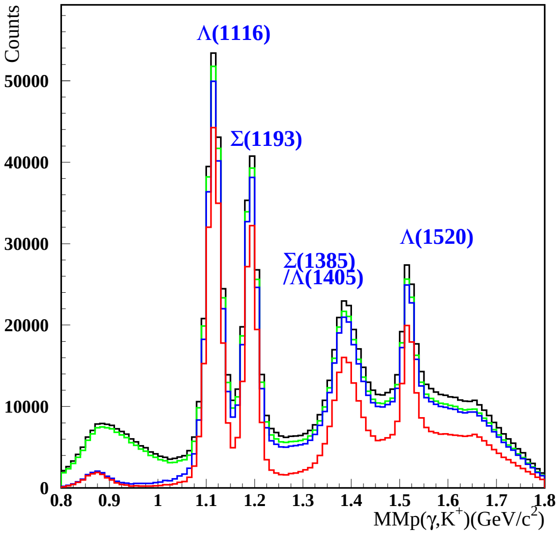

Figure 3.1: Missing mass spectra of K^+ with high statistics after applying the standard cuts listed in Table 3.1. The cut conditions of K^+ particle identification(PID)(black), decay in flight(DIF)(green), $\mathrm{e}^+\mathrm{e}^-$ cut(blue), z-vertex(red) are imposed on for survived K^+ events.

resolutions was considered to set the boundaries for the particle identification and obtained by perfoming a fitting with a polynomial function.

The boundary cut conditions of the momentum dependence are used for the K^+ particles identification. The K^+ particles were selected with 3σ mass cut and the red lines in Fig 3.2 indicate the boundary cut conditions for the K^+ particles. However, the boundaries between pions(protons) and kaons were set to 0.1762 GeV^2(0.55 GeV^2) at the higher momentum regions because of the worse mass resolution.

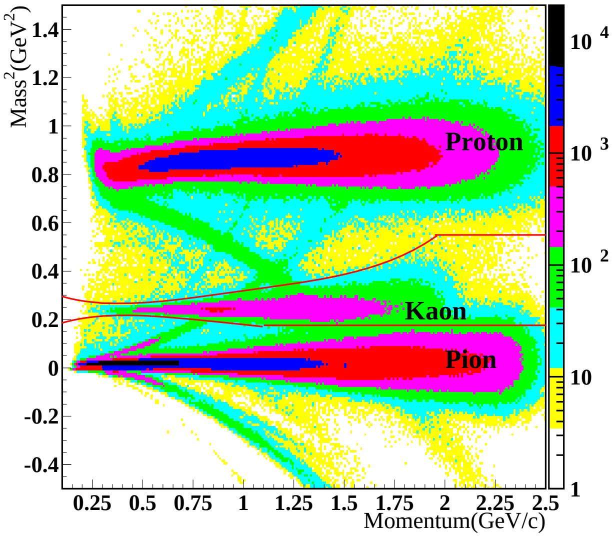

Figure 3.2: Charged particle identifications in the two dimensional scatter plot of squared mass(mass^2) versus momentum with pions, kaons and protons.

Decay in flight Cut

The events are rejected by decay-in-flight(DIF) cuts :

- χ^2 probability - The χ^2 probability was used to test a goodness of a fit and to reject bad tracks. The χ^2 probability of a track fitting is required larger than 0.02. The χ^2 probability with the number of degree of freedom *ndf* is defined as

$$prob(\chi^2, ndf) = \int_{\chi^2}^{\infty} f(\tilde{\chi}^2, ndf) d\tilde{\chi}^2. \qquad (3.3)$$

  The function $f(\chi^2, ndf)$ is the standard χ^2 distribution with the number of degree of freedom, *ndf*.

- Number of Outlier - If a hit of tracking chambers is deviated from the expected trajectories more than the resolution, the hit is judged as a background hit(outlier) and removed from the tracking. Decay-in-flight event has a track with the large number of outliers when it decays in the middle of the tracking volume (between SVTX and DC3). When the number of outliers are greater than 6, the tracks are rejected in the analysis.

- Consistency of TOF hit - It is required that a hit to the TOF counter corresponds to that of the prediction from the track. When the difference of y positions is greater than 80 mm or the difference of the TOF slat number is greater than 1, those tracks are rejected by this cut.

Fig. 3.3 shows the distributions of the χ^2 probability, the number of outliers and the difference of x and y positions between the reconstructed hit positions using the tracking system at the TOF counter and the measured positions by the TOF counter itself($id_{trk} - id_{tof}$ and $y_{trk} - y_{tof}$). The black histograms show the distribution of the K^+ skimmed events, and the red histograms show the distributions for the events survived after the decay-in-filight cuts.

e^+e^- Cut

The e^+e^- blocker, two lead bars, is used to remove e^+e^- events. The cut conditions(-30>ybar or ybar>16) were used to reject the e^+e^- events. Fig. 3.4 shows the distribution of Y-coordinate at e^+e^- bars. The black histrogram shows the survived events after K^+ PID and DIF cuts, and the red histrogram shows the survived events after K^+ PID, DIF and e^+e^- cuts. Therefore, the black and the red histograms indicate the distributions before and after the e^+e^- cut, respectively.

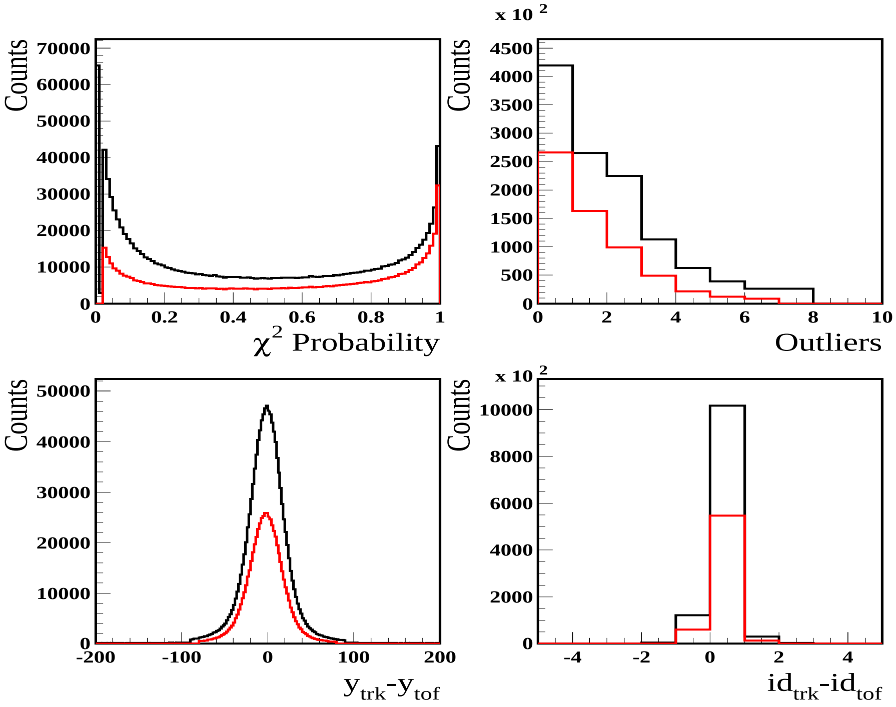

Figure 3.3: Distributions of decay-in-flight : the χ^2 probability, the number of outlier, $y_{trk} - y_{tof}$ and $id_{trk} - id_{tof}$. The black histograms show the distribution of the K^+ skimmed events, and the red histograms show the distributions for the events survived after the decay-in-filight cuts.

Z−vertex Cut

The single K^+ track events were used for the $\Sigma(1385)/\Lambda(1405)$ analysis. The single track events have the worse resolutions than the double track events because the photon beam spot at the target has σ_x=35 mm and σ_y=20 mm. Unfortunately, we do not know the correct vertex position between the photon beam and the single tracks. Therefore, the vertex point was defined as the closest distance between the track and the beam.

The z-vertex cut was applied to select events which come from the LH2 target region. Fig. 3.5 shows the distribution of z-vertex for the LLH2 data sets. The events were produced at the LH2 target region and the start counter region as shown in Fig. 3.5. Contamination events from the start counter existing in the target region can bias the physical results of differential cross sections and photon beam asymmetries. Therefore, the contamination events should be eliminated in the $\Sigma(1385)/\Lambda(1405)$ analysis. The more detailed analysis is shown in the Section 3.5. The z-vertex cut position to select the events produced at the LH2 target region was set to -1200 mm $<$ vtz $<$ -900 mm for the LLH2 data.

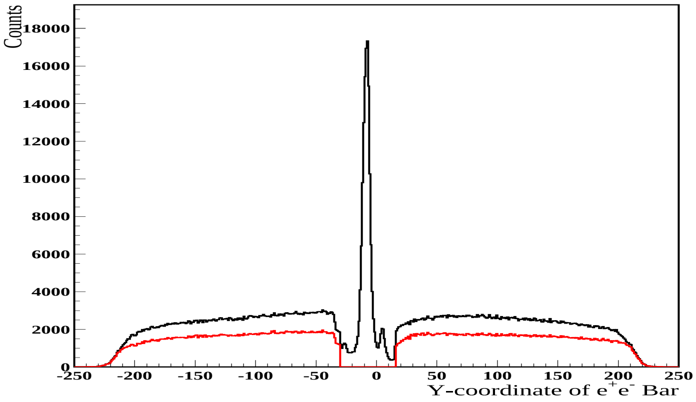

Figure 3.4: Distribution of Y-coordinate at e^+e^- bars. The black and the red histograms indicate the distributions before and after the e^+e^- cut, respectively.

Backgroud processes	Threshold Energy	E1	E2	E3	E4	E5	E6
$\vec{\gamma}p \longrightarrow K^+\pi^0\Lambda^0$(non-resonant)	1.15 GeV	O	O	O	O	O	O
$\vec{\gamma}p \longrightarrow K^{*+}\ \Lambda^0$	1.68 GeV		O	O	O	O	O
$\vec{\gamma}p \longrightarrow K^+\ \Lambda^*(1520)$	1.69 GeV		O	O	O	O	O
$\vec{\gamma}p \longrightarrow \phi p$	1.57 GeV	O	O	O	O	O	O
$\vec{\gamma}p \longrightarrow K^+\ \Lambda^*(1670)/\Lambda^*(1690)$	2.03 GeV				O	O	O

Table 3.2: Possible background processes under the $\Sigma(1385)/\Lambda(1405)$ signal region

3.3 K$^+$ missing mass distributions

Fig. 3.6 shows the K^+ missing mass distributions for the K^+ survived events in which standard cuts were applied to as listed in Table 3.1 at all the photon energy region(a) and 6 different photon energy regions(b). The missing mass distributions are different in each photon energy region. To select the $\Sigma(1385)/\Lambda(1405)$ events, the yields of $\Sigma(1385)/\Lambda(1405)$ events were obtained by the template fitting method with the consideration of possible background processes. There are many background processes under the $\Sigma(1385)/\Lambda(1405)$ mass region. The possible background processes possibly occur under the $\Sigma^*(1385)/\Lambda^*(1405)$ signal region are listed in Table 3.2. Each backgroud proesse has a different threhsold energy, so the possible background events under the signal region should be estimated at the classified the photon energy region. The possible background processes are checked with O in each photon energy region as shown in Table 3.2.

As shown in Table. 3.3, the photon energies were divided with the 150 MeV bin width from 1.5 GeV to 2.4 GeV. In the analysis of differential cross sections, the polar angles were divivded with 0.1 rad bin width in the region of $0.6<\cos\theta_{cm}^{K^+}<0.9$ and 0.05 rad bin width in the region of $0.9<\cos\theta_{cm}^{K^+}<1.0$. In the analysis of photon bem asymmetry, the polar angles were divivded with 2 bins with $0.6<\cos\theta_{cm}^{K^+}<0.9$ and $0.9<\cos\theta_{cm}^{K^+}<1.0$ because the missing mass distribution

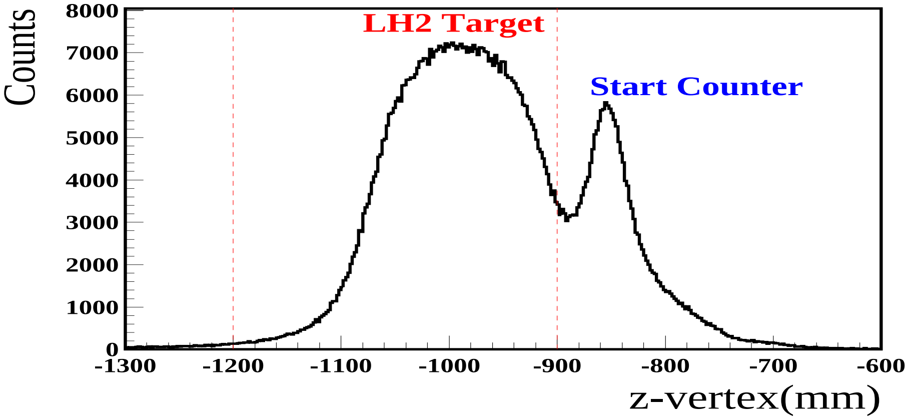

Figure 3.5: Distribution of z-vertex with a single track. The z-vertex cut position of -1200 mm$<$ z-vertex $<$ -900 mm cut is imposed on for long liqud hydrogen(LLH2) data.

should be get in each azimuthal angle bin. The azimuthal angle bin was divided with 12 bins from 0° to 360°.

3.4 Kinematical regions of $\Sigma(1385)/\Lambda(1405)$ hypreons

Fig. 3.7 shows kinematical regions for the $\Sigma(1385)/\Lambda(1405)$ hyperons and represents scatter plots as follow :
(a) is a scatter plot of missing mass of K^+ versus K^+ momentum,
(b) is a scatter plot of cos$\theta^{K^+}_{cm}$ versus momentum transfer($\tilde{t}$),
(c) is a scatter plot of the $cos\theta^{K^+}_{cm}$ versus K^+ azimuthal angle ϕ_{K^+}
(d) is a scatter plot of photon energy(E_γ) versus momentum transfer($\tilde{t}$).

The $\Sigma(1385)/\Lambda(1405)$ events were detected with 2π coverage for cos$\theta^{K^+}_{cm}$ >0.8 beacuse the acceptance of a LEPS spectrometer in the y-direction is smaller than that in the x-direction. The (b)∼(d) in Fig 3.7 shows the distributions for the $\Sigma(1385)/\Lambda(1405)$ events corresponding to 1.30<MM(K^+)<1.45 regions.

The $\tilde{t}$ is defined as t+|t|$_{min}$ where t is defined as a square of 4-momentum transfer from incident photons to K^+ outgoing particles and |t|$_{min}$ is defined as minimum momentum transfer for the production of $\Sigma(1385)/\Lambda(1405)$ out of a proton target at a polar angle(θ) of zero degree. The momentum transfer, $\tilde{t}$(=t+|t|$_{min}$) intervals were divided by 0.02 GeV^2 in $-0.1<\tilde{t}<0$, 0.05 GeV^2 in $-0.2<\tilde{t}<-0.1$ and 0.1 GeV^2 in $-0.6<\tilde{t}<-0.2$ for the analysis of the differential cross sections, as shown in Table 3.3.

Fig 3.8 shows the ditributions of the momentum transfer($\tilde{t}$) in 6 photon energy regions corresponding to the 1.30<MM(K^+)<1.45 regions.

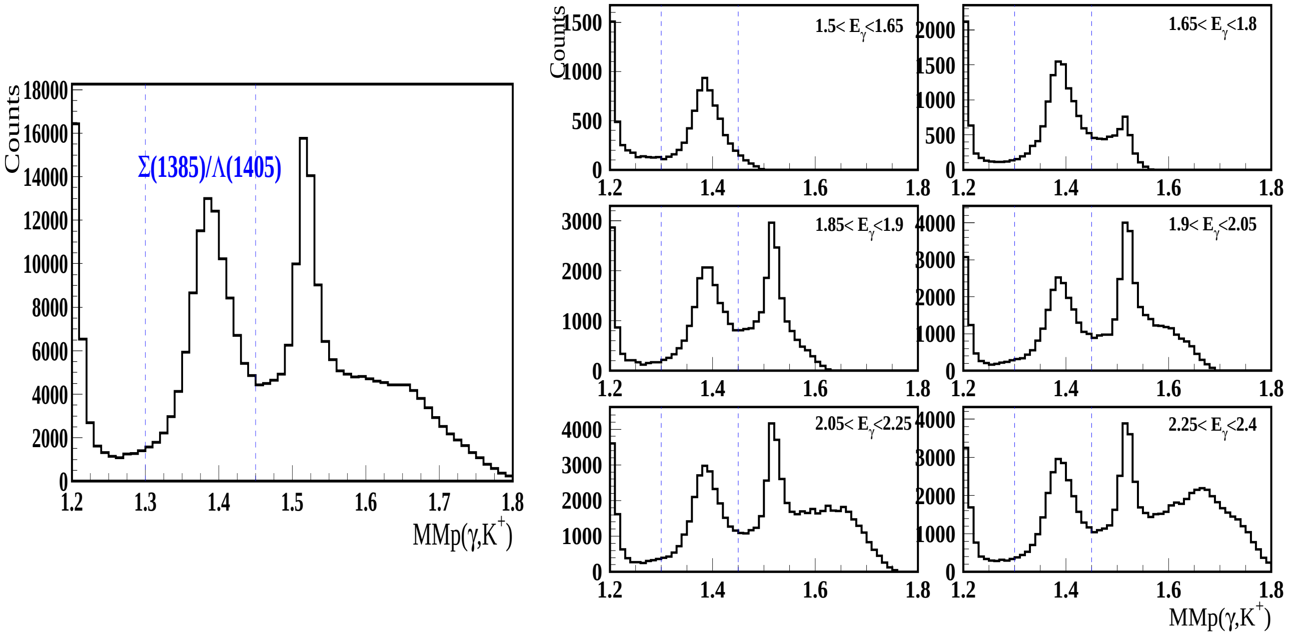

(a) (b)

Figure 3.6: Missing mass distributions for the K^+ survived events with all the photon energy region(a) and 6 different photon energy regions(b)

3.5 Contaminations in the $\Sigma(1385)/\Lambda(1405)$ signal region

The contaminations were considered as follow :

(1) tagging counter system

(2) start counter

(3) $2ns$ π^+/p events

since they can influence the yield estimation for $\Sigma(1385)/\Lambda(1405)$ events.

3.5.1 Background events at a tagging system

The photon energy was used to calculate the missing mass of the p(γ,K$^+$)X reactions. The tagger cut was used to select the good track of the recoil electron by the backward Compton scattering process in the tagging system. Because shielding materials were placed at the high electron-energy side of the tagging system corresponding to the low photon-energy side as shown in Fig. 2.11, so there are low energy photons of the shower events produced at shielding materials for the tagger counter. Some of these shower events are reconstructured and can have a wrong photon energy. Therefore, these events can appear under the signal region. These background events were rejected using follwing conditions :

$$npl(1) = 0 \text{ or } npl(2) = 0, \tag{3.4}$$

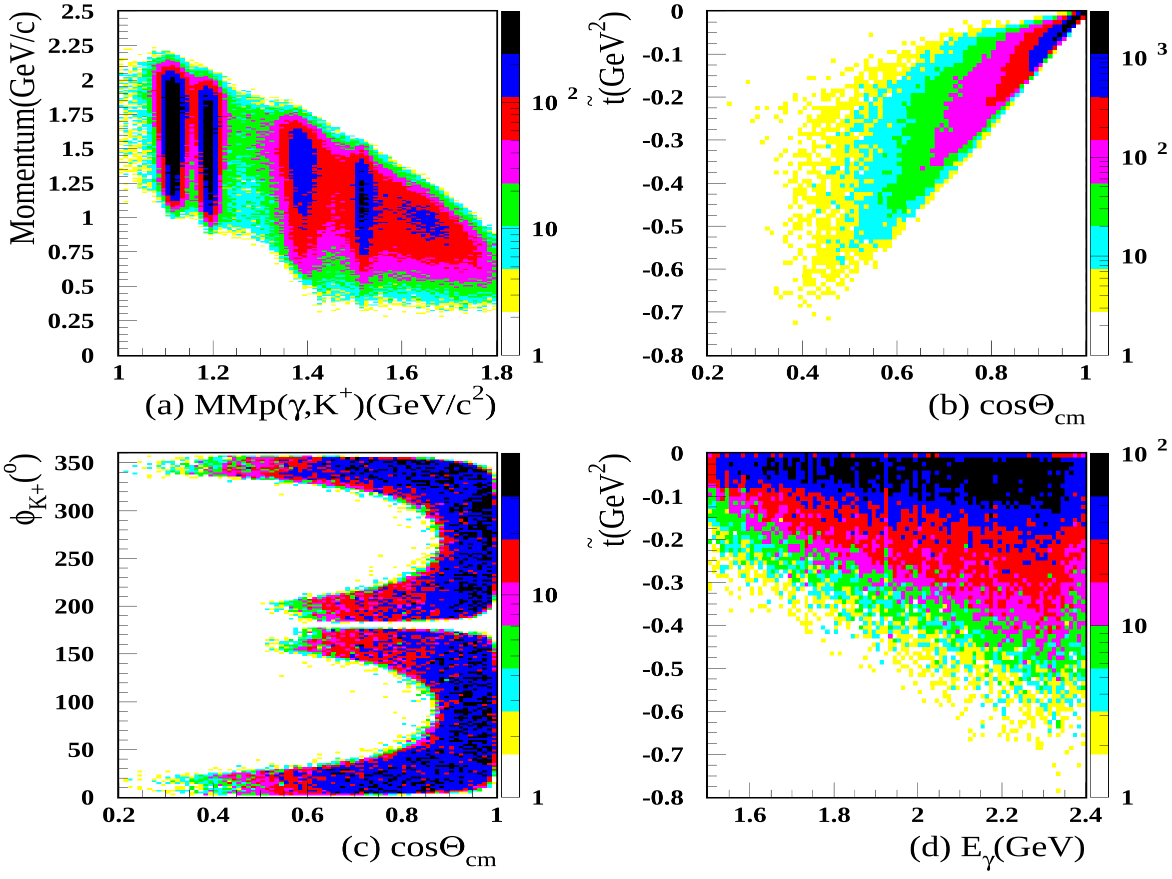

Figure 3.7: Kinematical regions of Σ(1385)/Λ(1405) events : scatter plots of (a) is missing mass of K$^+$ versus K$^+$ momentum, (b) is cos$\theta_{cm}^{K^+}$ versus momentum transfer($\tilde{t}$), (c) $cos\theta_{cm}^{K^+}$ versus K$^+$ azimuthal angle ϕ_{K^+} and (d) photon energy(E$_\gamma$) versus momentum transfer($\tilde{t}$)

where npl(1) and npl(2) are the number of hits which are not associated with any recoil electron, in the plastic scintillator hodoscope 1 and 2, respectively. This condition selects events for the hits by only recoil electrons at least in one of two hodoscopes.

In this analysis, the cut condition was required to get clean Σ(1385)/Λ(1405) events as follows ;

$$npl(1) = 0 \text{ and } npl(2) = 0 \tag{3.5}$$

There are two narrow energy regions, up to 2.4 GeV, where this condition cannot be used because of the presence of a few dead strips in the SSD layers. We assumed that there is no hit in these dead strips to preserve tracks passing through these areas. A special treatment was made for these events in the tagging analysis. Therefore, the full condition of the tagger

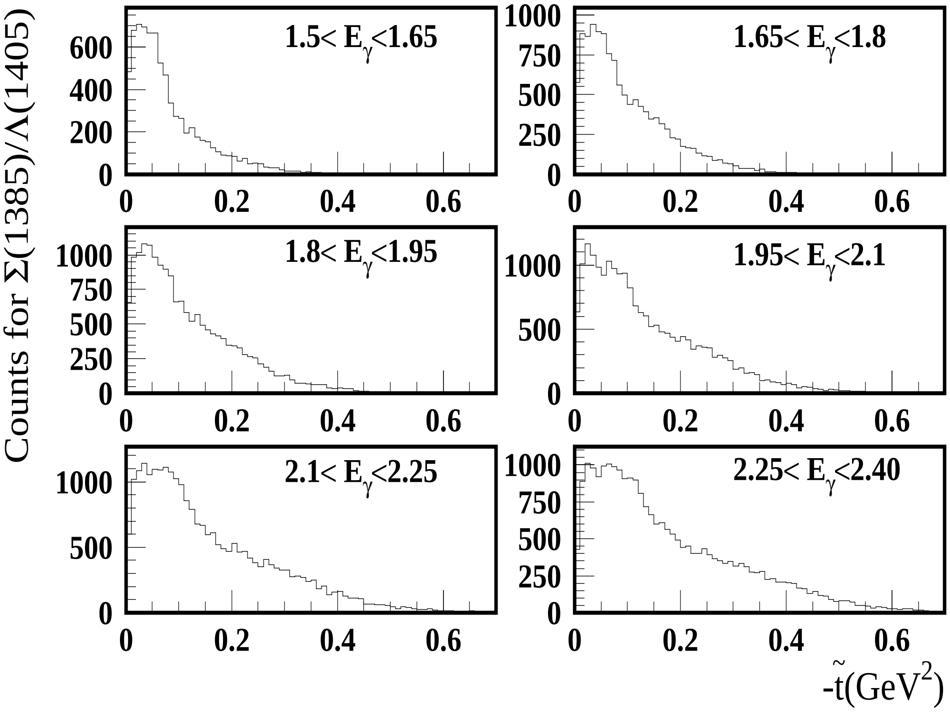

Figure 3.8: Distribution of momentum transfer($\tilde{t}$) in 6 different photon energy regions for the $\Sigma(1385)/\Lambda(1405)$ events

cut to select a good recoil electron is

$$(\text{npl}(1) = 0 \ \text{ or } \ \text{npl}(2) = 0) \text{ or } (1.91 < E_\gamma < 1.93 \ \text{ or } \ 2.27 < E_\gamma < 2.30). \tag{3.6}$$

In this analysis, we used new(tight) tagger cut conditions to get clean events as Eq. 3.7.

$$(\text{npl}(1) = 0 \ \text{ and } \ \text{npl}(2) = 0) \text{ or } (1.91 < E_\gamma < 1.93 \ \text{ or } \ 2.27 < E_\gamma < 2.30). \tag{3.7}$$

These conditions select the events for the hits by only recoil electrons at both of two hodoscopes.

3.5.2 Contaminations from the start counter

The horizontally polarized photons and the vertically polarized photons have different z-vertex distributions due to the different beam profiles. The vertex resolution for the horizontally polarized photons is worse than that for the vertically polarized photons. Therefore, the contamination rate of the start counter events was estimated separately.

The contamination from the start counter is vaies depending on polarization, polar angle and photon energy. The z-vertex distribution is neither the Gaussian shape nor symmetric especially at the forward angles. The Monte Carlo simulation (g3leps) including information on the beam profile was used to estimate the contamination rate of the $\Sigma(1385)/\Lambda(1405)$

events produced at the start counter. The MC spectra shape of the z-vertex distributions were fitted to the data. The Fig. 3.9 shows contamination from the start counter in the LLH2 target region which indicates the green vertical lines. The left figures are for the horizontally polarized photon beam and the right figures are for the vertically polarized photon beam. The figures from top to bottom are for the 0.95<cos$\Theta_{cm}^{K^+}$ <1.00(C1=very forward angle regions), the 0.90<cos$\Theta_{cm}^{K^+}$ <0.95(C2), the 0.80<cos$\Theta_{cm}^{K^+}$ <0.90(C3), the 0.70<cos$\Theta_{cm}^{K^+}$ <0.80(C4) and the 0.60<cos$\Theta_{cm}^{K^+}$ <0.70(C5), respectively. The 6 different figures in each polar angle region indicate the different photon energy region. The figures from the upper-left corner to the bottom right corner represent the lower photon energy region to the higher photon energy region. The filled green colors indicate the contaminated events in the target region from the start counter as shown in Fig. 3.9.

The contamination rate from the start counter as a function of E_γ at the different $cos\Theta_{cm}^{K^+}$ angle regions are shown in Fig. 3.10. The upper figure is for the horizontally polarized photons cases and the bottom figure is for the vertically polarized photons cases. The contamination rate from the start counter was found to be large at the very forward angle regions. Each color indicates the divided $cos\Theta_{cm}^{K^+}$ bin as follows: 0.95<cos$\Theta_{cm}^{K^+}$ <1.0(black), 0.90<cos$\Theta_{cm}^{K^+}$ <0.95(red), 0.80<cos$\Theta_{cm}^{K^+}$ <0.90(green), 0.70<cos$\Theta_{cm}^{K^+}$ <0.80(blue) and 0.60<cos$\Theta_{cm}^{K^+}$ <0.70(pink).

We found that the contamination ratio of the horizontally polarized photon cases is larger than the vertically polarized photon cases. The contamination rate at the lower photon energy regions is larger than at the higher photon energy regions. The contamination rate is in the range of 0.5∼13% at the lower photon energy region and 0∼4% at the higher photon energy region in terms of cos$\Theta_{cm}^{K^+}$. Moreover, the contamination rate at the very forward angle is larger than the large scattering angle case.

As a result of the contamination ratio, the shape of missing mass spectra is important in the yield estimation of $\Sigma(1385)/\Lambda(1405)$ at the very forward angle/lower photon energy region, while there are negligiblely small contamination ratio at the higer photon energy region.

As the same method, the contamination ratio were also estimated as $\tilde{t}$ bins and the results are shown in Fig. 3.11.

3.5.3 π^+/p contamination

The circulating electrons were bunched at every 1.966 ns in the storage ring. The arrival time of a BCS photon at the target was synchronized with the RF signal. The 2 ns bunch structures are seen in the 2−dimensional scatter plot of momentum and mass squared(mass^2). The 2 ns events of π^+ and proton events in the K^+ band region should be eliminated. However, the statistics of 2 ns π^+/p events is low, so it is difficult to estimate the contamination ratio and their missing mass spectra.

Therefore, the following procedure were done to eliminate 2 ns π^+/p events with high statistics :
(1) The real π^+(proton) events were shifted with $+(-)2$ ns(green).
(2) The K^+ identified(red) events in the K^+ band region(blue) are estimated as shown in the Fig. 3.12.

The Fig. 3.12 is the 2−dimensional scatter plot of momentum and mass squared(mass^2) for +2 ns events of π^+ and the Fig. 3.13 is the 2−dimensional scatter plot of momentum and

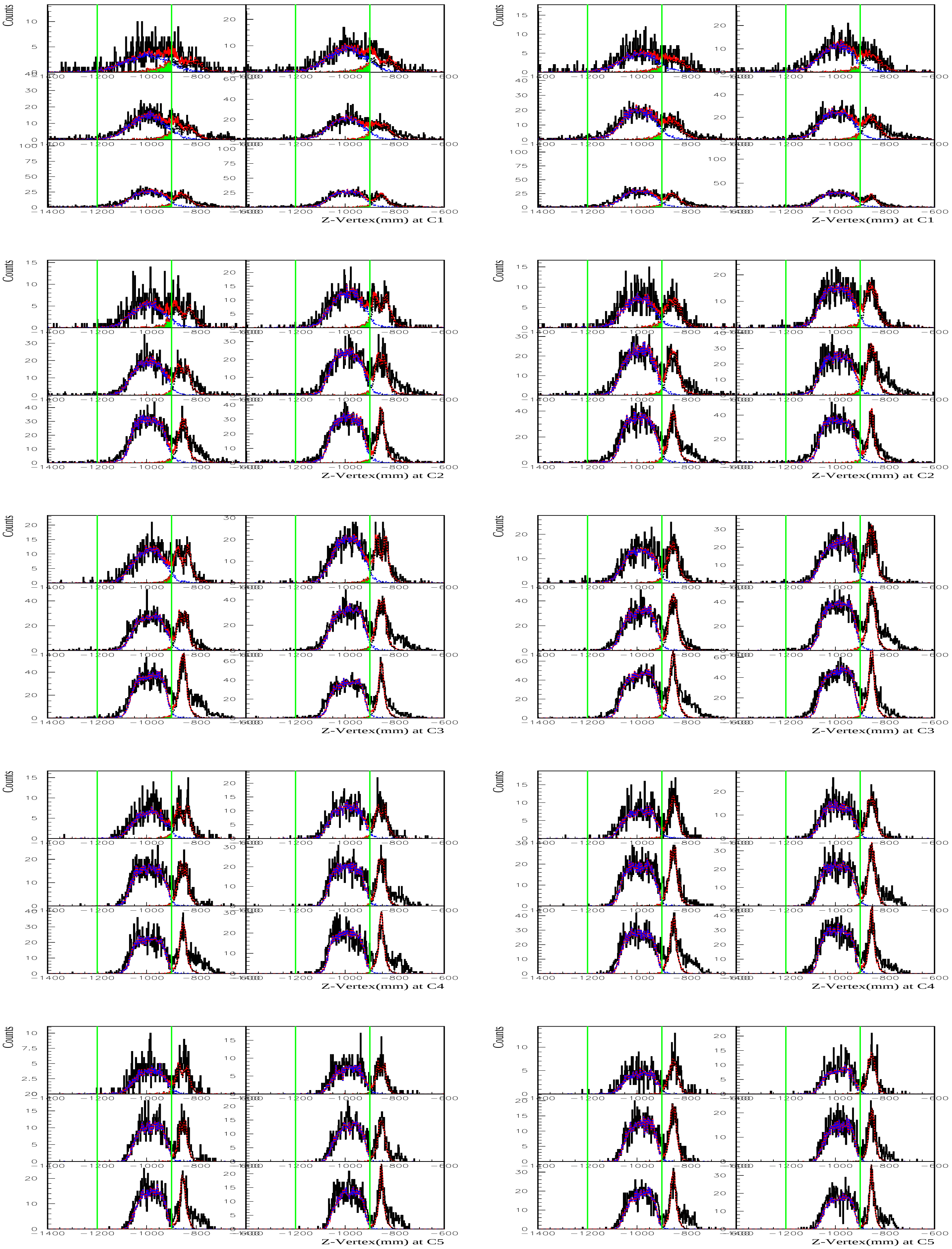

Figure 3.9: Contamination from the start counter to the target region as the beam polarization, polar angle and the photon energy: Left and right figures are for the horizontally and the vertically polarized photon beam, respectively. The figures from top to bottom indicate the from C1 to C5 bin.

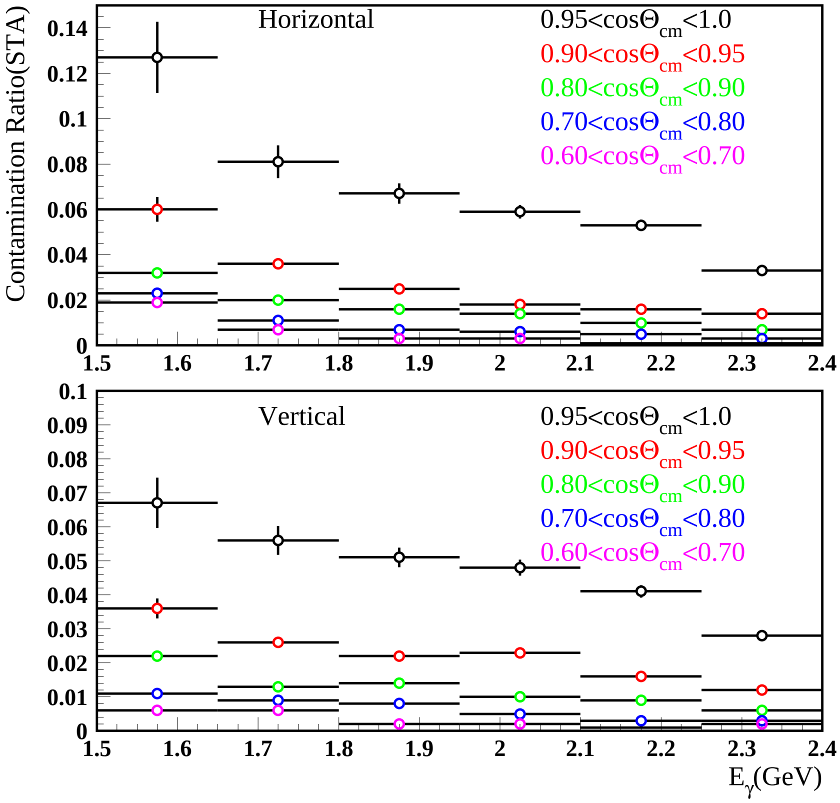

Figure 3.10: Contamintaion rate from the start counter as a function of E_γ at different $cos\Theta_{cm}^{K^+}$ regions: The $cos\Theta_{cm}^{K^+}$ are divided into $0.95<\cos\Theta_{cm}^{K^+}<1.0$(black), $0.90<\cos\Theta_{cm}^{K^+}<0.95$(red), $0.80<\cos\Theta_{cm}^{K^+}<0.90$(green), $0.70<\cos\Theta_{cm}^{K^+}<0.80$(blue) and $0.60<\cos\Theta_{cm}^{K^+}<0.70$(pink). And the contamination ratio of the horizontally polarized photon cases is larger than the vertically polarized photon cases.

mass squared(mass^2) for -2 ns events of proton. Then,
(3) The probability of the shifted 2 ns events from real π^+(proton) using the mass squared(mass^2) distribution can be separated well between 2 ns events and real K^+ events at the low momentum region. These corrections can estimate 2 ns events of π^+ and proton events in each K^+ missing mass region.

As shown in Fig. 3.14 and Fig. 3.15, the blue-dashed lines show the missing mass distribution of the 2 ns π^+/p events and the green-dashed lines show the missing mass distribution of the rejected background events from the start counter. The black-solid lines show the sum of the missing mass distributions for both $2ns$ π^+/p events and the start counter contaminations. The missing mass distributions were obtained in 6 photon energy regions divided into 5 different $\cos\Theta_{cm}^{K^+}$ regions. The Fig. 3.14 is for the horizontally polarized photon case and Fig. 3.14 is for the vertically polarized photon case. The red-dashed lines indicate the $1.30<MM(K^+)<1.50$

GeV/c^2 signal region for the $\Sigma(1385)/\Lambda(1405)$. It can be explained that about the half of them events are in the unphyisical missing mass region (between the tail of $\Sigma(1193)$ and 1.23 GeV/c^2) at the lower photon energy regions. These contaminations were subtracted and the contamination rate is a few % in the $\Sigma(1385)/\Lambda(1405)$ signal regions.

3.6 Fitting to missing mass distributions

The yields of $\Sigma(1385)/\Lambda(1405)$ were obtained by a template fitting using missing mass spectra of background events by MC simulation. The template fitting was done with a log-likelihood fit .

$$\chi^2 = \sum_{j=1}^{n} \frac{(f_{data} - \sum_{i=1}^{5} N_j f_{MC,i})^2}{\sigma_j^2}, \tag{3.8}$$

where i represents the number of each reaction for the MC simulation,
j represents each bin of the missing mass spectra,
N_j is the number of events at j^{th} bin in the missing mass spectra.
σ_j represents the statistical error.
f_{data} is spectra of real data,
f_{MC} is spectra of MC which can be expressed as f_{MC}=$a_1 f_1(x_1)$+$a_2 f_2(x_2)$+$a_3 f_3(x_3)$+..
(a_1=a_2.... represents a yield coefficient for each processes.
f_1=f_2... represents the MC spectra of each processes with high statistics).

The MINUIT package was used to obtain yield parameters for signals and backgrounds by minimizing χ^2 of Eq. 3.8.

The missing mass spectra of $\Sigma(1385)/\Lambda(1405)$ obtained by using MC spectra after template fitting to the data are indicated with red dashed line as shown in Fig. 3.16. The production ratio of $\Lambda(1405)$ to $\Sigma(1385)$ which was obtained by TPC experiments [20] was used in the summed $\Sigma(1385)/\Lambda(1405)$ MC spectra. As shown in Fig. 3.16, the missing mass spectra of contamination which comes from the start counter, 2 *ns* of π^+/p events(hatched histograms) are included, and the background events from the tagging counter are already removed in the missing mass spectra of real data. The number of yields of the background events with non-resonant $K^+\pi^0$ Λ^0(black), K^{*+} Λ^0(green), K^+ $\Lambda(1520)$(blue), ϕp(pink) and $K^+\Lambda(1670)/\Lambda(1690)$(light blue) were obtained, and the red-solid lines indicate the summed spectra of $\Sigma(1385)/\Lambda(1405)$ signal events and the possible background events by MC template fitting.

The yields of $\Lambda(1405)$ and $\Sigma(1385)$ were obtained with different fitting methods. The Method I means the template fitting done using $K^+\pi^0$ Λ^0 and K^{*+} Λ^0, respectively. The Method II means the azimuthal angle distributions of $K^+\pi^0\Lambda^0$ and K^{*+} Λ^0 following the azimuthal angle distributions of MC results. The Method II considers the fluctuations between signal and two $K^+\pi^0\Lambda^0$ and K^{*+} Λ^0 backgrounds under the $\Sigma(1385)$ and $\Lambda(1405)$ signal region because their spectra get resembled as the photon energy becomes lower. The missing mass spectra of MC at each azimuthal angle bin have been multiplied by the same scale factor for $K^+\pi^0$ Λ^0 and K^{*+} Λ^0, respectively. The scale factor was obtained with high statistics at each photon energy region. We obtained the sum of the missing mass spectra of $K^+\pi^0$ Λ^0 and K^{*+}

Λ^0. The shapes of the summed missing mass spectra were used to get the $\Sigma(1385)/\Lambda(1405)$ yields as a free parameter.

Fig. 3.17 shows the different template fitting method, (a) Method I, (b) Method II and (c) Method I with the assumption of the straight-line backgrounds.

3.7 GEANT simulation

The acceptance of the LEPS spectrometer($A_{spectrometer}$) was obtained by Geant3 Monte Carlo(MC) simulation(g3leps). The input parameters for g3leps MC simulation are listed in Appendix B.1.

3.7.1 Smearing of DC resolution and E$_\gamma$ resolution

The smearing for incident photon energy and DC resolution was done for 12.2 MeV and 15%, respectively. Fig. 3.18 shows the mean and sigma of $\Lambda(1116)$ and $\Sigma(1193)$. The red circles are for real data, the black circles are for MC before smearing. The blue circles are for MC after smearing. We found that the mean and sigma are consistent well after smearing of DC resolution and E$_\gamma$ resolution.

3.7.2 Acceptance for the $\vec{\gamma}p \to K^+\Sigma(1385)/\Lambda(1405)$ reactions

The acceptance of the $\Sigma(1385)/\Lambda(1405)$ in the LEPS spectrometer was obtained with the ratio of $\Lambda(1405)$:$\Sigma(1385)$=1:1 using Breit-Wigner formula. The mass and width are used with 1383.7MeV/c^2 and 36 MeV/c^2 and 1406.5 MeV/c^2 and 50 MeV/c^2 for $\Sigma(1385)$ and $\Lambda(1405)$, respectively. Fig. 3.19 shows the acceptance for the p($\vec{\gamma}$,K^+)$\Sigma(1385)/\Lambda(1405)$ as a function of momentum transfer with 6 photon energy bins. The black circles denotes the acceptance for the horizontally polarized photons and the red circles are the acceptance for the vertically polarized photons. It was found that the acceptance is almost same for both cases. Therefore, we can use the averaged acceptance of both cases as shown in Fig. 3.20.

	E_γ range[GeV]
E1	1.50−1.65
E2	1.65−1.80
E3	1.80−1.95
E4	1.95−2.10
E5	2.10−2.25
E6	2.25−2.40

	(for differential cross sections) $\cos\Theta_{cm}^{K+}$ range[rad]		(for photon beam asymmetry) $\cos\Theta_{cm}^{K+}$ range[rad]
C1	0.95−1.00	CA1	0.90-1.00
C2	0.90−0.95	CA2	0.60-0.90
C3	0.80−0.90		
C4	0.70−0.80		
C5	0.60−0.70		

	ϕ_{K^+} range (°)		ϕ_{K^+} range (°)
$\phi1$	0-30	$\phi7$	180-210
$\phi2$	30-60	$\phi8$	210-240
$\phi3$	60-90	$\phi9$	240-270
$\phi4$	90-120	$\phi10$	270-300
$\phi5$	120-150	$\phi11$	300-330
$\phi6$	150-180	$\phi12$	330-360

	$\tilde{t}$ bins[GeV^2]
T1	$-0.02 < \tilde{t} < 0.$
T2	$-0.04 < \tilde{t} < -0.02$
T3	$-0.06 < \tilde{t} < -0.04$
T4	$-0.08 < \tilde{t} < -0.06$
T5	$-0.10 < \tilde{t} < -0.08$
T6	$-0.15 < \tilde{t} < -0.10$
T7	$-0.20 < \tilde{t} < -0.15$
T8	$-0.30 < \tilde{t} < -0.20$
T9	$-0.40 < \tilde{t} < -0.30$
T10	$-0.50 < \tilde{t} < -0.40$
T11	$-0.60 < \tilde{t} < -0.50$

Table 3.3: Definition of the E_γ, $\cos\theta_{cm}^{K^+}$, ϕ_{K^+} and $\tilde{t}$ bins

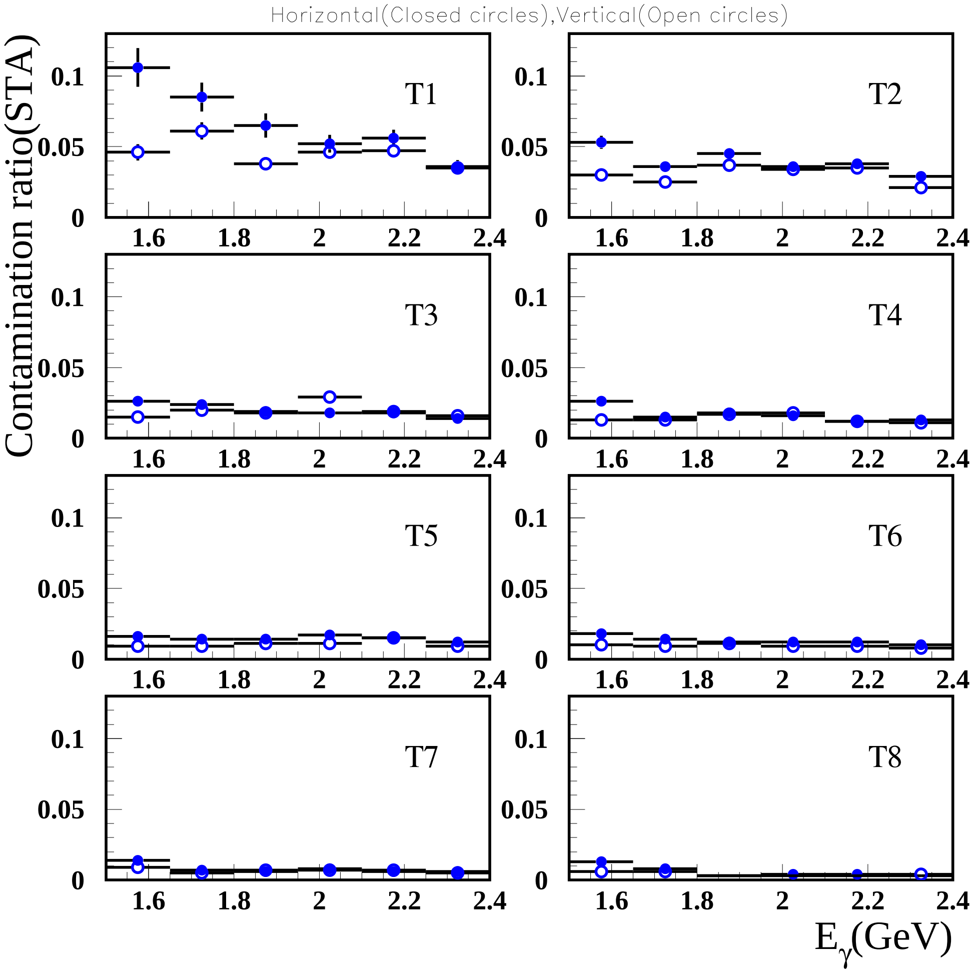

Figure 3.11: Contamintaion rate from the start counter as a function of E_γ at different $\tilde{t}$ regions(from T1 to T8 bins). The closed and the open circles indicate the horizontally and the vertically polarized photon beam cases, repectively

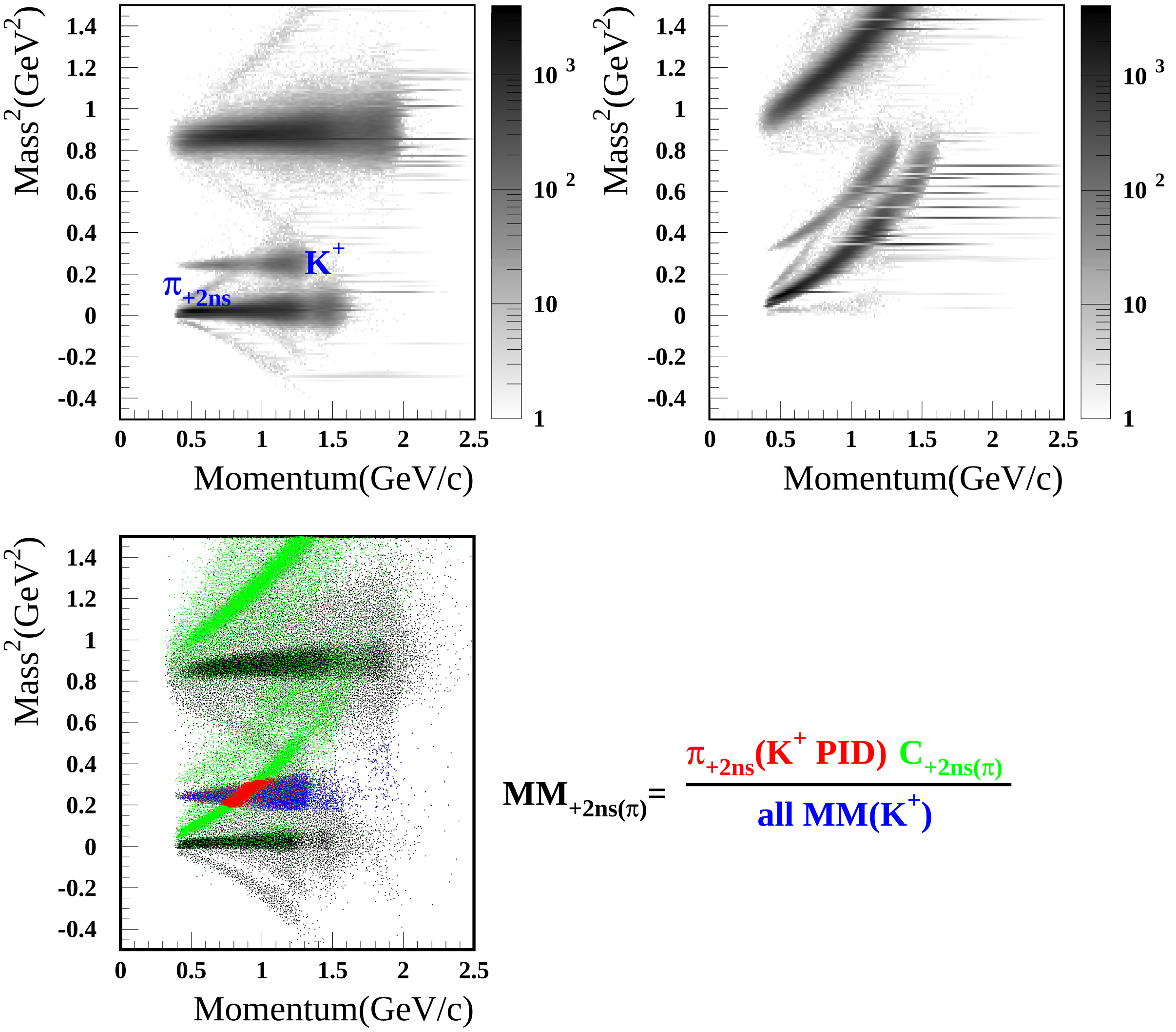

$$MM_{+2ns(\pi)} = \frac{\pi_{+2ns}(K^+\ \mathrm{PID})\ C_{+2ns(\pi)}}{\mathrm{all}\ MM(K^+)}$$

Figure 3.12: '+2 ns events' in the K^+ region from π^+ events

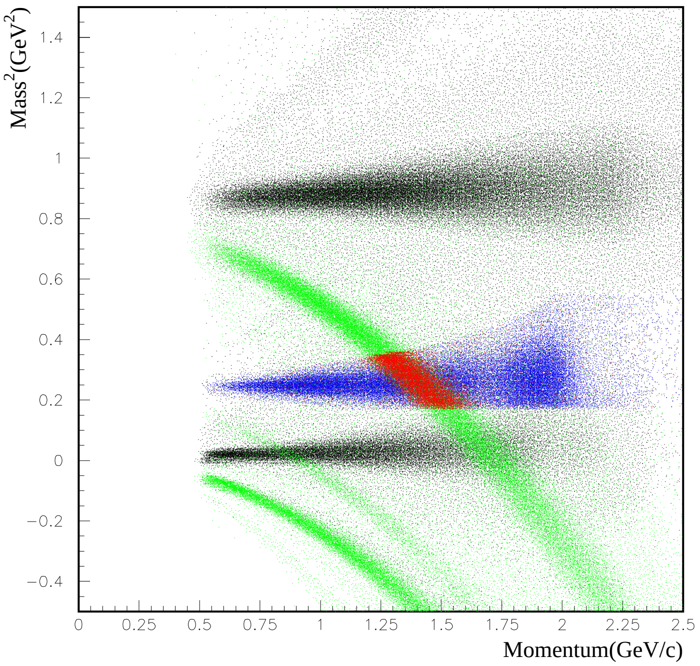

Figure 3.13: '-2 ns events' in the K^+ region from proton events

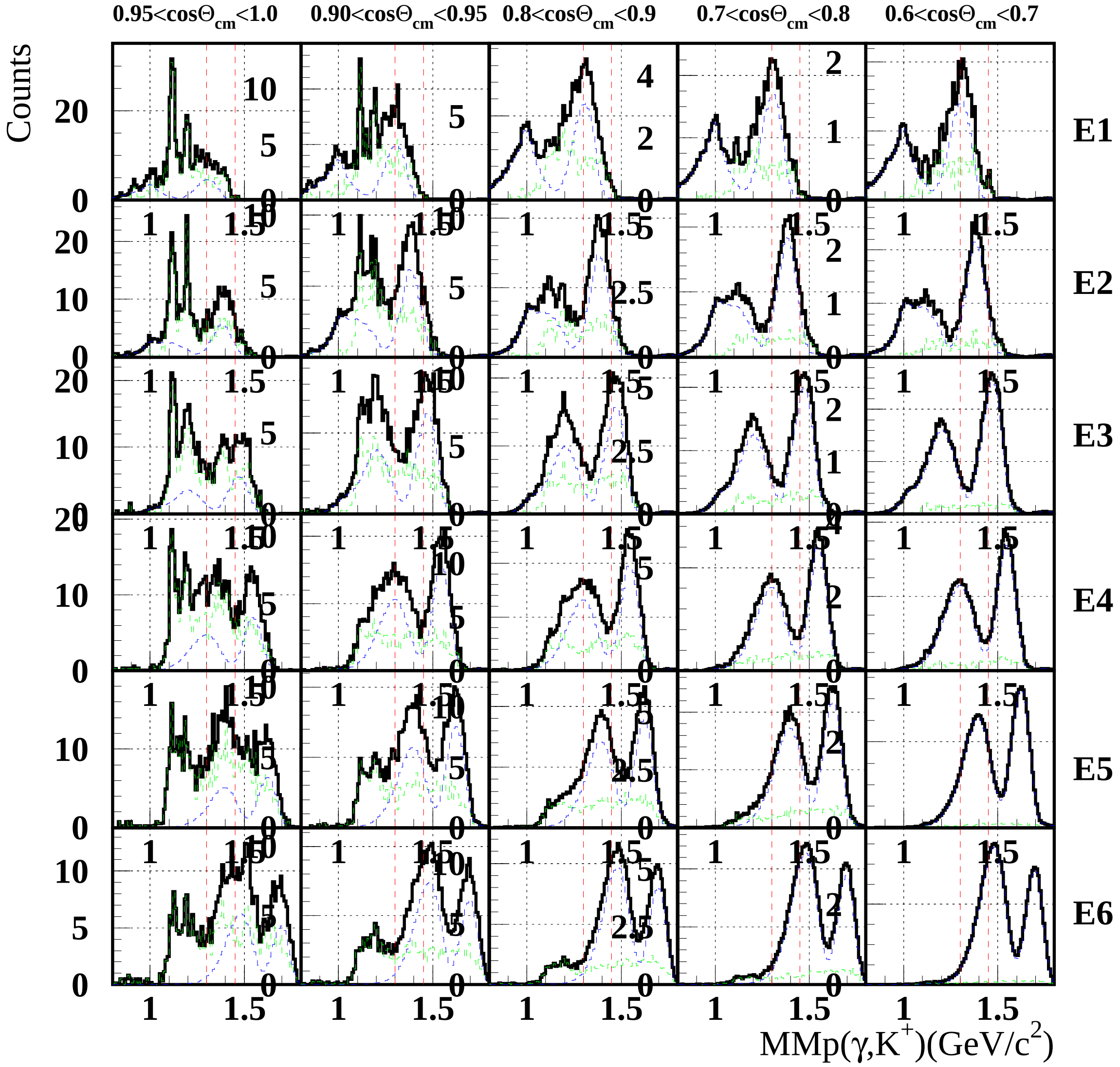

Figure 3.14: The blue-dashed lines show the missing mass distribution of the rejected 2 ns π^+/p events and the green-dashed lines show the missing mass distribution of the rejected background events from the start counter. The black-solid lines show the sum of the missing mass distributions for both $2ns$ π^+/p events and the start counter contamination. The missing mass distributions were obtained in 6 photon energy regions divided into 5 different $\cos\theta^{K^+}_{cm}$ regions. (Horizontally polarized photons)

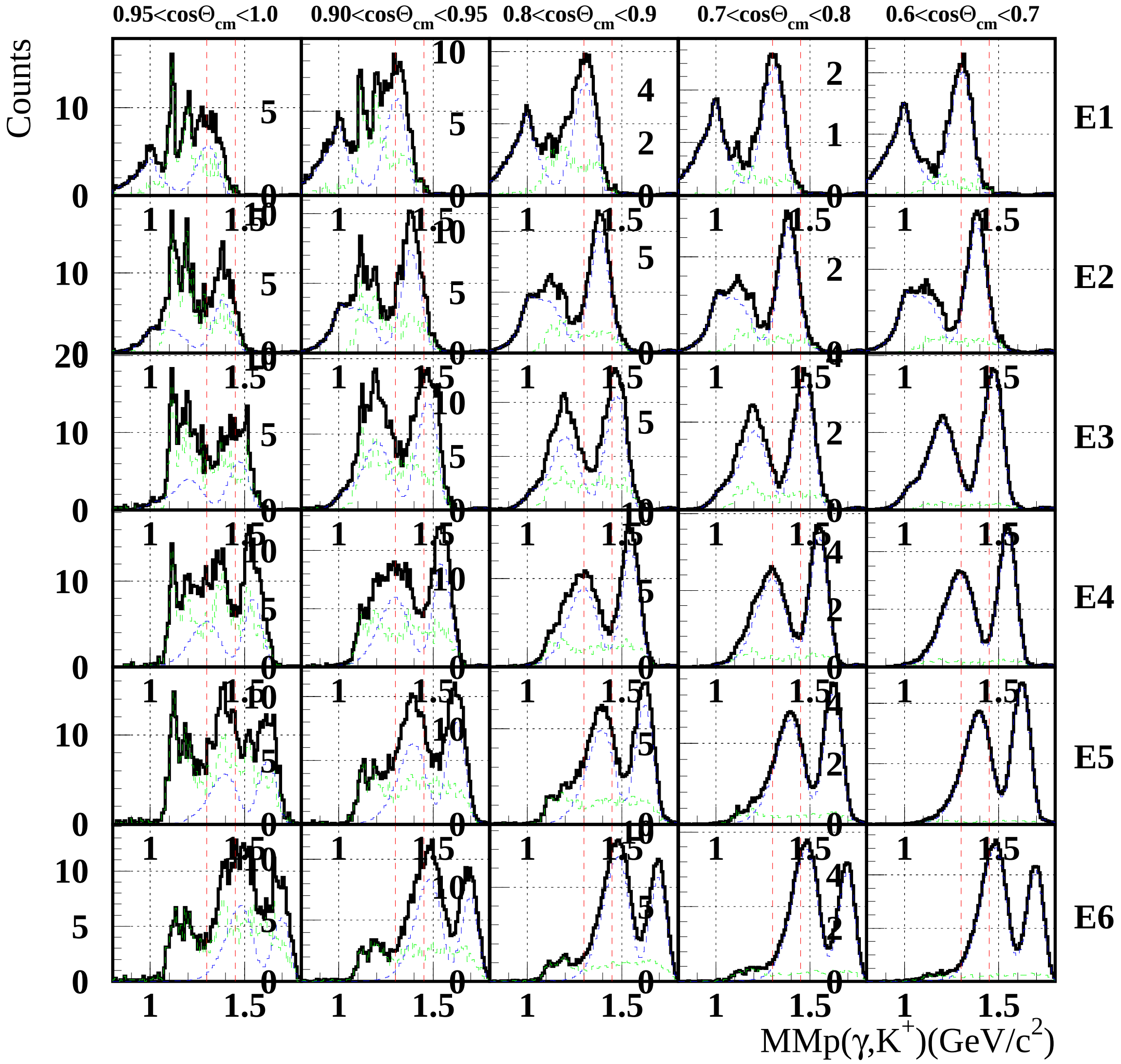

Figure 3.15: The blue-dashed lines show the missing mass distribution of the rejected 2 ns π^+/p events and the green-dashed lines show the missing mass distribution of the rejected background events from the start counter. The black-solid lines show the sum of the missing mass distributions for both $2ns$ π^+/p events and the start counter contamination. The missing mass distributions were obtained in 6 photon energy regions divided into 5 different cos$\theta_{cm}^{K^+}$ regions. (Vertically polarized photons)

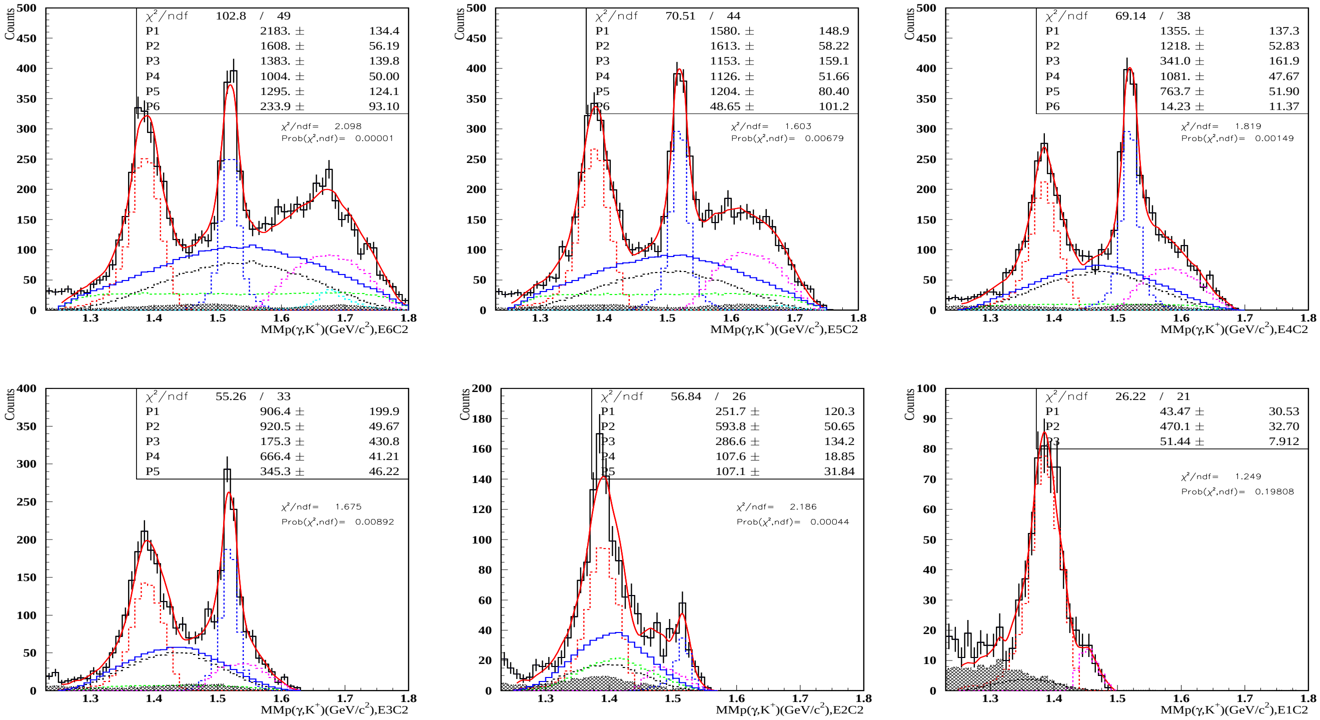

Figure 3.16: Template fitting for $\Sigma(1385)/\Lambda(1405)$

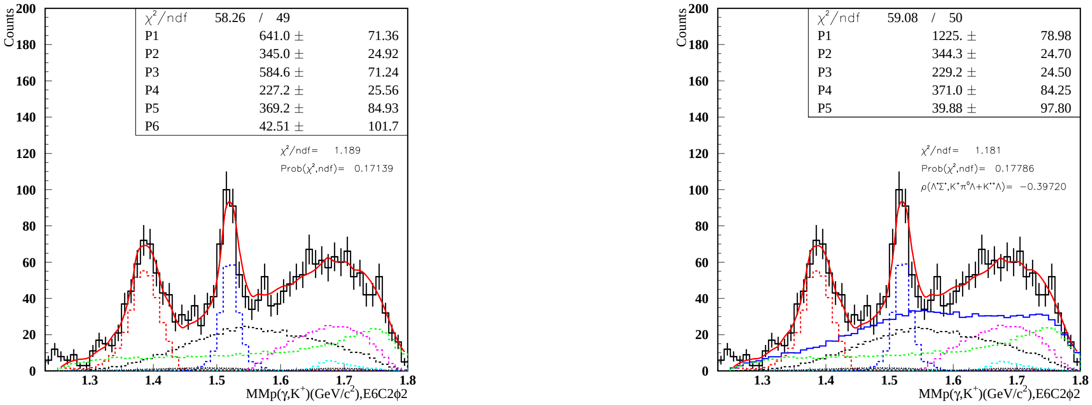

(a) (b)

Figure 3.17: Different template fitting method : (a) Method I (b) Method II

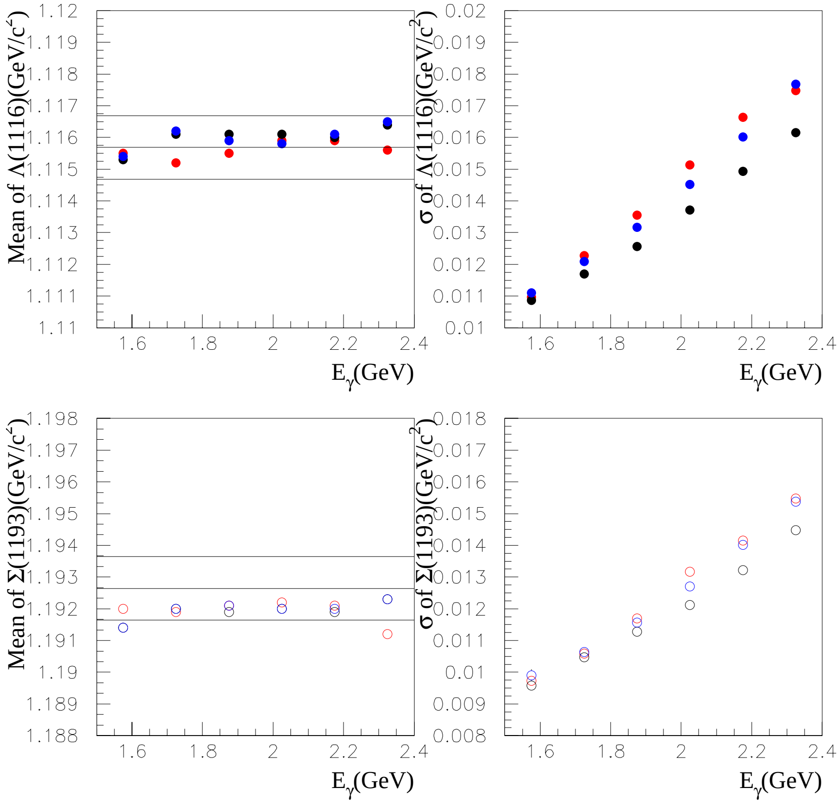

Figure 3.18: Missing mass resolution by smearing of DC and $E\gamma$ resoultions. The red circles are the mean and sigma values for real data, the black circles are for MC before smearing and the blue circles are for MC after smearing.

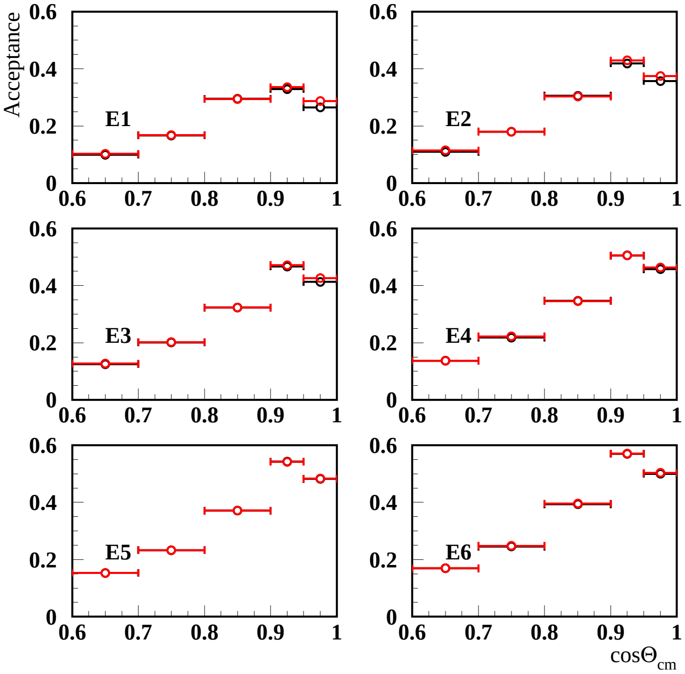

Figure 3.19: Acceptance of LEPS spectrometer for the p($\vec{\gamma}$,K^+)$\Sigma(1385)/\Lambda(1405)$; the black circles for the horizontally polarized photons and the red circles for the vertically polarized photons.

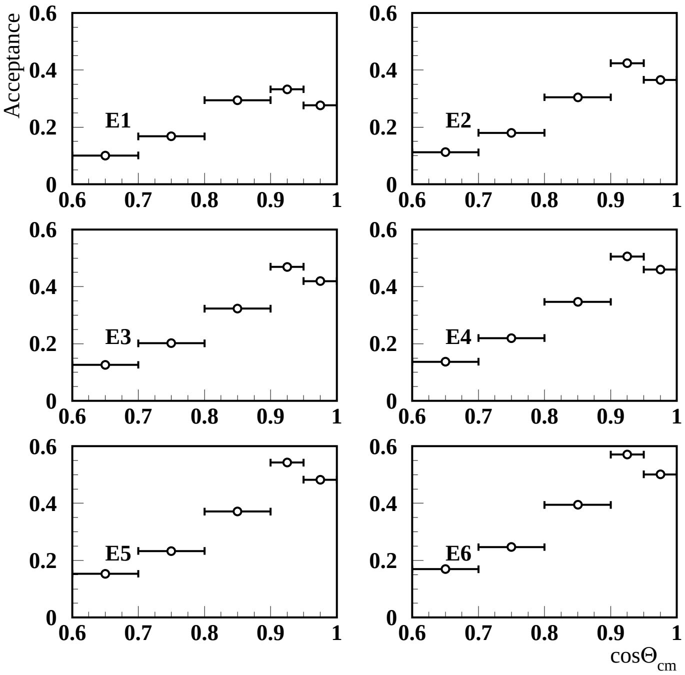

Figure 3.20: Averaged acceptance of LEPS spectrometer for the p($\vec{\gamma}$,K^+)$\Sigma(1385)/\Lambda(1405)$.

Chapter 4

Results

The differential cross sections were accurately measured as a function of the K$^+$ forward scattering angle ($0.6 < cos\Theta_{cm}^{K^+} < 1.0$) and the momentum transfer $\tilde{t}$ at the 1.5< E_γ <2.4 GeV photon energy regions with high statistics.

4.1 Differential cross sections for $\Sigma(1385)/\Lambda(1405)$

4.1.1 Differential cross sections ($\frac{d\sigma}{dcos\Theta_{cm}^{K^+}}$)

The differential cross sections defined as $\frac{d\sigma}{dcos\Theta_{cm}^{K^+}}$ are given as follows;

$$\frac{d\sigma}{dcos\Theta_{cm}^{K^+}} = \frac{N_{K^+}}{A_{spectrometer} \cdot N_\gamma \cdot N_t \cdot dcos\Theta_{cm}^{K^+}}, \tag{4.1}$$

where denotes

N$_{K^+}$; yields for p($\vec{\gamma}$,K^+)$\Lambda(1405)/\Sigma(1385)$
A$_{spectrometer}$; acceptance for the p($\vec{\gamma}$,K^+)$\Lambda(1405)/\Sigma(1385)$ in LEPS spectrometer
N$_\gamma$; the number of photons at the target
N$_t$; number of protons inside the liquid hydrogen target cell
(N$_t$ = $0.708 g/cm^3 \times 16 cm \times 6.022 \times 10^{23}/1.00794 = 6.76821 \times 10^{23} [protons/cm^2]$)
$dcos\Theta_{cm}^{K^+}$; width of each bin

The number of photons(N$_\gamma$) in each photon energy bin was obtained, and the scale factor(F$_t$) for the probability of the number of the scattered electron tracks which are reconstructed in the tagger was determined to be 0.762 by using the differential cross sections for the π^0 photo production [69]. The beam transmission(T) which corrected rejection of shower is 52.6%. Therefore, the number of photons at the liquid hydrogen target is,

$$N_\gamma = N_{(tagged)\gamma} \cdot F_t \cdot T = N_{(tagged)\gamma} \cdot 0.762 \cdot 0.526 \tag{4.2}$$

Fig. 4.1 shows the yields(left figures) and acceptance(right figures) for $\Sigma(1385)/\Lambda(1405)$ as a function of $dos\Theta_{cm}^{K^+}$ in each photon energy region from E1(top) to E6(bottom). The yields of $\Sigma(1385)/\Lambda(1405)$ were obtained from the missing mass spectra in each $dos\Theta_{cm}^{K^+}$ and E$_\gamma$ region using the template fitting method I with a 0.05 bin width at $0.9 < cos\Theta_{cm}^{K^+} < 1.0$ and a 0.1 bin width at $0.6 < cos\Theta_{cm}^{K^+} < 0.9$.

Fig. 4.2 represents the differential cross sections of $\Sigma(1385)/\Lambda(1405)$ as a function of $dcos\Theta_{cm}^{K^+}$ in terms of the photon energy. The differential cross sections($d\sigma/dcos\Theta_{cm}^{K^+}$) have a forward peak at the high photon energy while the angular distributions are almost flat at the low photon energy region.

Fig. 4.3 represents the energy dependence of $\Sigma(1385)/\Lambda(1405)$. The differential cross sections for $\Sigma(1385)/\Lambda(1405)$ show the gradually increase as the photon energy increases as shown in Fig. 4.3 (a) and (b) while the differential cross sections decrease as the photon energy increases as shown in Fig. 4.3 (d) and (e).

The differential cross sections for $\Sigma(1385)/\Lambda(1405)$ are listed at Table. 4.1 in each photon energy and angular bin.

The differential cross sections of $\Sigma(1385)/\Lambda(1405)$ from the previous LEPS/TPC experiment(black circles) [20] and this LEPS/K^+ experiment (blue circles) were compared as shown in Fig. 4.4. The weighted mean value of the three angular/photon energy regions was obtained at 0.8< $cos\Theta_{cm}^{K^+}$ <1.0 from the LEPS/K^+ measurement results. Both of the experimental results are quite similar, but the LEPS/K^+ results are slightly smaller than those of the LEPS/TPC measurement results at the overall photon energy regions with the large systematic errors.

Our LEPS/K^+ experimental data were also compared with other experimental results with the sum of $\Sigma(1385)$ and $\Lambda(1405)$ by JLAB/CLAS [22] preliminary results, as shown in Fig. 4.5. (Note that the corresponding photon energy regions are slightly different in each photon energy bin.) The blue circles indicate the LEPS/K^+ data and red circles indicate the JLAB/CLAS data, respectively.

The JLAB/CLAS data also shows the enhancement in a forward angle as the photon energy increases while the differential cross sections are flat or decrease near the threshold energy region(black squares of Fig. 4.5(a)). Our LEPS/K^+ data have similar angular dependence with JLAB/CLAS results and almost the same near the threshold energy region as shown in Fig. 4.4(a). Moreover, our LEPS/K^+ result are almost similar with the JLAB/CLAS data at 0.6< $cos\Theta_{cm}^{K^+}$ <0.8 angle region of overall photon energy region, but there are large discrepancy at $1.8 < E_\gamma < 2.0$ GeV region as shown in Fig. 4.4(c). The LEPS spectrometer has good forward angle coverage while other experiments have poor forward angle coverage though the JLAB/CLAS spectrometer cover the almost 4π angles. The magnitudes of the differential cross sections are smaller than JLAB/CLAS data.

4.1.2 Differential cross sections ($\frac{d\sigma}{d\tilde{t}}$)

The differential cross sections defined as $\frac{d\sigma}{d\tilde{t}}$ are given as follows;

$$\frac{d\sigma}{d\tilde{t}} = \frac{N_{K^+}}{A_{spectrometer} \cdot N_\gamma \cdot N_t \cdot d\tilde{t}}, \tag{4.3}$$

where denotes $d\tilde{t}$ is width of each bin, and N_{K^+}, $A_{spectrometer}$, N_γ and N_t denote as the same as Eq. 4.3.

Differential cross sections $d\sigma/d\tilde{t}$ in terms of photon energy were obtained as a function of momentum transfer for $\Sigma(1385)/\Lambda(1405)$ events. The momentum transfer for each $t+|t|_{min}(=\tilde{t})$ interval are divided by 0.02 GeV^2 in $-0.1<\tilde{t}<0$, 0.05 GeV^2 in $-0.2<\tilde{t}<-0.1$ and 0.1 GeV^2 in $-0.6<\tilde{t}<-0.2$.

Fig. 4.6 shows the yields(left figures) and acceptance(right figures) for $\Sigma(1385)/\Lambda(1405)$ as a function of $\tilde{t}$ in terms of photon energy from E1(top) to E6(bottom). The yields of $\Sigma(1385)/\Lambda(1405)$ were obtained from the missing mass spectra in each $\tilde{t}$ and E_γ regions using the template fitting method I. Our LEPS spectrometer have very good forward angle coverage, the $\Sigma(1385)/\Lambda(1405)$ events were measured at very forward angle regions precisely with high statistics by LEPS spectromter. It was found that the yields and acceptance decrease as momentum transfer $\tilde{t}$ becomes large.

The differential cross sections, $d\sigma/d\tilde{t}$ in terms of photon energy were obtained as shown in Fig. 4.7. The differential cross sections are almost flat at the low photon energy regions while they decrease in the photon energy regions from E3 to E6 as $\tilde{t}$ becomes increase. The results indicate the contribution of $t-$channel meson exchange is dominant at the high photon energy regions.

Fig. 4.8 shows the results after the exponential fit to the differential cross sections of $\Sigma(1385)/\Lambda(1405)$. The fitting function is shown as follows;

$$\frac{d\sigma}{d\tilde{t}} = \sigma_0 exp(-b\tilde{t}), \tag{4.4a}$$

where b is a slope parameter and σ_0 is $d\sigma/d\tilde{t}$ at $\tilde{t}=0$.

We firstly fitted the differential cross sections for the whole $\tilde{t}$ regions as shown in Fig. 4.8(a). In addition, as shown in Fig. 4.8(b), we performed the fitting for the specified $\tilde{t}$ regions since the acceptance and kinematic coverage $\tilde{t}$ regions are different as the photon energy ranges. The fitting ranges in each photon energy region are as follows: from T2 to T9 regions for E1 and E2 regions, from T2 to T10 regions for E3 and E4 regions and from T2 to T11 regions for E5 and E6 regions. The red-dotted vertical lines as shown in Fig. 4.8(b) represent the fitting range of each photon energy region.

Fig. 4.9(a) shows the slope parameters of $\Sigma(1385)/\Lambda(1405)$ depending on the photon energy which was obtained by the fitting, and we found that they become large as the photon energy increases. The blue-closed circles indicate the results obtained after fitting for whole the $\tilde{t}$ ranges and red-open circles show the results after the fitting for the selected $\tilde{t}$ regions.

4.2 Photon beam asymmetries for the $\vec{\gamma}p \rightarrow K^{+}\Sigma(1385)/\Lambda(1405)$

The photon beam asymmetry(Σ) was obtained by using horizontally and vertically polarized photon beams. The relation between the photon beam asymmetry and the producution yields is as follows :

$$\frac{nN_V - N_H}{nN_V + N_H} = P\Sigma cos(2\phi_{K+}), \tag{4.5}$$

where N_H is the K$^+$ photoproduction yield with the horizontally polarized photons and N_V is the K$^+$ photoproduction yield with the vertically polarized photons. The yields of N_H and N_V were obtaind after correction of the acceptance in the LEPS spectrometer. n is the normalization factor which was obtained by using the number of the horizontally polarized photons(n_h) and the vertically polarized photons(n_v).

$$n = \frac{n_h}{n_v} \tag{4.6}$$

The number of photons at the tagger were explained in Appendix A. And the linear polarization(P) is given by [56] :

$$P_\gamma = P_{laser}\frac{(1 - cos\alpha)^2}{2(\chi + 1 + cos^2\alpha)} \tag{4.7}$$

The multi-line mode of Ar laser was used in this experiment from 333.6 nm to 363.8 nm. The 351.1 nm wavelength was used to calculate the photon polarization. The polarization of laser photons, P$_{laser}$ was measured by every run and obtained as 92.22 % and 94.38 % in the horizontally and the vertically polarized photon beam, respectively. The average P$_{laser}$ is 93.307 % for LLH2 data sets. A slightly lower value of P$_{laser}$ was measured in LLH2 data sets. It resulted from some inaccurate measurements of the laser polarizaiton during the experiment. The photon polarization P$_\gamma$ was calculated event by event using Eq. 4.7. After that, the average photon polarization was obtained with the horizontally and the vertically polarized photons.

The Fig. 4.10 shows the coordinate frame for $\vec{\gamma}p \rightarrow K^{+}\Sigma(1385)/\Lambda(1405)$ photoproduction process. The z axis is the direction of the photon beam and the xz frame defines the reaction plane.

If the number of the vertically polarized photons is larger than that of the horizontally polarized photons, then Σ gives a positive value, and we can assume the magnetic component is dominant in a t-channel process. If the number of the horizontally polarized photons is larger than that of the vertically polarized photons, then Σ gives a negative value and we can assume the electric component is dominant in a t-channel process. To measure the photon beam asymmetry(Σ) precisely, it is important to get the yields of signals after subtracting the background events in each azimuthal ϕ_{K^+} angle bin with high statistics.

4.2.1 Azimuthal angle distributions

The $\Sigma(1385)/\Lambda(1405)$ events were obtained with the template fitting into the missing mass distributions on each azimuthal angle and photon energy bins as shown in Appendix C(C.1-C.6).

The K$^+$ azimuthal angle distributions(ϕ_{K^+}) were obtained by the horizontally and the vertically polarized photon beams in term of the photon energy regions(E1-E6). The ϕ_{K^+} angle distributions of $\Sigma(1385)/\Lambda(1405)$ by Method I(a) and Method II(b) were obtained for 6 different photon energy regions as shown in Fig. 4.11. The black circles are for the horizontally polarized photon case and the red circles are for the vertically polarized photon case. Their yields and acceptance by the LEPS spectrometer were obtained as shown in Fig. 4.11. The yields of $\Sigma(1385)/\Lambda(1405)$ after acceptance correction were used to get photon beam asymmetry.

4.2.2 Photon beam asymmetries

The photon beam asymmetries for $\Sigma(1385)/\Lambda(1405)$ were measured in the 6 different photon energy regions at 1.5 GeV $\leq$ E$_\gamma$ $\leq$ 2.4 GeV and with two K$^+$ polar angle ranges(0.6 $\leq$ cosΘ_{cm,K^+} $\leq$ 0.9 and 0.9 $\leq$ cosΘ_{cm,K^+} $\leq$ 1). The ratios of $(n \cdot N_v - N_h)/(n \cdot N_v + N_h)$ were plotted as a function of the K$^+$ azimuthal angle(ϕ_{K^+}), and the data points were fitted with a function of cos($2\phi_{K^+}$)(red solid line). The amplitude $P\Sigma$ was obtained by cosine fitting, and the photon beam asymmetry was obtained by using the fitting results and the measured polarization event by event. Fig. 4.12 and Fig. 4.13 show the azimuthal angle distributions of the ratio R for the $\Sigma(1385)/\Lambda(1405)$ obtaind by Mehtod I and Method II, repectivley. Each spectra show the results for each photon energy region from the low photon energy to the high photon energy region.

Fig 4.14 represents the photon beam asymmetries for $\Sigma(1385)/\Lambda(1405)$ with 2 different polar angular regions. The photon beam asymmetries for $\Sigma(1385)/\Lambda(1405)$ are small in all photon energy regions, and their amplitudes become large as the photon energy increases as shown in Fig. 4.14. The blue circles were measured by the template fitting method I, the red circles are measured by the template fitting method II.

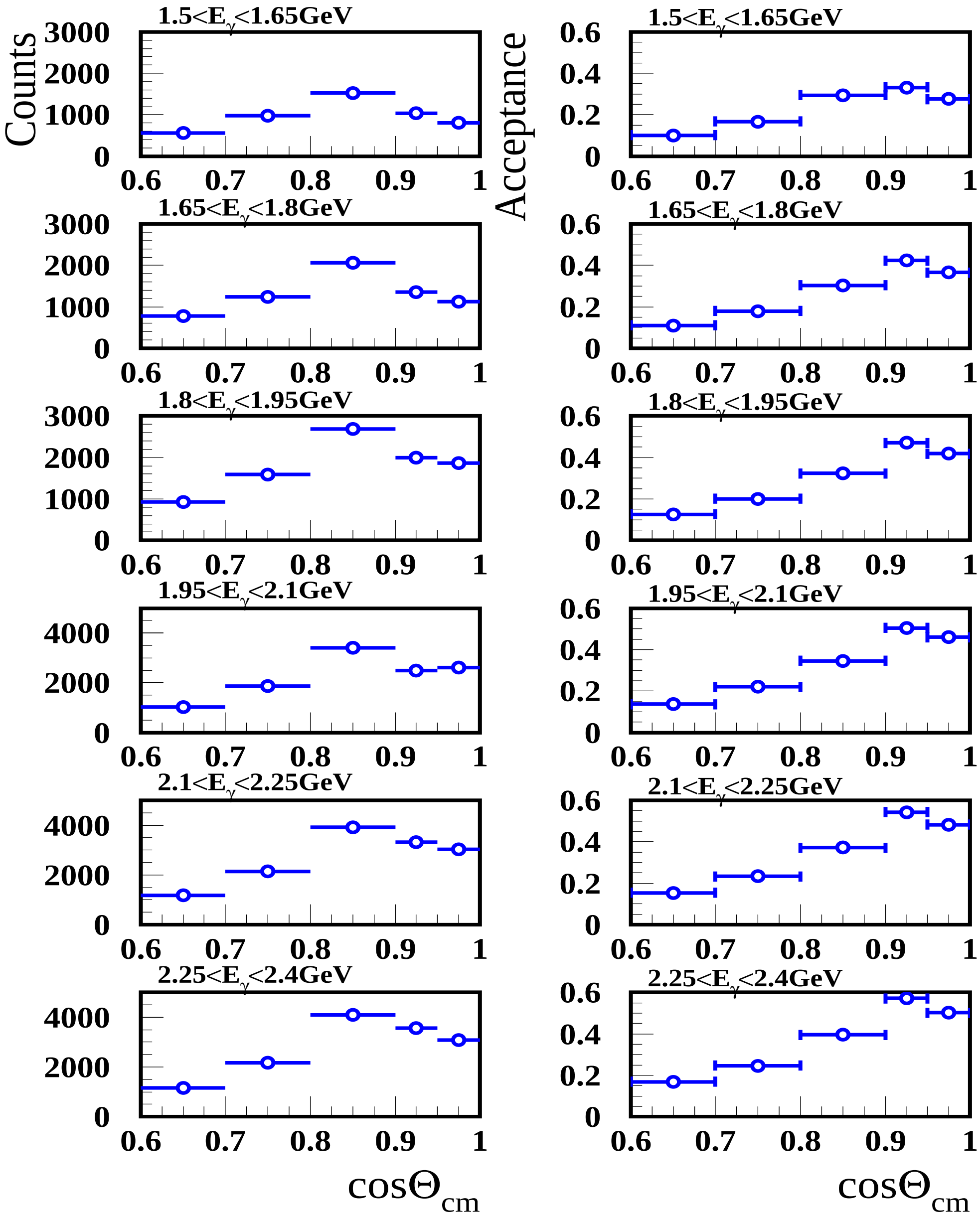

Figure 4.1: Yields and acceptance for Σ(1385)/Λ(1405) as a function of $dcos\Theta_{cm}^{K^+}$

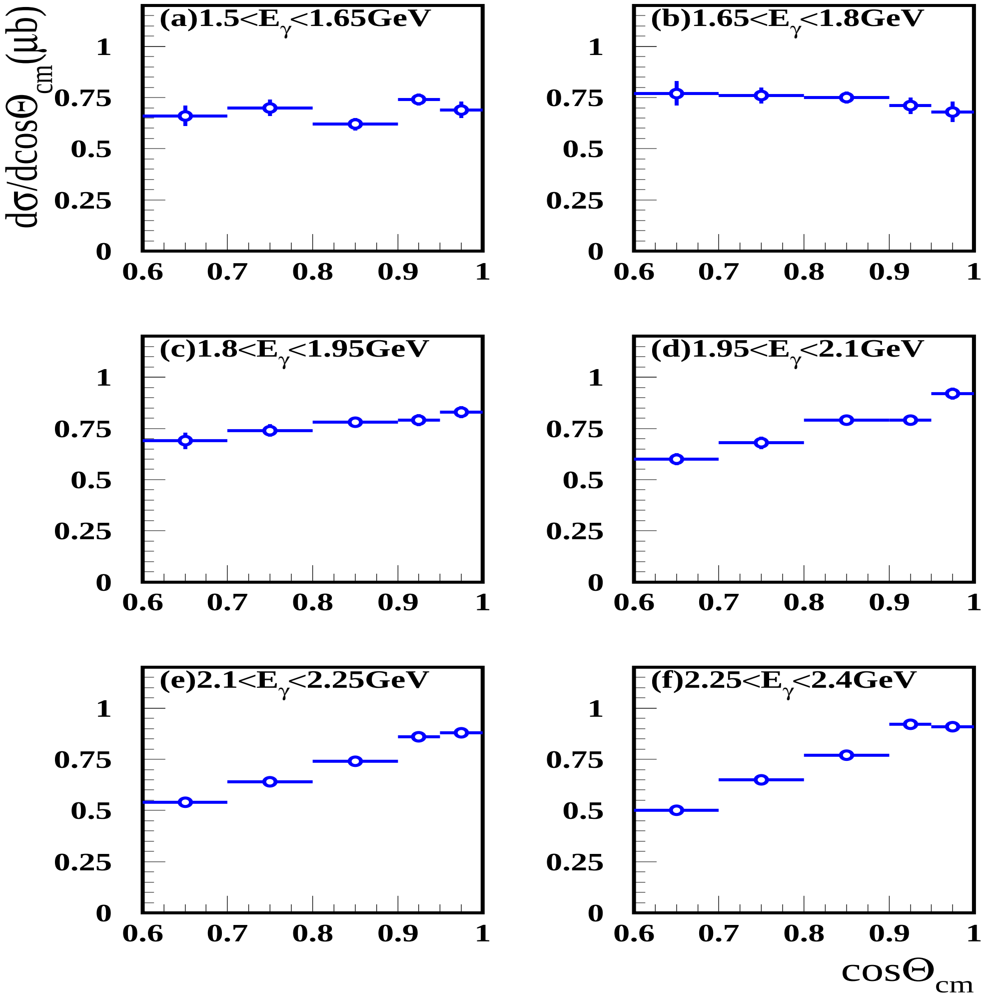

Figure 4.2: Differential cross sections for $\Sigma(1385)/\Lambda(1405)$ as a function of $dcos\Theta_{cm}^{K^+}$

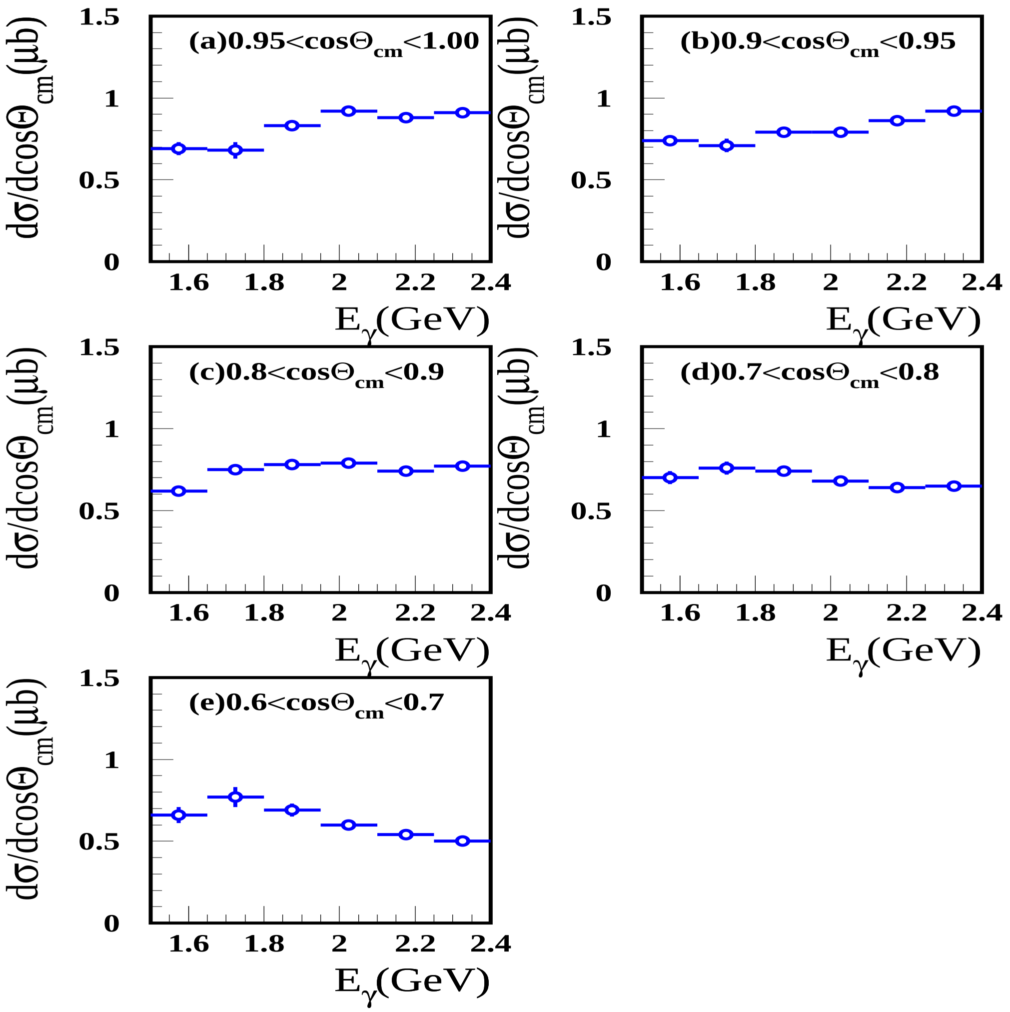

Figure 4.3: Differential cross sections for $\Sigma(1385)/\Lambda(1405)$ as a function of E_γ

E_γ (GeV)	$\cos\Theta_{cm}^{K+}$	$d\sigma/dcos\Theta_{cm}^{K+}$ ± statistical error
1.575	0.65	0.69 ± 0.04
	0.75	0.74 ± 0.03
	0.85	0.62 ± 0.03
	0.925	0.70 ± 0.04
	0.975	0.66 ± 0.05
1.725	0.65	0.68 ± 0.05
	0.75	0.71 ± 0.04
	0.85	0.75 ± 0.03
	0.925	0.76 ± 0.04
	0.975	0.77 ± 0.06
1.875	0.65	0.83 ± 0.03
	0.75	0.79 ± 0.03
	0.85	0.78 ± 0.02
	0.925	0.74 ± 0.03
	0.975	0.69 ± 0.04
2.025	0.65	0.92 ± 0.03
	0.75	0.79 ± 0.02
	0.85	0.79 ± 0.02
	0.925	0.68 ± 0.03
	0.975	0.60 ± 0.03
2.175	0.65	0.88 ± 0.02
	0.75	0.86 ± 0.02
	0.85	0.74 ± 0.02
	0.925	0.64 ± 0.02
	0.975	0.54 ± 0.02
2.325	0.65	0.91 ± 0.02
	0.75	0.92 ± 0.02
	0.85	0.77 ± 0.02
	0.925	0.65 ± 0.02
	0.975	0.50 ± 0.02

Table 4.1: Differential cross sections for $\Sigma(1385)/\Lambda(1405)$

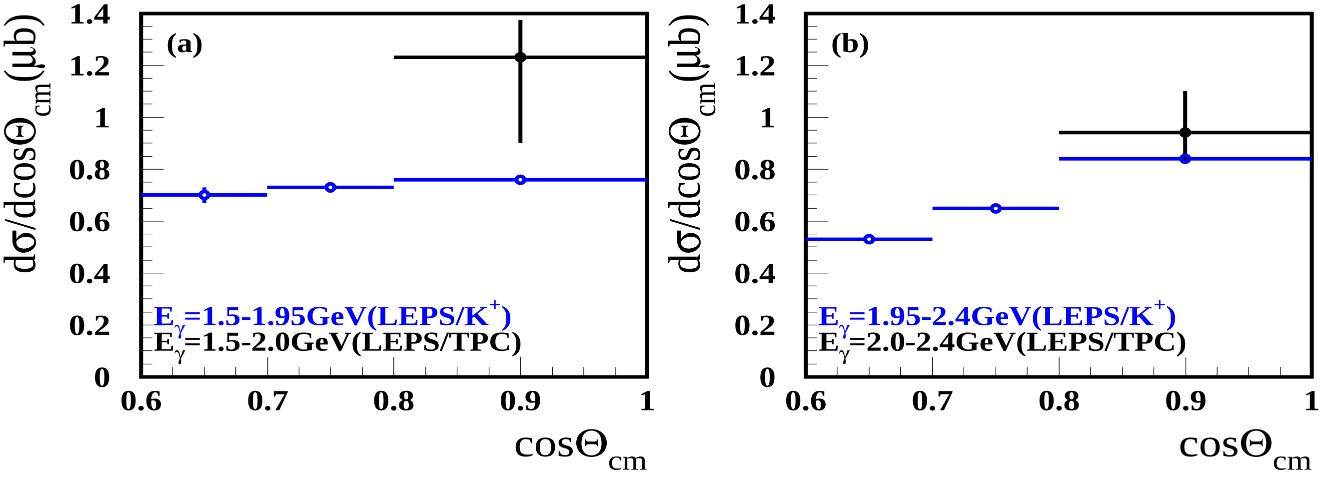

Figure 4.4: Comparisons of the differential cross sections for $\Sigma(1385)/\Lambda(1405)$ hyperons between LEPS/K^+(blue circles), LEPS/TPC(black circles) experimental results

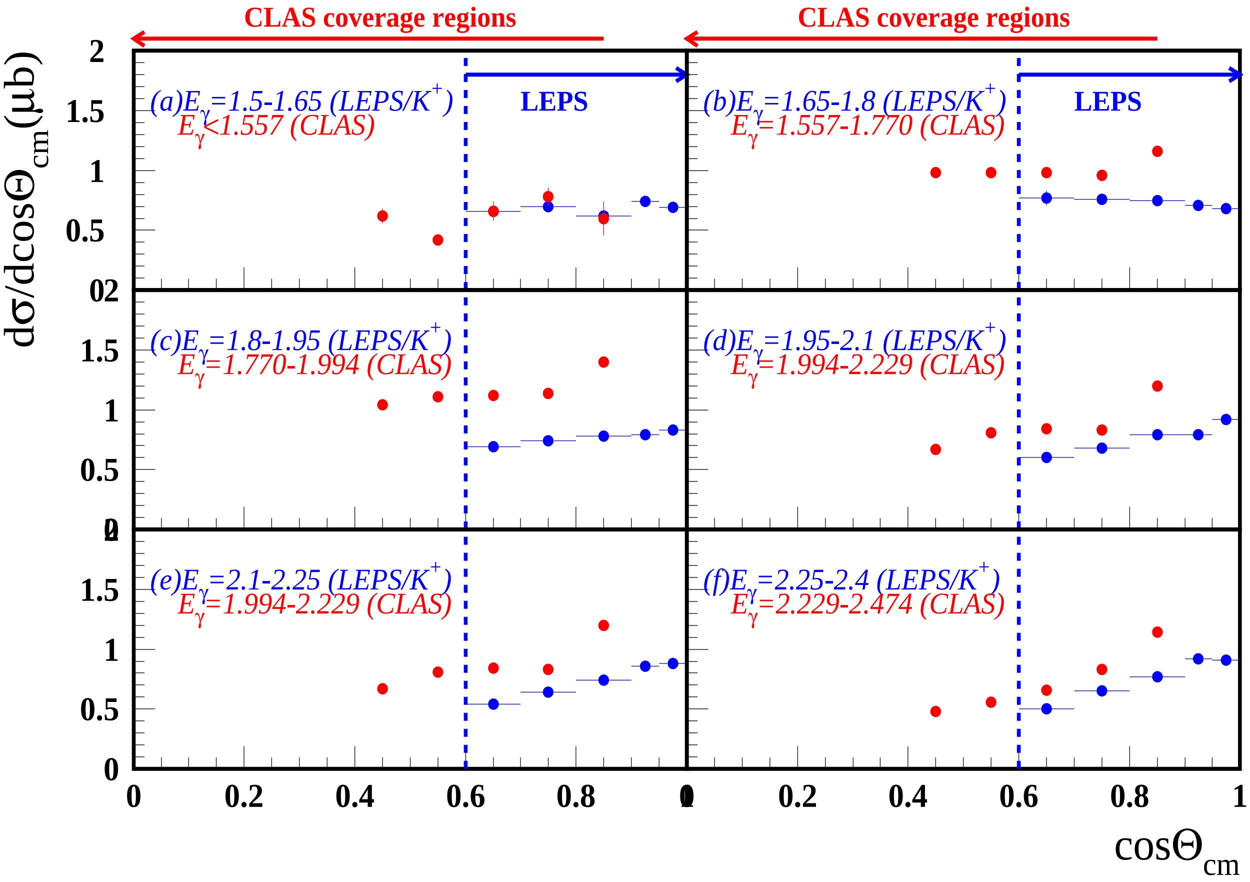

Figure 4.5: Comparisons of the differential cross sections for $\Sigma(1385)/\Lambda(1405)$ between LEPS/K^+(blue circles) and JLAB/CLAS experimental results(red circles). The preliminary JLAB/CLAS results are just represented with $cos\Theta_{cm}^{K+}$ >0.4 region and more detailed preliminary results of the overall angular region are shown in Fig. 1.3.

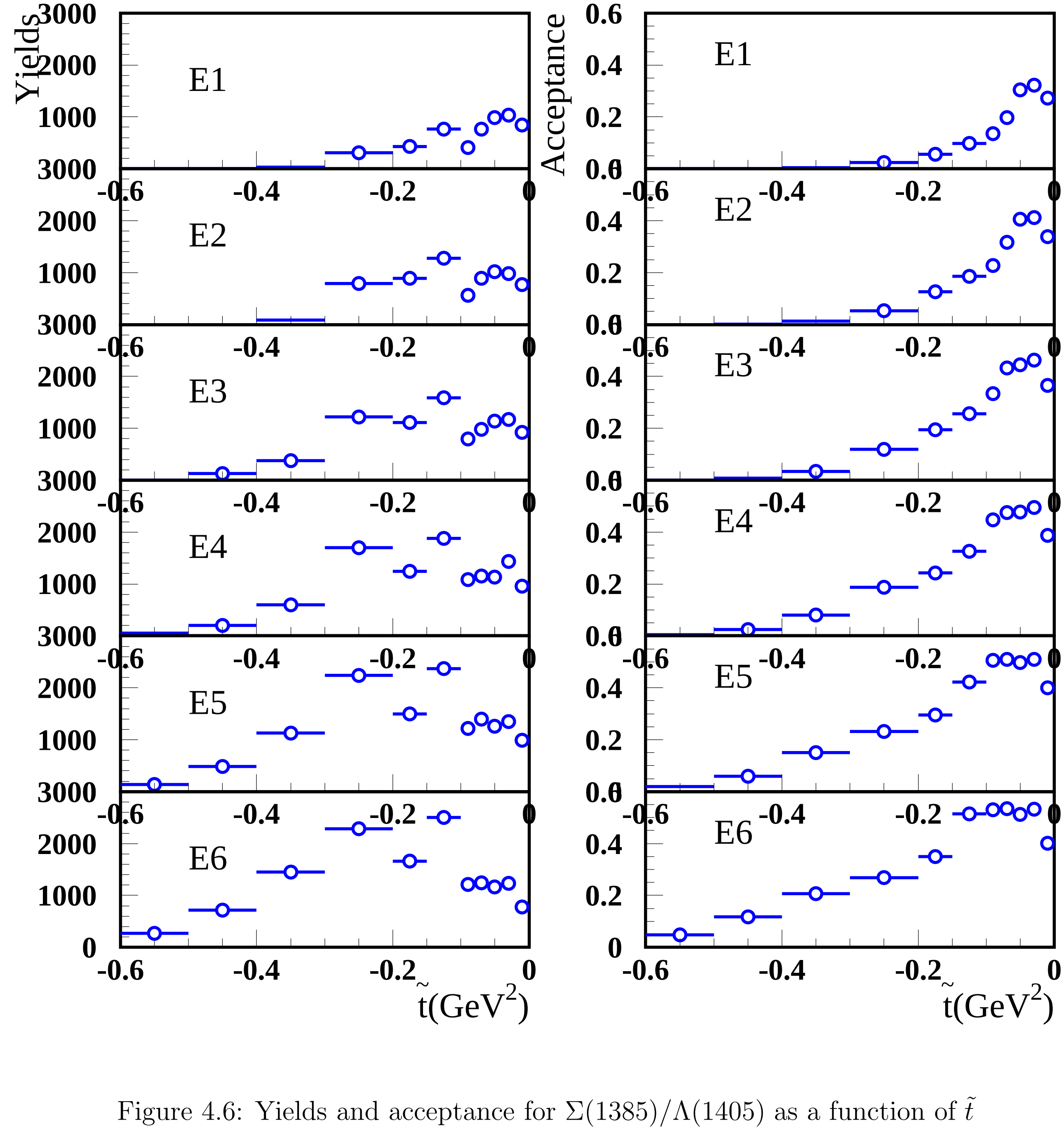

Figure 4.6: Yields and acceptance for $\Sigma(1385)/\Lambda(1405)$ as a function of $\tilde{t}$

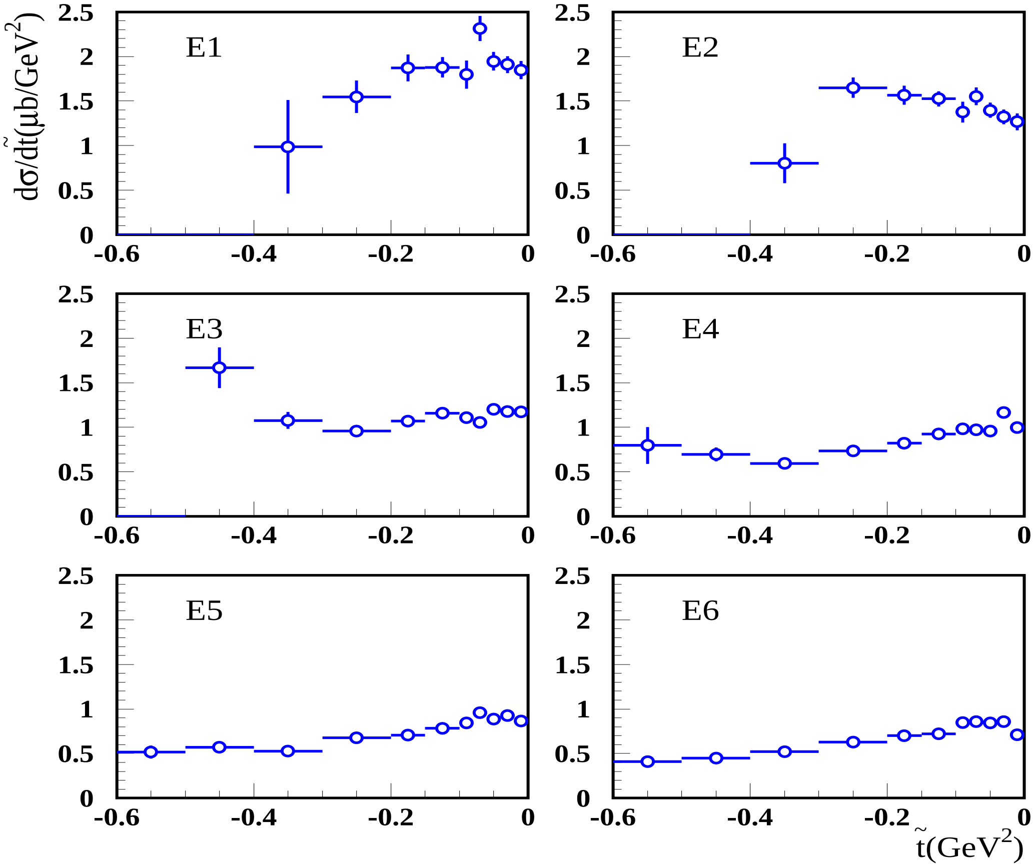

Figure 4.7: Differential cross sections for $\Sigma(1385)/\Lambda(1405)$ as a function of $d\tilde{t}$

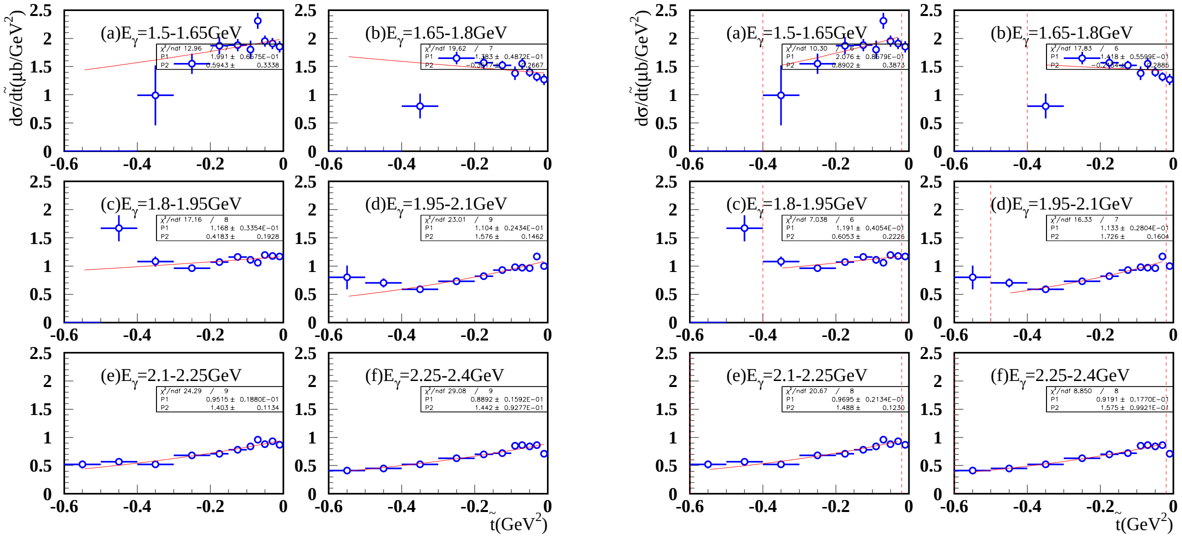

(a) (b)

Figure 4.8: Exponential fit to differential cross sections of Σ(1385)/Λ(1405)

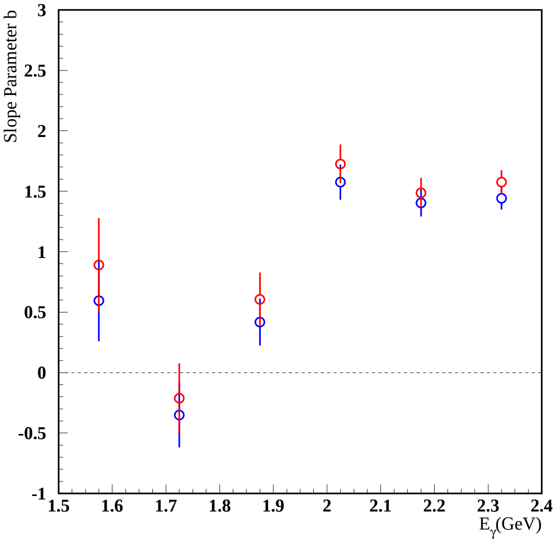

Figure 4.9: Slope parameter of Σ(1385)/Λ(1405)

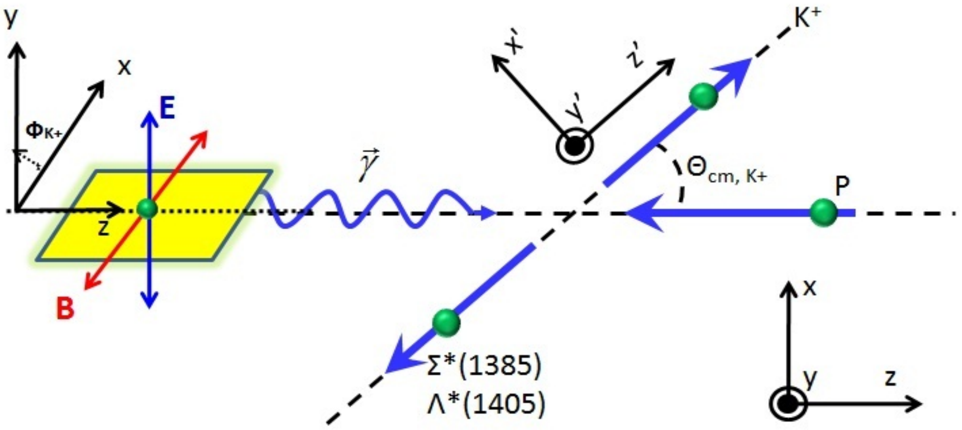

Figure 4.10: Coordinate frame for $\vec{\gamma}p \rightarrow K^+\Sigma(1385)/\Lambda(1405)$ photoproduction process

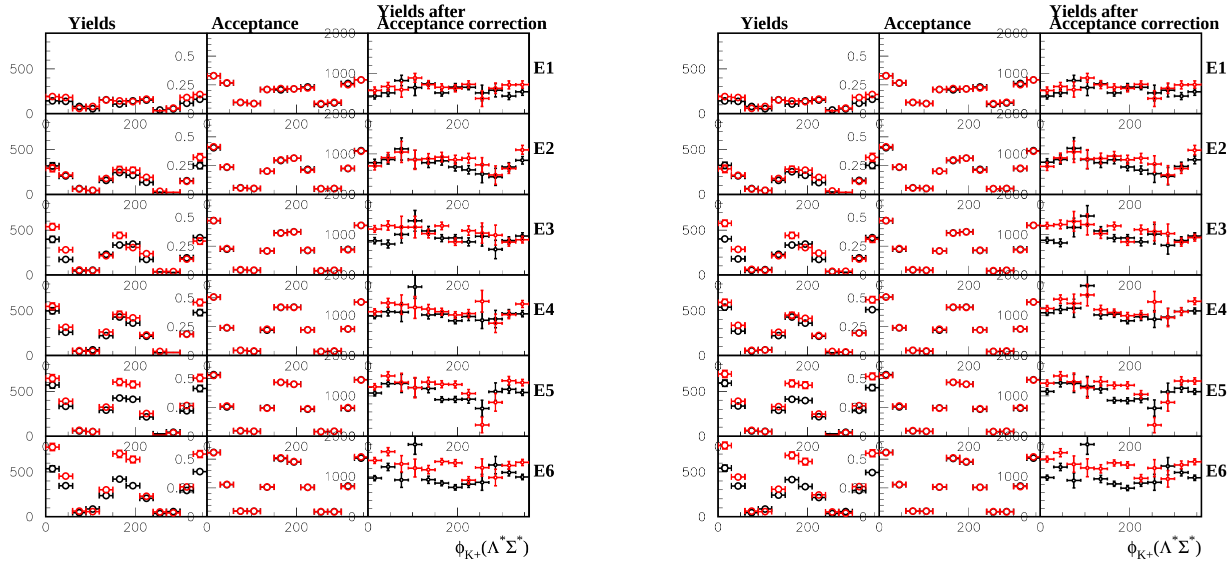

(a) (b)

Figure 4.11: Azimuthal angle dependence of $\Sigma(1385)/\Lambda(1405)$ (a) Method I (b) Method II

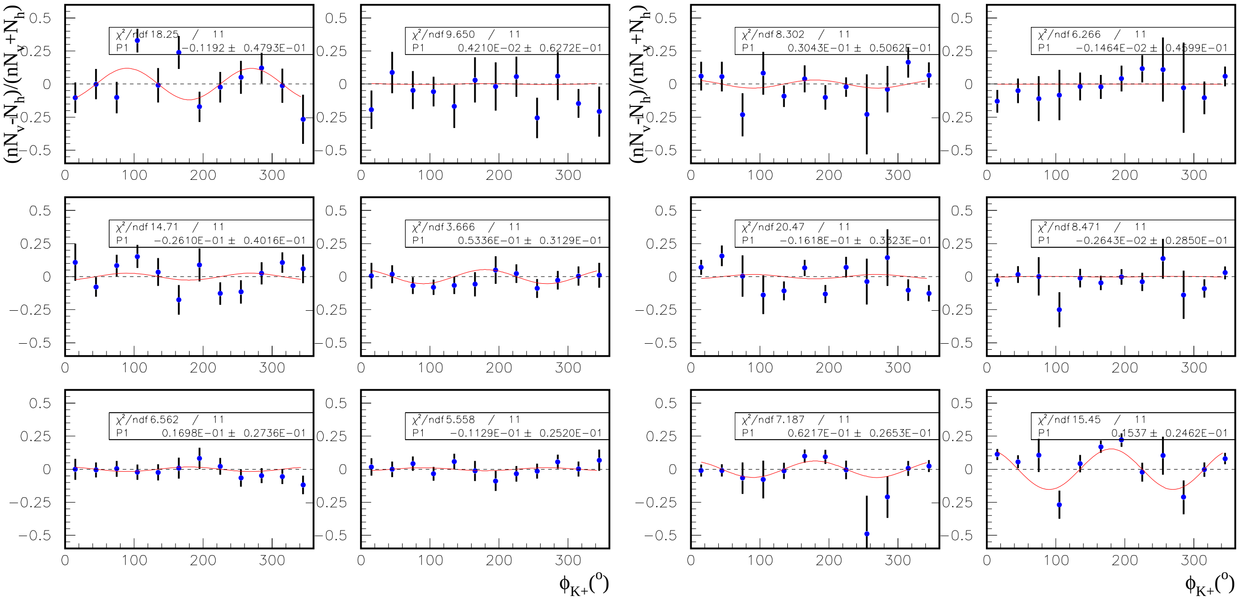

(a) $0.9 \le \cos\Theta_{cm,K^+} \le 1.0$ (b) $0.6 \le \cos\Theta_{cm,K^+} \le 0.9$

Figure 4.12: ϕ distribution of the ratio R for the $\Sigma(1385)/\Lambda(1405)$(Method I)

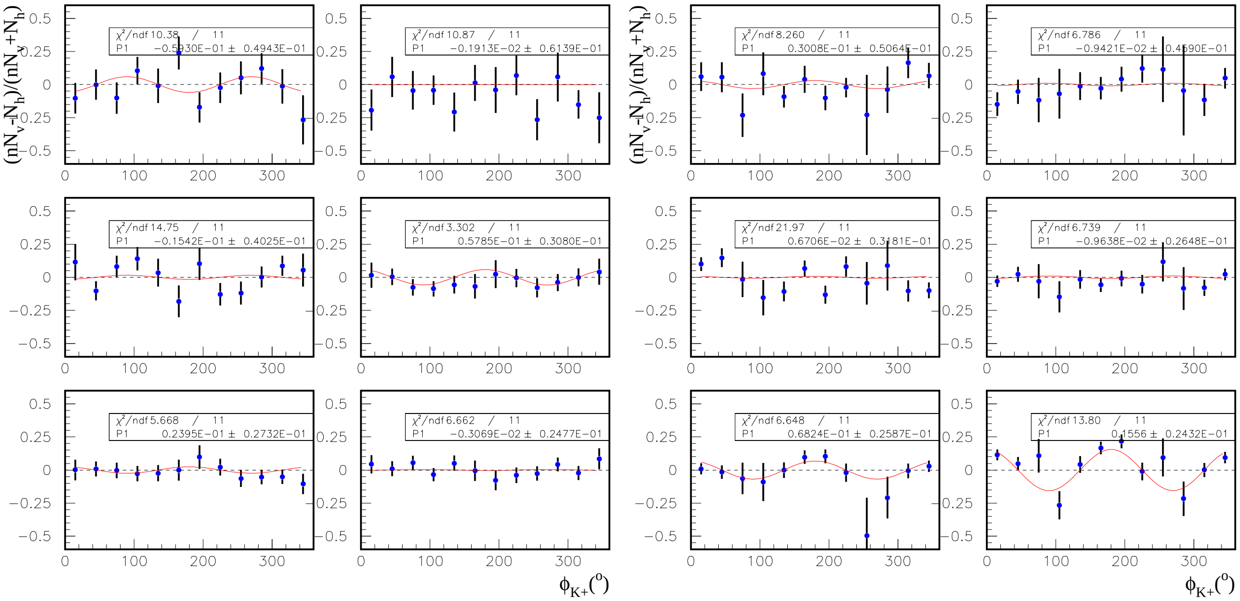

(a) $0.9 \le \cos\Theta_{cm,K^+} \le 1.0$ (b) $0.6 \le \cos\Theta_{cm,K^+} \le 0.9$

Figure 4.13: ϕ distribution of the ratio R for the $\Sigma(1385)/\Lambda(1405)$(Method II)

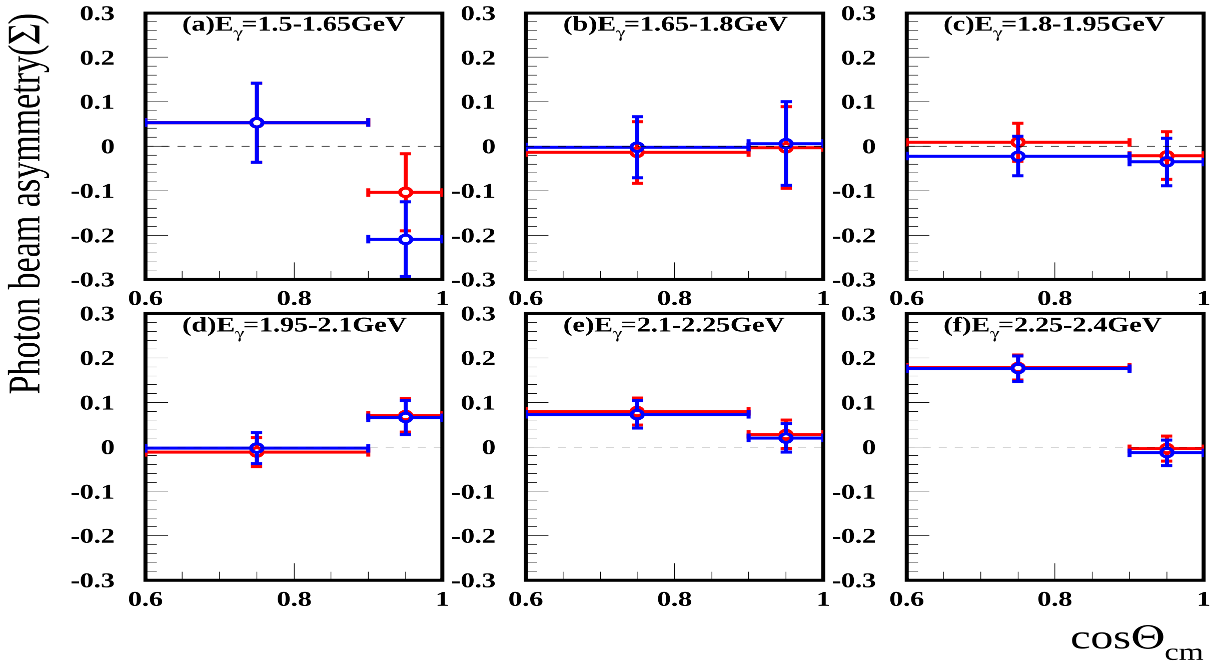

Figure 4.14: Photon beam asymmetries for the $\Sigma(1385)/\Lambda(1405)$ (Method I(blue) and Method II(red))

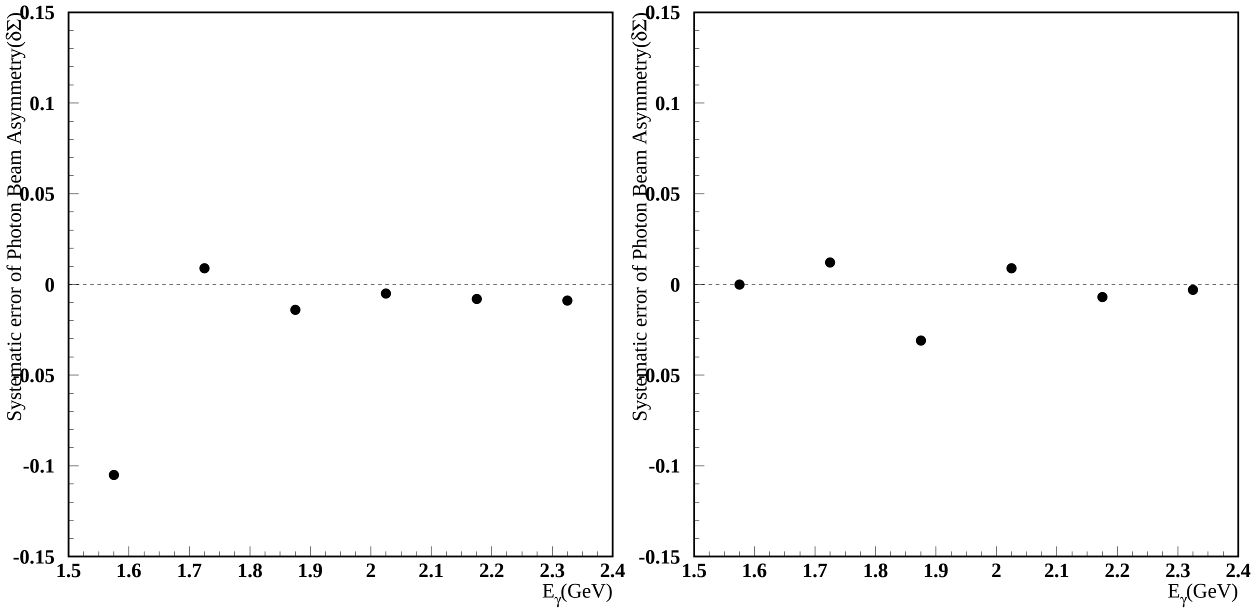

(a) $0.9 \leq \cos\Theta_{cm,K^+} \leq 1.0$ (b) $0.6 \leq \cos\Theta_{cm,K^+} \leq 0.9$

Figure 4.15: Systematical error of photon beam asymmetries for the $\Sigma(1385)/\Lambda(1405)$

Chapter 5

Conclusions and Discussions

The differential cross sections and photon beam asymmetries were measured to decompose the contributions of the pseudoscalar meson(K^-) and the vector meson(K^*) exchange in the $t-$channel for $\Sigma(1385)/\Lambda(1405)$ photoproduction.

Fig. 5.1 shows the angular dependence of the differential cross sections for the $\vec{\gamma}p \rightarrow K^+\Sigma(1385)/\Lambda(1405)$ reaction. The differential cross sections for $\Sigma(1385)/\Lambda(1405)$ have a forward peak at the high photon energy regions as shown in Fig. 5.1(c)∼(f) and the characteristic of the forward peaking becomes more clearly seen as the photon energy increases. On the other hand, the differential cross sections at the low photon energies are almost flat and slightly decrease at the very forward angle as shown in Fig. 5.1(a) and (b).

The differential cross sections($\frac{d\sigma}{d\tilde{t}}$) for $\Sigma(1385)/\Lambda(1405)$ were obtained as shown in Fig. 5.2. They decrease as the momentum transfer($|\tilde{t}|$) increases at the high photon energy regions. The slightly fall-off pattern at $\tilde{t}$∼0 is seen. This indicates the contribution of the pseudoscalar meson(K^-) exchange in the $t-$channel because of the momentum coupling at the vertex point.

Our experimental results were compared with the theoretical calculations as shown in Fig. 5.3. The green curves show the results of $\Sigma(1385)$ calculated by Oh *et al.* [31] and the red curves show the results of $\Lambda(1405)$ calculated by Nam *et al.* [32] using effective Lagrangian model. (Note that the theoretical curves of $\Lambda(1405)$ are shown with a factor 10 scaled to show the angular dependence of the differential cross sections because their magnitudes are very small.) The theoretical curves for $\Sigma(1385)$ show a forward peaking behavior as the photon energy increases. This behavior indicate the contribution of the K^* exchange. On the other hand, the theoretical curves for $\Lambda(1405)$ show the slight decrease at the forward angle in the overall photon energy regions. With these model calculations, we decomposed the contribution of $t-$channl meson exchanges from this experiment. We conclude that the forward peaking behavior indicates the K^* meson exchange(natural parity exchange) for $\Sigma(1385)$ is dominant at the high photon energy, and the flat and slilgtly decrease angular distributions at the very forward angle regions indicate the K^- meson exchange(unnatural parity exchange) for $\Lambda(1405)$ becomes dominant at the low photon energy region.

Moreover, Oh's and Nam's model calculation used the different form factor structure, coupling strength and cutoff mass, and their model calculation were fitted to CLAS and LEPS/TPC data, respectively. Since the differential cross sections strongly depend on the choice of form factor structure and coupling strength, there can be found the discrepancy in

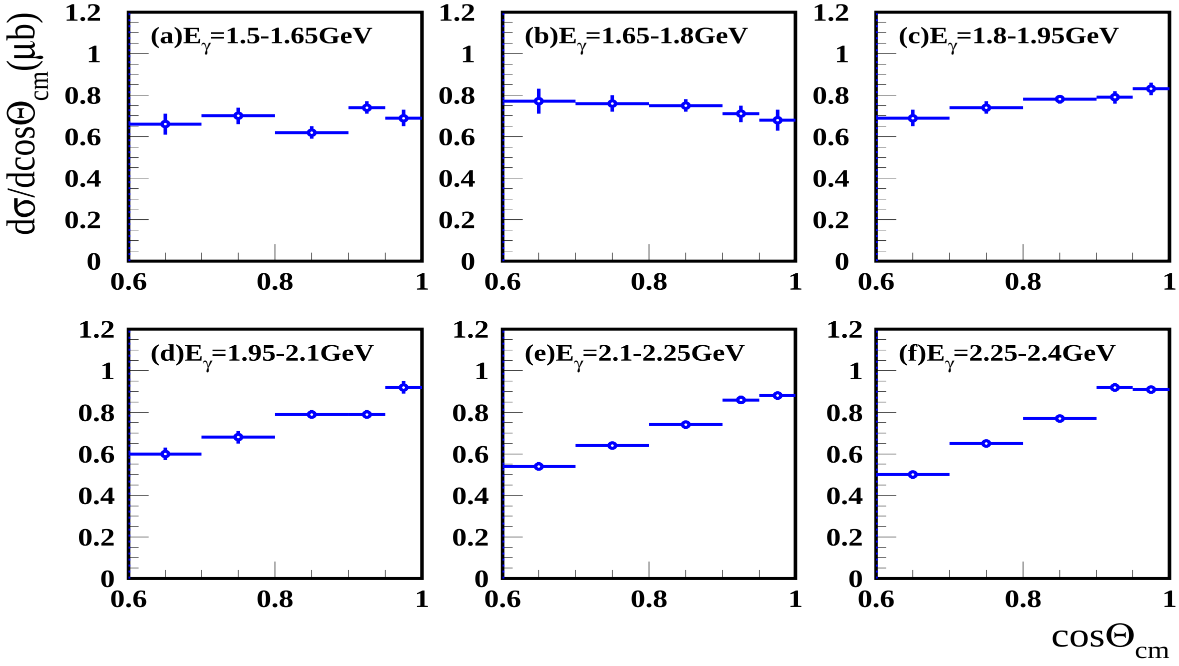

Figure 5.1: Differential cross sections ($\mathrm{d}\sigma/\mathrm{d}cos\Theta_{cm}^{K+}$) for the $\Sigma(1385)/\Lambda(1405)$ in terms of photon energy

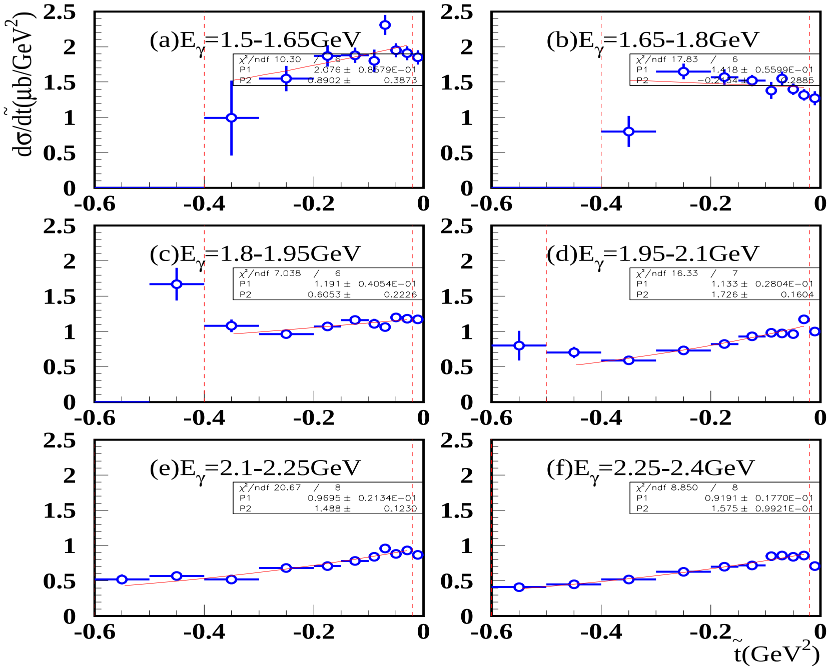

Figure 5.2: Differential cross sections($\mathrm{d}\sigma/\mathrm{d}\tilde{t}$) for the $\Sigma(1385)/\Lambda(1405)$ in terms of photon energy (The red-dotted vertical lines represent the fitting range of each photon energy region.)

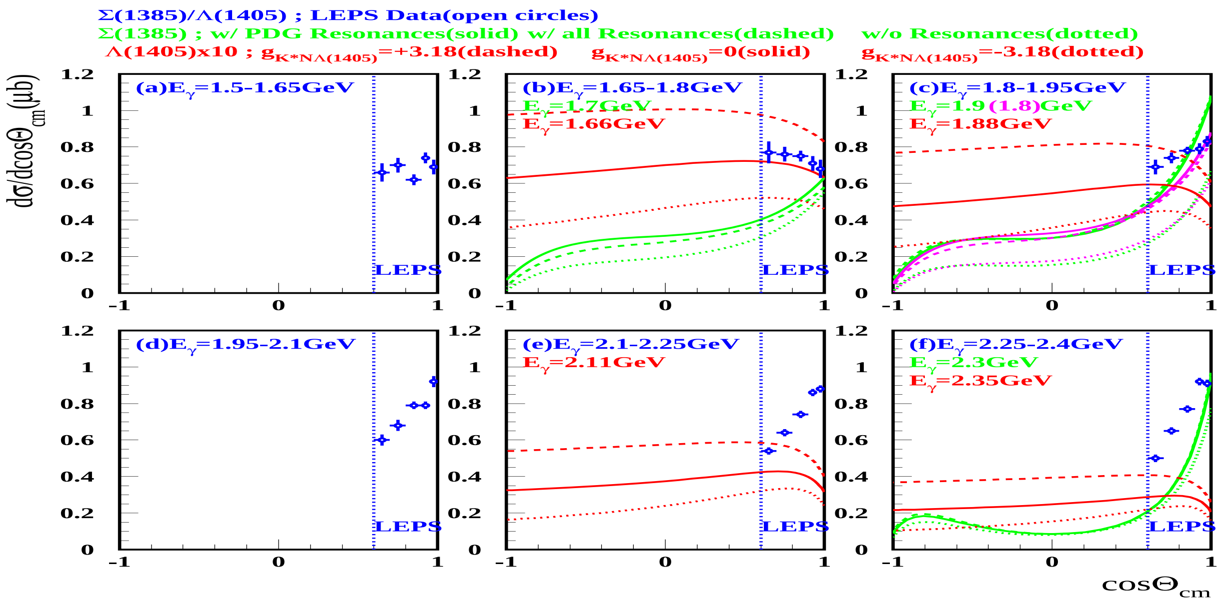

Figure 5.3: Differential cross sections as a function of $cos\Theta^{K+}_{cm}$ for $\Sigma(1385)/\Lambda(1405)$: The blue circles indicate with the LEPS/K^+ experimental data and the green(pink) and red lines indicate theoretical calculations of the $\Sigma(1385)$ and $\Lambda(1405)$, respectively. (Note that the results of $\Lambda(1405)$ are shown with a factor 10 scaled.) The blue-dotted vertical lines indicate the LEPS kinematical angular coverage regions.

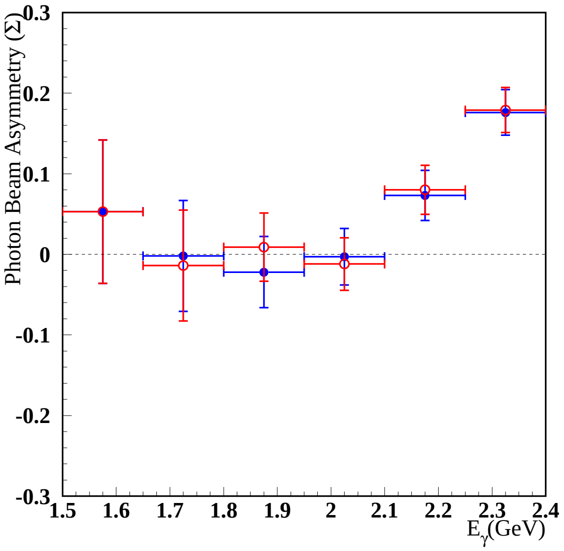

Figure 5.4: Energy dependence of the photon beam asymmetries for $\Sigma(1385)/\Lambda(1405)$ at 0.6 $\leq$ cosΘ_{cm,K^+} $\leq$ 0.9 regions. The blue and red colors indicate the obtained values by different template fitting method I and II, respectively.

the Oh's and Nam's model calculation. It is difficult to conclude the production mechanism for $\Sigma(1385)$ and $\Lambda(1405)$ with only the results of the differential cross sections. Therefore, the measurement of the photon beam asymmetry is necessary to understand the production mechanism for $\Sigma(1385)$ and $\Lambda(1405)$.

Our LEPS experimental results of the photon beam asymmetries for $\Sigma(1385)/\Lambda(1405)$ are the first measurements in the world and provide the information on the contributions of the $t-$channel meson exchanges(K^- or K^*). Fig. 5.4 shows the energy dependence of the photon beam asymmetries for $\Sigma(1385)/\Lambda(1405)$. The magnitudes of the photon beam asymmetries increase from 0 to the positive value as the photon energy increases above E_γ=2.1 GeV. The positive value at the high photon energy region indicates the K^* meson exchange contribution becomes larger than the K^- meson exchange contribution for $\Sigma(1385)/\Lambda(1405)$. It is difficult to differentiate K^- or K^* meson contribution for the $\Sigma(1385)$ and $\Lambda(1405)$ respectively only with the photon beam asymmetry results, because these results indicate the production mechanism for the $\Sigma(1385)/\Lambda(1405)$.

Since the differential cross sections of $\Sigma(1385)$ is larger than that of $\Lambda(1405)$ at the high photon energy regions as measured in the LEPS/TPC experiment [20], the forward peak of differential cross sections is expected to be mainly comes from $\Sigma(1385)$ at the high photon energy regions. Moreover, the positive values of the photon beam asymmetries indicate the K^* meson exchange(natural parity exchange) in the $t-$channel. Using the differential cross sections and the photon beam asymmetries results, we conclude that K^* meson exchange(natural parity exchange) for the $\Sigma(1385)$ becomes dominant at the high photon energy regions. We otained consistent results with the differential cross sections and the photon beam asymmetries.

The differential cross sections of $\Lambda(1405)$ at the low photon energy region is larger than at the high photon energy region, but still smaller than that of $\Sigma(1385)$ as measured in the

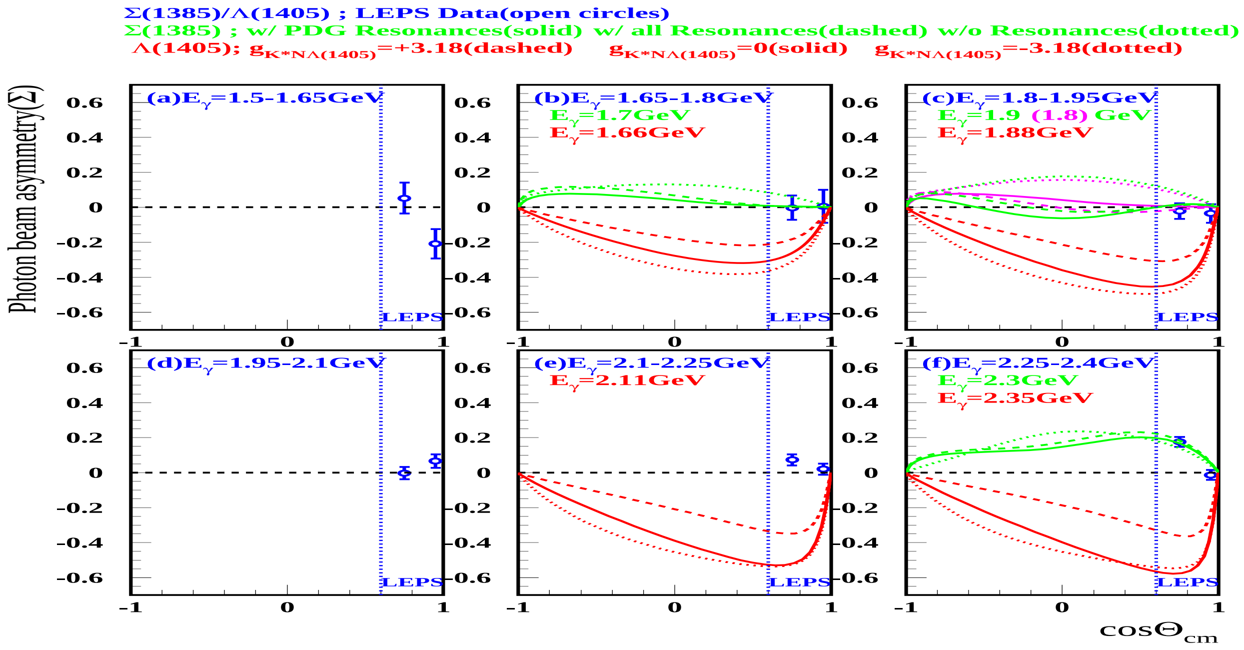

Figure 5.5: Photon beam asymmetries as a function of $cos\Theta_{cm}^{K+}$ for $\Sigma(1385)/\Lambda(1405)$: The indication is as same as Fig. 5.3.

LEPS/TPC experiment [20]. The $\Lambda(1405)$ begins to produce at the low photon energy regions. The destructive interferences between the K^- meson exchange for $\Lambda(1405)$ and the K^* meson exchange for $\Sigma(1385)$ are possible to make photon beam asymmetry(Σ)$\sim$0 for the $\Sigma(1385)/\Lambda(1405)$ photoproduction at the low photon energy region.

The photon beam asymmetry results were compared with the theoretical calculations as shown in Fig. 5.5. As shown in Fig 5.5(f), the model curve of $\Sigma(1385)$ reproduce experimental data at the high photon energy. Therefore, this measured photon beam asymmetries results represent the production mechanism of $\Sigma(1385)$ with the contribution of K^* meson exchange(natural parity exchange) at the high photon energy region. The model curves with/without K^* contribution do not change the sign of the photon beam asymmetries for $\Lambda(1405)$. This means the K^* meson exchange contribution for the $\Lambda(1405)$ is small.

Chapter 6

Summary

The photoproduction experiments for $\Sigma(1385)/\Lambda(1405)$ were carried out at SPring-8/LEPS. Differential cross sections and photon beam asymmetries were measured for the reaction of γp $\rightarrow K^+\Sigma(1385)/\Lambda(1405)$ by using a Liquid Hydrogen target with the LEPS forward spectrometer.

LEPS standard data acquisition was done with good forward acceptance. The LEPS detector is a forward magnetic spectrometer to identify the charged particles, and it consists of a start counter, a silicon vertex counter, an aerogel Cherenkov counter, three drift chambers, a dipole magnet and a wall of Time of Flight scintillation counters. The purpose of this experiment is to understand the production mechanism for the $\Sigma(1385)$ and $\Lambda(1405)$ hyperons by measuring the differential cross sections and photon beam asymmetries for the $\Sigma(1385)/\Lambda(1405)$ with high statistics at the K^+ forward angle region. The K^+ events were detected by the forward LEPS spectrometer and the $\Sigma(1385)/\Lambda(1405)$ were identified by means of the missing mass of K^+. We had the sufficient statistics with the missing mass of K^+ at the forward angles, we accurately measured the photon energy and angular dependence of the differential cross sections and the photon beam asymmetries. Possible background processes and contaminations under the $\Sigma(1385)/\Lambda(1405)$ signal regions were studied to get the $\Sigma(1385)/\Lambda(1405)$ events.

Differential cross sections for the $\Sigma(1385)/\Lambda(1405)$ photoproduction were measured as a function of $cos\Theta_{cm}^{K+}$ and the momentum transfer($\tilde{t}$) in the specific regions of 1.5$< E_\gamma <$2.4 GeV and 0.6$< cos\Theta_{cm}^{K+} <$1.0. The differential cross sections for the $\Sigma(1385)/\Lambda(1405)$ photoproduction shows the angular dependence of a forward peak behavior at the higher photon energy regions while they are flat angular dependence or slightly decrease at the forward angle region in the low photon energy regions. From the results of differential cross sections, we want to decompose the contributions of the pseudoscalar meson(K^-) and the vector meson(K^*) exchange in the $t-$channel for $\Sigma(1385)/\Lambda(1405)$ photpoproduction. However, it is difficult to conclude the production mechanism for $\Sigma(1385)$ and $\Lambda(1405)$ with only the results of the differential cross sections. Therefore, the measurement of the photon beam asymmetry is necessary to understand the production mechanism for $\Sigma(1385)$ and $\Lambda(1405)$.

Our experimental results of the photon beam asymmetries are the first measurement in the world for $\Sigma(1385)/\Lambda(1405)$ photoproduction. We found the energy dependence of photon beam asymmetries for $\Sigma(1385)/\Lambda(1405)$ and the magnitudes of the photon beam asymmetries increase up from 0 to the positive value as the photon energy increases above $E_\gamma \sim 2.1$ GeV.

From the experimental results, we expect that the contribution of the K^* meson exchange(natural parity exchange) for the $\Sigma(1385)$ is large at the high photon energy regions. However, the contribution of the K^- meson exchange(unnatural parity exchange) for the $\Lambda(1405)$ or resonances contributions are considerable at the low photon energy regions.

Acknowledgments

I sincerely appreciate to Prof. Takashi Nakano for giving me valuable opportunity to study in Osaka University with his abundant support and advice in my researches as well as life. I have learned a lot and improved my understandings in the field of this research under his guidance and advice, and I was inspired by his continuous efforts and passion in researches. Again, I would like to thank him for his advice, encouragement and support during long time.

I would like to thank Prof. Mizuki Sumihama in Gifu University for teaching me a lot of LEPS experiments and analysis work. Her comments and discussions for my Ph.D study were always very helpful to me. Also, I would like to thank Prof. JungKeun Ahn in Pusan National University for his continuous comments and discussion for this study. I would like to thank Prof. Masaru Yosoi, Prof. Norihito Muramatsu and Dr. Tomoaki Hotta who taught me a lot of experimental techniques.

I would like to thank all my committee members, Prof. Atsushi Hosaka, Prof. Hiroyuki Noumi, Prof. Tadafumi Kishimoto and Prof. Toru Sato.

I would like to thank my LEPS Collaborators Dr. W.C. Chang, Dr. Y. Kato Dr. M. Miyabe, Dr. M. Niiyama, Mr. T. Sawada, Mr. Y. Nakatsugawa, Dr. J. Y. Chen, Dr. S.H.Hwang, Dr. Y. Sugaya, Prof. T. Mibe, Dr. T. Yorita, Dr. H. Kohri, Dr. T. Ishikawa, Dr. T. Matsumura, Prof. M. Nomachi, Prof. H. Shimizu, Prof. K. Imai, Dr. T. Miwa Prof. H.Hicks, Prof. C.Rangacharyulu, Prof. H. Ejiri, Dr. H. Fujimura, Dr. Y. Ohashi and Dr. S. Date.

I would like to thank Prof. Atushi Hosaka and Dr. S. I. Nam for their comments in the theoretical aspects of this research. I would like thank my PNU laboratory memebers, Dr. H.S.Lee, Mr. S.J.Kim, Dr.B.H.Choi and J.Y.Park at Pusan National University.

Finally, I would like to thank my family for their continuous supports and encouragement.

Appendix A

The number of photons

The number of photons(N_γ) is obtained in each photon energy regions. as shown in Table A.1. [70]

$E_{\gamma,min}$	$E_{\gamma,max}$	n_v	n_h	Total(n_v+n_h)	n	n
1.50	1.55	.46394E+11	.42525E+11	.88919E+11	.91661	0.88982
1.55	1.60	.57066E+11	.49536E+11	.10660E+12	.86805	
1.60	1.65	.60729E+11	.52583E+11	.11331E+12	.86586	0.86044
1.65	1.70	.57023E+11	.48736E+11	.10576E+12	.85467	
1.70	1.75	.60758E+11	.52054E+11	.11281E+12	.85674	0.85454
1.75	1.80	.61280E+11	.52232E+11	.11351E+12	.85235	
1.80	1.85	.68527E+11	.58217E+11	.12674E+12	.84955	0.85195
1.85	1.90	.71274E+11	.60887E+11	.13216E+12	.85427	
1.90	1.95	.73849E+11	.62903E+11	.13675E+12	.85178	0.85593
1.95	2.00	.76769E+11	.66016E+11	.14279E+12	.85993	
2.00	2.05	.83518E+11	.71615E+11	.15513E+12	.85748	0.85228
2.05	2.10	.86236E+11	.73063E+11	.15930E+12	.84724	
2.10	2.15	.86254E+11	.74042E+11	.16030E+12	.85842	0.85858
2.15	2.20	.97412E+11	.83650E+11	.18106E+12	.85872	
2.20	2.25	.10016E+12	.85706E+11	.18586E+12	.85569	0.84861
2.25	2.30	.10015E+12	.84280E+11	.18443E+12	.84154	
2.30	2.35	.10097E+12	.86841E+11	.18781E+12	.86007	0.85640
2.35	2.40	.68498E+11	.58291E+11	.12679E+12	.85099	
2.40	2.45	.28151E+11	.24165E+11	.52316E+11	.85841	0.86228
2.45	2.50	.15807E+11	.13739E+11	.29546E+11	.86917	
1.50	2.40	1.35687E+12	1.16318E+12	2.52003E+12	**0.8573**	

Table A.1: The number of photons in each photon energy bins

The normalization factor which means the ratio of the horizontally and the vertically polarized photons for LLH2(2002-2003) is obtained in each photon energy region as Table A.1 and Fig A.1. The normalization factor n has 0.8573 for LLH2 in the region of $1.50<E\gamma<2.40$.

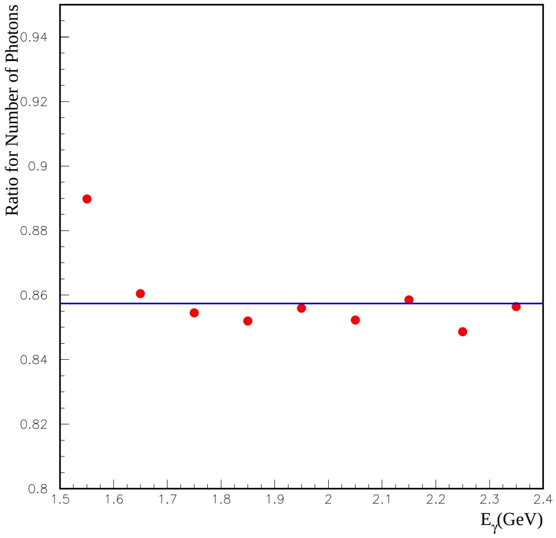

Figure A.1: Energy dependence of the normalization factor n=n_h/n_v

Appendix B

MC simulation - g3leps input

input	**value**	**input**	**value**
LTRK	1	CUTS	0.05 0.05 0.05 0.005
NTUP	1	DEBU	0 0 0
RAWH	1	DCAY	1
EMAX	100	ANNI	0
EMIN	0^a	BREM	0
EVNT	0	COMP	0
CHEK	0	PAIR	0
USRI	0	PHOT	0
SCAN	0^a	RAYL	0
SHCP	0^a	DRAY	0
PHIP	0^a	HADR	1
PERT	0^a	LOSS	1
BSIM	1	MULS	1
BPAR (horizontal)	1 1. 1. 0.6 -1 -1 0.0 0.	MUNU	0
BPAR (vertical)	1 1. 1. 0.6 -1 1 0.0 0.	SYNC	0
ODC1	0	RAYL	0
NEUT	0	LABS	0
SMER	1 1 1 1 00012 00003 00000	CKOV	0
DCEF	2 00010	TIME	2=9800. 3=-1000
VXEF	1 00001	RNDM	commented out
USRF	0	AUTO	0
VETO	0 0 0	SWIT	0 3 0 1 0 0 0 0 0 1
PSEL	0	ENER	2400.^{a}
TLH2	1	channel	11,12,13($\Lambda^*(1405)$)/31,32,33($\Sigma^*(1385)$)
FLAT	1	VOLU	'LEPS'
TARG	1 1	TRIG	-
RUNG	1 1^a	KINE	0 0. 0. 2.40^a
BEAM	0		
POLA	1^a		

Table B.1: The input parameters for g3leps MC simulation(g3leps.in)

Appendix C

Fit to the missing mass

Figure C.1- C.6 show the missing mass spectra in each azimuthal angle bins from high photon energy(E6) to low photon energy(E1) with the template fitting method I with including straight-line backgrounds. The figures from the fist to third line show the horizotanlly polarized case and from the 4th to 6th line show the vertically polarized case at 6 different photon energy regions as shwon in figure C.1- C.6. These yields are used to measure the photon beam asymmetry.

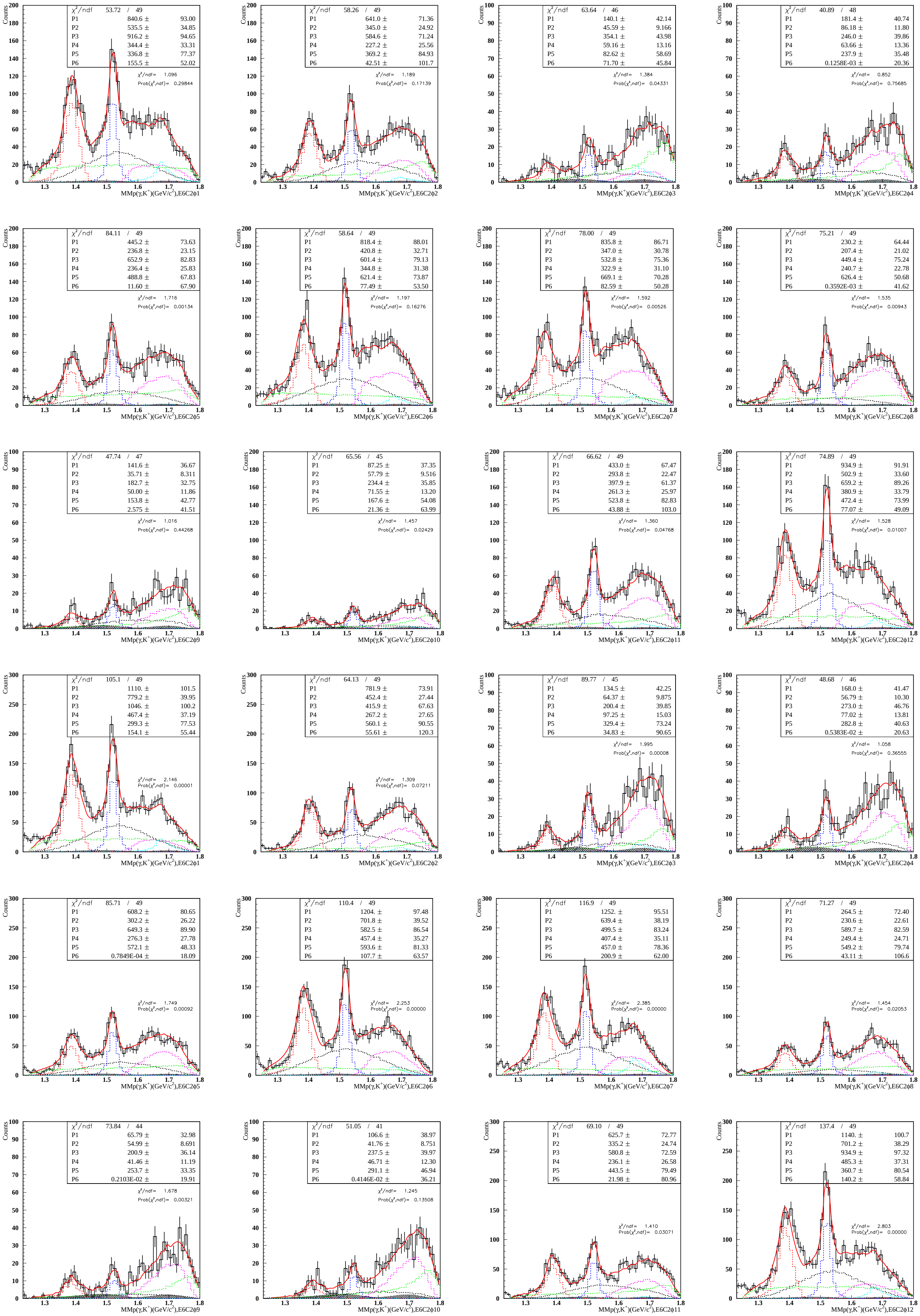

Figure C.1: Missing mass spectra with template fitting result for Σ(1385)/Λ(1405) at E6 photon energy region

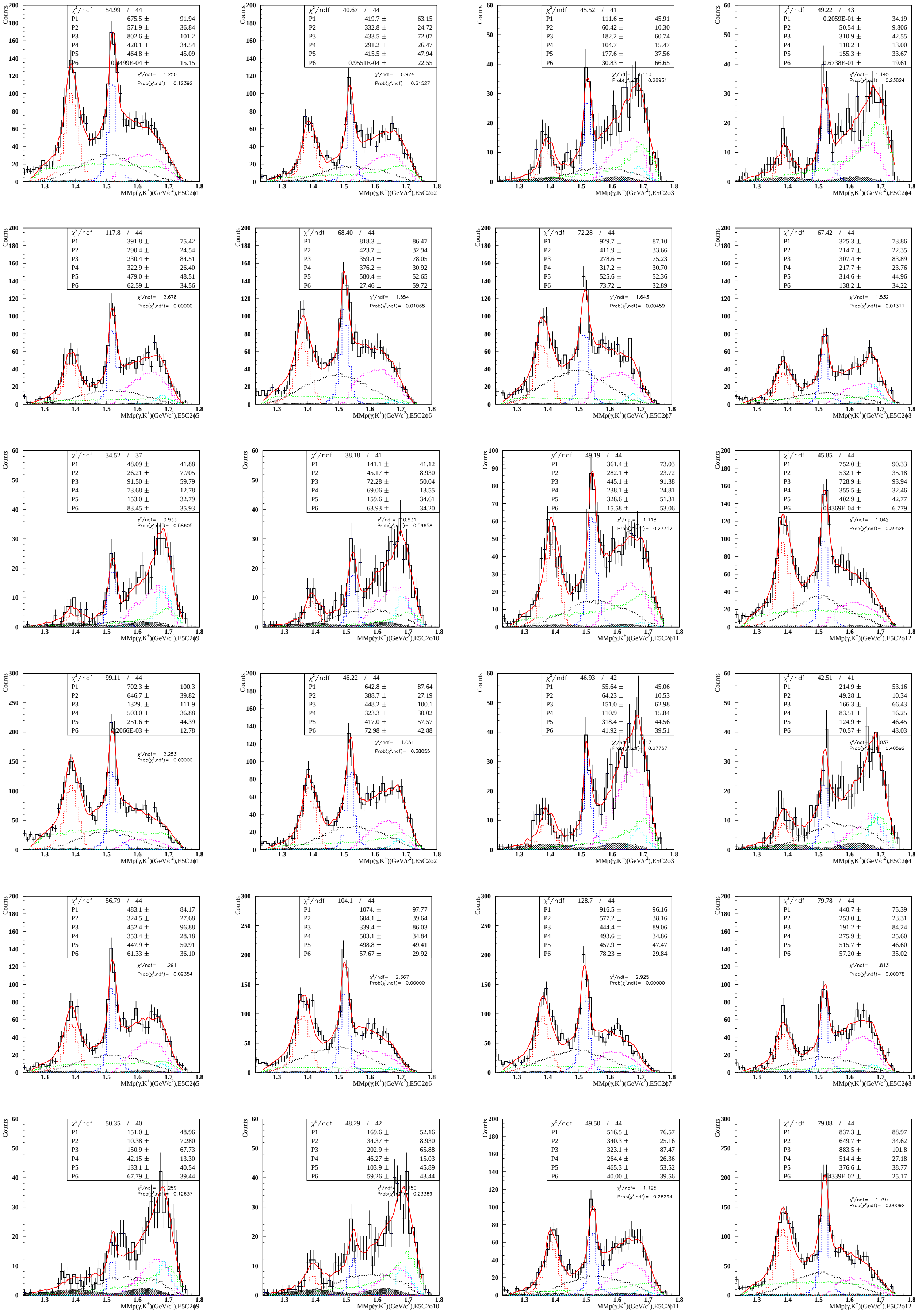

Figure C.2: Missing mass spectra with template fitting result for Σ(1385)/Λ(1405) at E5 photon energy region

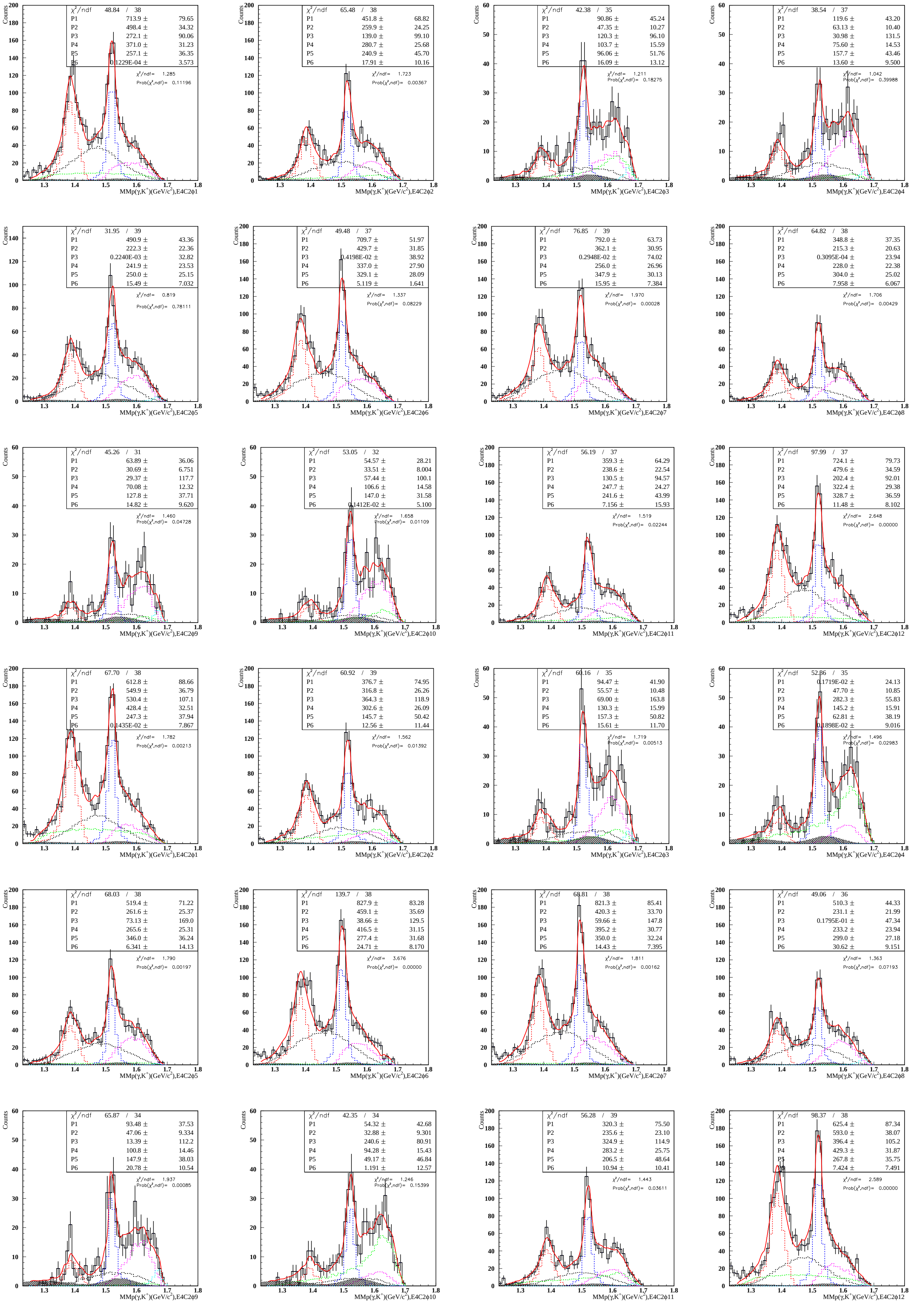

Figure C.3: Missing mass spectra with template fitting result for $\Sigma(1385)/\Lambda(1405)$ at E4 photon energy region

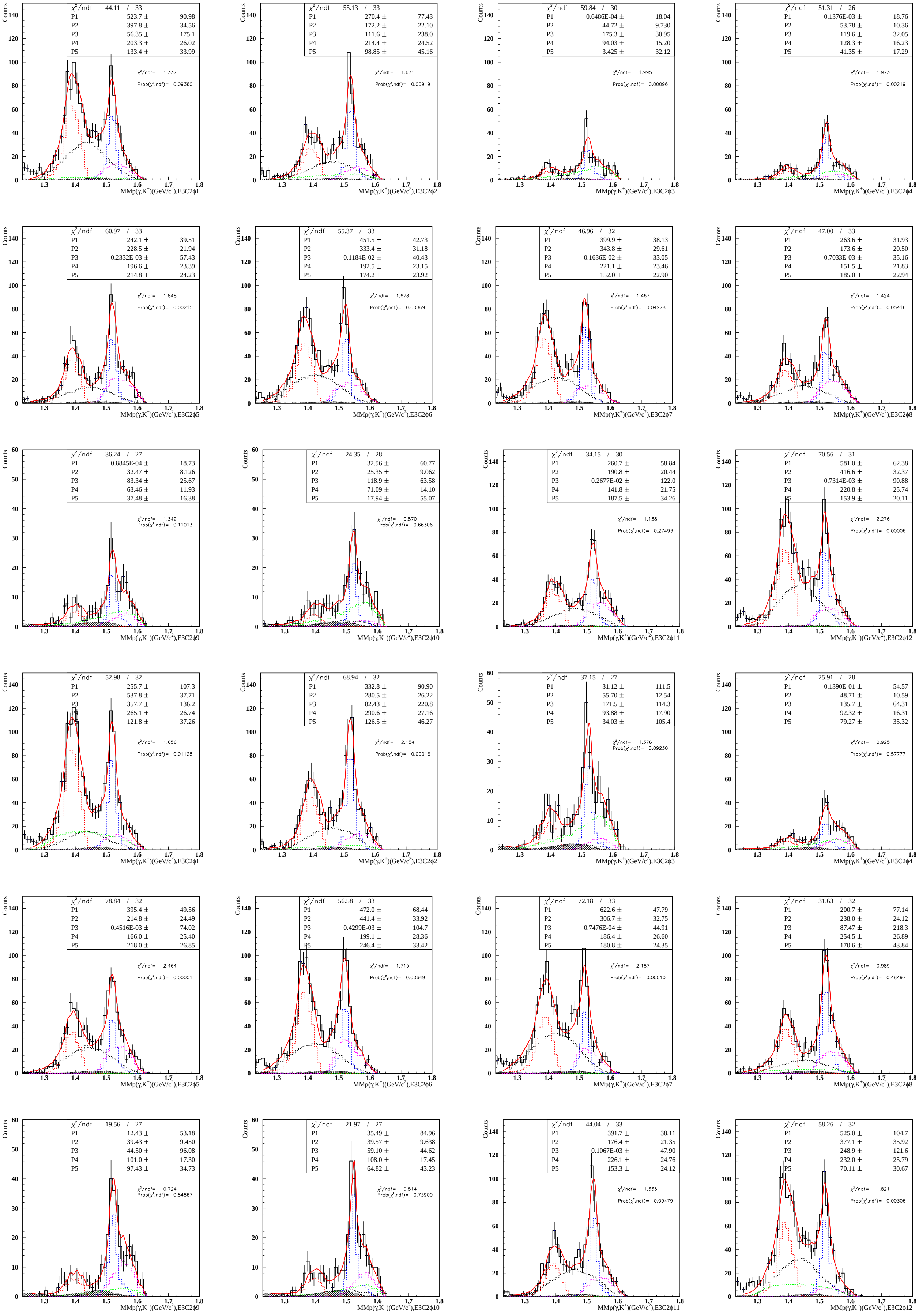

Figure C.4: Missing mass spectra with template fitting result for Σ(1385)/Λ(1405) at E3 photon energy region

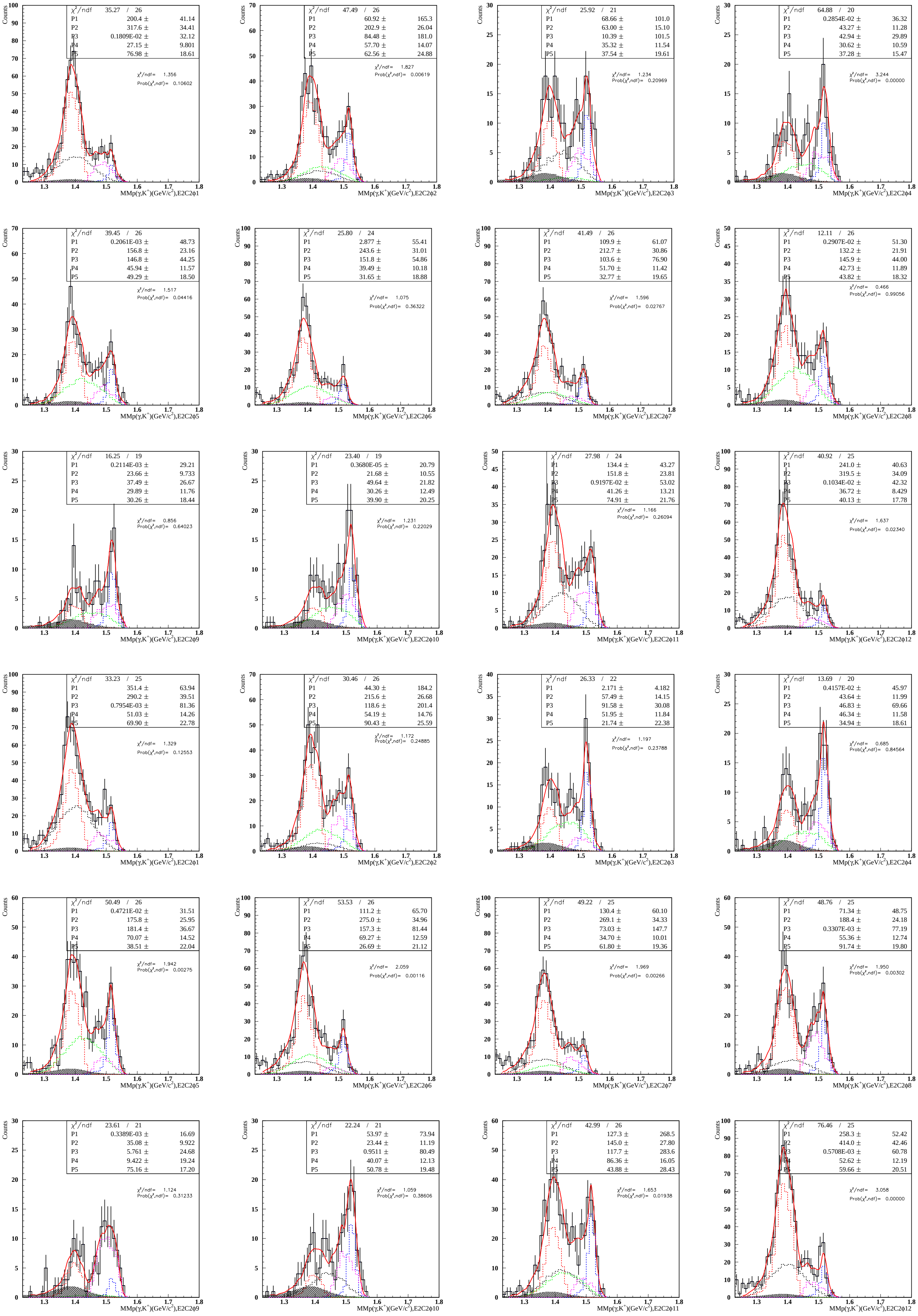

Figure C.5: Missing mass spectra with template fitting result for Σ(1385)/Λ(1405) at E2 photon energy region

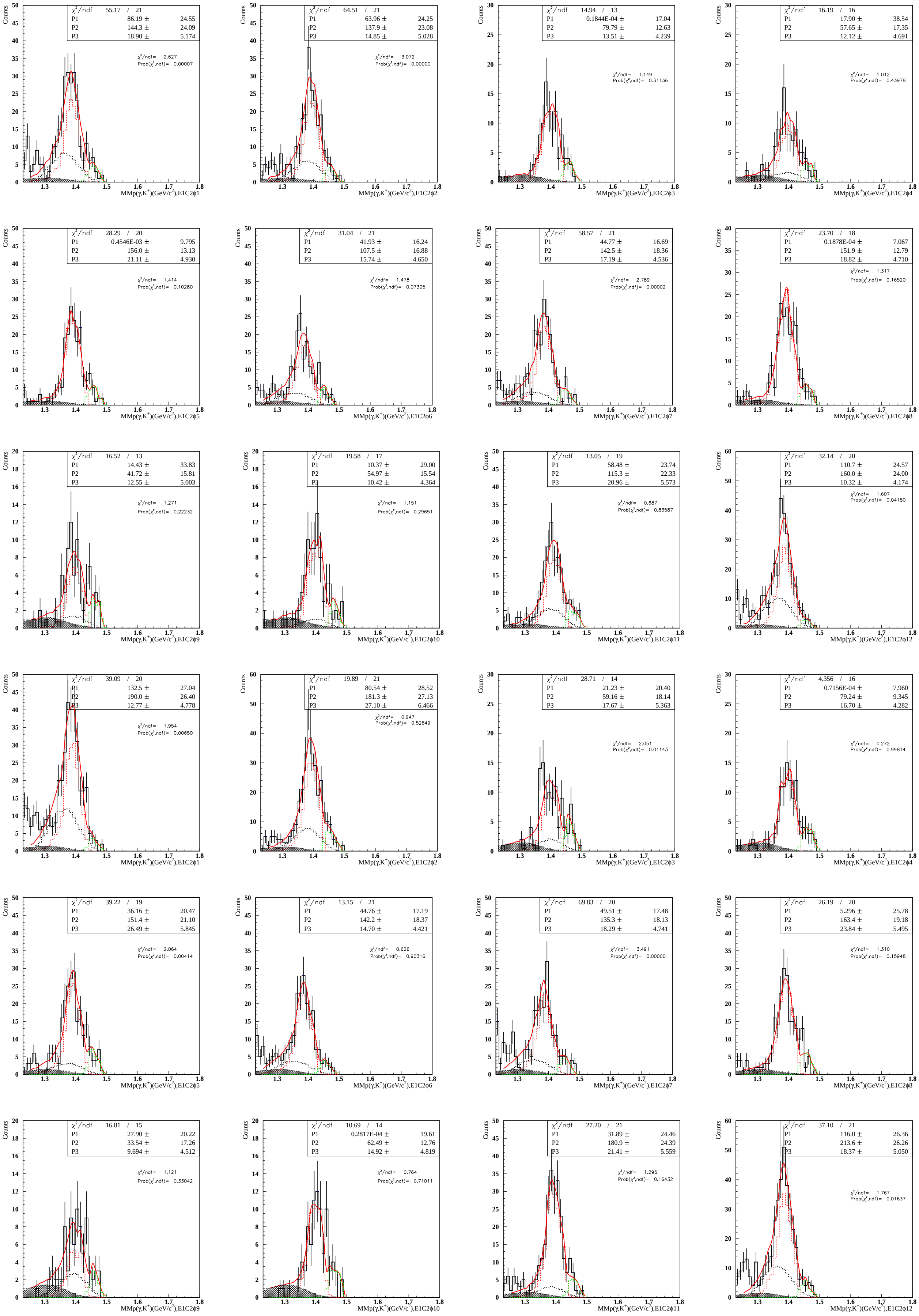

Figure C.6: Missing mass spectra with template fitting result for Σ(1385)/Λ(1405) at E1 photon energy region

Appendix D

Comparision with Lutz and Soyeur's model

The Lutz and Soyeur [34] suggested the double kaon pole contribution($\propto \frac{1}{(t-M_K^2)^2}$) is much stronger than the single kaon pole contribution ($\propto \frac{1}{(t-M_K^2)}$) in the t-channel process for the $\Sigma(1385)/\Lambda(1405)$ photoproduction of the differential cross sections($\mathrm{d}\sigma/\mathrm{d}\tilde{t}$) compared to the old(1970's) DESY data [24].

However, our accurate angular distribution measurements of $\mathrm{d}\sigma/\mathrm{d}\tilde{t}$ for the $\Sigma(1385)/\Lambda(1405)$ photoproduction at the forward angle regions do not give enough clues to identify the double kaon pole contributions. Our differential cross sections have similar $\tilde{t}$ distributions at large $\tilde{t}$, but they are smaller than the DESY data at low $\tilde{t}$ and inconsistent with the theoretical calculation curve of the double kaon pole contribution. These results indicate that the double kaon pole contribution is not dominant and there are other contributions than the double kaon pole contributions in the production mechanism of $\Sigma(1385)/\Lambda(1405)$.

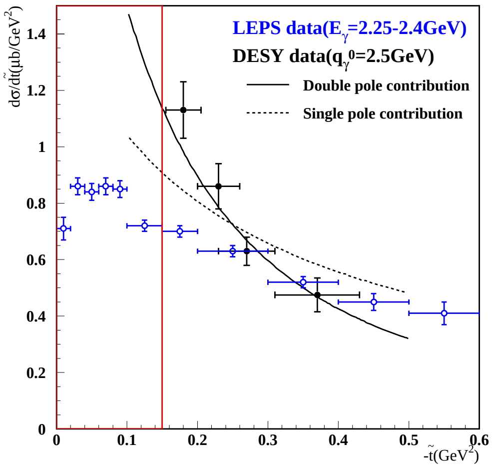

Figure D.1: Comparison of the differential cross sections($\mathrm{d}\sigma/\mathrm{d}\tilde{t}$) for the $\Sigma(1385)/\Lambda(1405)$ between the experimental results and the Lutz and Soyeurs's model theoretical calculation

Bibliography

[1] F. Halzen and A. D. Martin, 'QUARKS AND LEPTONS : An Introductory Course in Modern Particle Physics, John wiley & Sons (1984)

[2] R. Bradford *et al.*, Phys. Rev. **C73**, 035202 (2006)

[3] I. Hleiqawi *et al.*, Phys. Rev. **C75**, 042201(R)(2007)

[4] M. Q. Tran *et al.*, Phys. Lett. **B445**, 20, (1998)

[5] J. W. C. McNabb *et al.*, Phys. Rev. **C69**, 042201 (2004)

[6] K. H. Glander *et al.*, Eur. Phys. J. A19, 251 (2004)

[7] R. G. T. Zegers *et al.*, Phys. Rev. Lett. **91**, 092001 (2003)

[8] M. Sumihama *et al.*, Phys. Rev. **C73**, 035214 (2006)

[9] K. Nakamura *et al.*, J. Phys. **G37**, 075021 (2010) (PDG)

[10] N. Isgur, G. Karl, Phys.Rev.D **18**, 4187 (1978)

[11] R. H. Dalitz, T. C. Wong and G. Rajasekaran, Phys. Rev. **153**, 1617 (1967)

[12] R. H. Dalitz, S. F. Tuan, Phys. Rev. Lett. **2**, 425 (1959)

[13] Y. Nemoto, N. N akajima, H. Matsufuru and H. Suganuma, Phys. Rev. **D68**, 094505 (2003)

[14] M. F. M. Lutz, E. E. Kolomeitsev, Found. Phys. **31**, 1671 (2001)

[15] E. Oset, A. Ramos, C. Bennhold, Phys. Lett. **B527**, 99 (2002)

[16] D. Jido *et al.*, Phys. Rev. **C66**, 055203 (2002)

[17] M. F. M. Lutz, E. E. Kolomeitsev, Nucl. Phys. **A700**, 193 (2002)

[18] T. Hyodo *et al.*, Phys. Rev. **C68**, 065203 (2003)

[19] J. C. Nacher, E. Oset, H.Toki and A.Ramos, Phys. Lett. **B455**, 55(1999)

[20] M. Niiyama *et al.*(LEPS Collaboration), Phys. Rev. **C78**, 035202 (2008)

[21] J. K. Ahn *et al.*(LEPS Collaboration), Nucl. Phys. A721,715c(2003)

[22] K. Moriya, Doctor Thesis of Carnegie Mellon University, (2010) and K. Moriya, Panic 2011 conferences

[23] I. Schulday, Doctor Thesis of Bonn University, (2004)

[24] T. Azemoon *et al*, Nucl. Phys. **B95**, 77 (1975)

[25] L. Guo and D. P. Weygand,(CLAS Collaboration), in proceedings of internation Workshop on the Physics of Excited Bayrons(NSTAR05)

[26] J. H. R. Crouch *et al.*(Cambrigde bubble chamber group), Phys. Rev. **156**, 1426 (1967)

[27] R. Erbe *et al.*(DESY bubble chamber group), Nuovo Cimento A **49**, 504 (1967)

[28] R. Erbe *et al.*(ABBHHM Collaboration), Phys. Rev. **188**, 2060 (1969)

[29] I. Zychor *et al.*, Phys. Lett. **B660**, 167 (2008)

[30] E. Epple and L. Fabbietti for the HADES collaboration, nucl-ex/1202.0232v1, (2012)

[31] Y. Oh, C. M. Ko and K. Nakayamam, Phys. Rev. **C77**, 045204 (2008)

[32] S. I. Nam *et al.*, JKPS, Vol. 59, No. 4, Oct.(2011), pp.2676-2683
S. I. Nam *et al.*, hep-ph/arXiv:0806.4029
J. H. Park, Master Thesis, Pusan National University (2008)

[33] W. A. Williams, C. R. Ji and S. R. Contanch, Phys. Rev. **C43**, (1991), 452

[34] M. F. M. Lutz and M. Soyeur, Nucl. Phys. **A748**, 499 (2005)

[35] P. Stichel, Z. Phys. **180**, 170 (1964)

[36] http://www.spring8.or.jp.

[37] M. Fujiwara, *et al.*, Jornal of the Japanese Society for Synchrotron Radiation Research, **10** (1997) 23.

[38] M. Fujiwara, *et al.*, Acta. Phys. Pol. **29** (1998) 141.

[39] T. Nakano, *et al.*, Nucl. Phys. **A629** (1998) 559C.

[40] T. Nakano, *et al.*, Nucl. Phys. **A670** (2000) 332.

[41] T. Nakano, *et al.*, Nucl. Phys. **A684** (2001) 71.

[42] T. Nakano *et al.*, Phys. Rev. Lett. **91**, 012002 (2003)

[43] T. Mibe *et al.*, Phys. Rev. Lett. **95**, 182001 (2005)

[44] T. Ishikawa *et al.*, Phys. Lett. **B608**, 215, (2005)

[45] H. Kohri *et al.*, Phys. Rev. Lett. **97**, 082003 (2006)

[46] W. C. Chang *et al.*, Phys. Lett. **B658**, 209, (2008)

[47] M. Sumihama *et al.*, Phys. Lett. **B657**, 32, (2007)

[48] K. Hicks *et al.*, Phys. Rev. **C76**, 042201 (2007)

[49] K. Hicks *et al.*, Phys. Rev. Lett. **102**, 012501 (2009)

[50] T. Nakano *et al.*, Phys. Rev. **C79**, 025210 (2009)

[51] N. Muramatsu *et al.*, Phys. Rev. Lett. **103**, 012001 (2009)

[52] M. Sumihama *et al.*, Phys. Rev. **C80**, 052201(R) (2009)

[53] W. C. Chang *et al.*, Phys. Lett. **B684**, 6, (2010)

[54] H. Kohri *et al.*, Phys. Rev. Lett. **104**, 172001 (2010)

[55] T. Matsumura, Master thesis of University of Osaka (2000)

[56] A. D'Angelo, O. Bartalini, V. Bellini, P. Levi Sandri, D. Moricciani, L. Nicoletti and A. Zucchiatti, Nucl. Instr. Meth. **A455** (2000) 1.

[57] T. Mibe, Master thesis of University of Osaka (2000).

[58] R. Suda, M. Watanabe, R. Enomoto, T. Iijima, I. Adachi, H. Hattori, T. Kuniya, T. Ooba, T. Sumiyoshi and Y. Yoshida, Nucl. Instr. Meth. **A406** (1998) 213.

[59] O. Toker, S. Masciocchi, E. Nygard, A. Rudge and P. Weilhammer, Nucl. Instr. Meth. **A340** (1994) 572.

[60] T. Sasaki, Master thesis of University of Kyoto (2000).

[61] Y. Sugaya and M. Nomachi, Nucl. Instr. Meth. **A437** (1999) 68

[62] Y. Sugaya *et al.*, IEEE transactions on nuclear science **48** No.4 (2001) 1282

[63] CERN Program library

[64] R. Frühwirth, M. Regler, R. K. Bock, H. Grote, "Data Analysis Techniques for High-Energy Physics", Cambridge Univ. Press.

[65] R. Frühwirth, Nucl. Instr. Meth. **A262** (1987) 444.

[66] J. Myrheim and L. Bugge, Nucl. Instr. Meth. **160** (1979) 43.

[67] E. J. Wolin and L. L. Ho, Nucl. Instr. Meth. **A329** (1993) 493.

[68] J. Ajaka, *et al.*, Phys. Rev. Lett. **81** (1998) 1797.

[69] M. Sumihama, LEPS technical note No. 32.

[70] M. Sumihama, LEPS technical note No. 43.

[71] J. J. Sakurai, 'Modern Quantum Mechanics', Addison-Wesley Publishing Company,(1994)